Faculté des lettres et sciences humaines
Département de géomatique appliquée
Université de Sherbrooke

et

Fachbereich 2 (Biologie/Chemie)
Universität Bremen

Optical characterization of Polar winter aerosols and clouds

Konstantin Baibakov

Thèse présentée pour l'obtention du grade de Philosophiae Doctor en télédétection

und

dem Fachbereich 2 (Biologie/Chemie)
der Universität Bremen vorgelegt als Dissertation zur Erlangung des Grades eines Doktors der Naturwissenschaften (Dr. rer. nat.)

Sherbrooke/Bremen
2014

Composition du jury

Optical characterization of Polar winter aerosols and clouds

Konstantin Baibakov

Cette thèse a été évalué par un jury composé des personnes suivantes:

Norm O'Neill
Dép. de géomatique appliquée, Université de Sherbrooke, Sherbrooke, Canada
Directeur de recherche

Otto Schrems
Dept. of Chemistry, University of Bremen, Bremen, Germany
Co-directeur de recherche

Andreas Herber
Alfred Wegener Institute for Polar and Marine Research, Bremerhaven, Germany
Co-directeur de recherche

Alain Royer
Dép. de géomatique appliquée, Université de Sherbrooke, Sherbrooke, Canada
Examinateur

Thomas J. Duck
Dept. of Physics and Atmospheric Science, Dalhousie University, Halifax, Canada
Examinateur externe

Abstract

The Arctic region is particularly sensitive to climate change and has recently undergone major alterations including a dramatic decrease of sea-ice extent. Our ability to model and potentially mitigate climate change is limited, in part, by the uncertainties associated with radiative forcing due to direct and indirect aerosol effects which in turn are dependent on our understanding of aerosol and cloud processes. Aerosol loading can be characterized by aerosol optical depth (AOD) which is the most important (extensive or bulk) aerosol radiative parameter and arguably the most important regional indicator of aerosol behavior. One of the most important shortcomings in our understanding of Arctic aerosols is their behavior during the Polar winter. A major reason for this is the lack of night-time AOD measurements. In this work we use lidar and starphotometry instruments in the Arctic to obtain vertically resolved aerosol profiles and column integrated representations of those profiles (AODs) respectively. In addition, data from a space-borne lidar (CALIOP) is used to provide a pan-Arctic context and seasonal statistics in support of ground based measurements. The latter were obtained at the Eureka (80° N, 86° W) and Ny Ålesund (79° N, 12° E) high Arctic stations during the Polar Winters of 2010-11 and 2011-12. The physical significance of the variation of the small-amplitude AODs that are typical of the Arctic Polar Winter, requires verification to ensure that artifactual contributions (such as incomplete cloud screening) do not contribute to these variations. A process-level event-based analysis (with a time resolution of $\approx$ minutes), is essential to ensure that extracted extensive (bulk) and intensive (per particle) optical and microphysical indicators are coherent and physically consistent. Using the starphotometry-lidar synergy we characterized several distinct events throughout the measurement period: these included aerosol, ice crystal, thin cloud and polar stratospheric cloud (PSC) events. In general fine ($<1\mu m$) and coarse ($>1\mu m$) mode AODs from starphotometry (τ_f and τ_c) were coherent with their lidar analogues produced from integrated profiles : however several inconsistencies related to instrumental and environmental factors were also found. The division of starphotometer AODs into τ_f and τ_c components was further exploited to eliminate coarse mode cloud optical depths (spectral cloud screening) and subsequently compare τ_f with cloud-screened AODs using a traditional (temporal based) approach. While temporal and spectral cloud screening case studies at process level resolutions yielded good to moderate results in terms of the coherence between spectrally and temporally cloud screened data (both temporally screened starphotometer and lidar optical depths), seasonal results apparently still contained cloud

contaminated data. Forcing an agreement using a more restrictive, second-pass, clear sky criterion ("minimal cloud envelope") produced mean 2010-11 AOD seasonal values of 0.08 and 0.04 for Eureka and Ny Ålesund respectively. In 2011-12 these values were 0.12 and 0.09. Conversely, CALIOP AODs (0 to 8 km) for the high Arctic showed a slight decrease from 2010-2011 to 2011-2012 (0.04 vs 0.03).

Résumé

La caractérisation optique des aérosols et des nuages pendant l'hiver polaire

L'Arctique est particulièrement sensible aux changements climatiques et a récemment subi des modifications majeures incluant une diminution dramatique de l'extension de la glace de mer. Notre capacité à modéliser et à potentiellement réduire les changements climatiques est limitée, en partie, par les incertitudes associées au forçage radiatif induit par les effets directs et indirects des aérosols, qui dépendent de notre compréhension des processus impliquant les nuages et les aérosols. La charge des aérosols est caractérisée par l'épaisseur optique des aérosols (AOD) qui est le paramètre radiatif extensif le plus important et l'indicateur régional du comportement des aérosols sans doute le plus décisif. Une de nos lacunes majeures dans la compréhension des aérosols arctiques est leur comportement durant l'hiver polaire. Cela est principalement dû au manque de mesures nocturnes d'AOD. Dans ce travail, on utilise des instruments (lidar et photomètre stellaire) installés en Arctique pour mesurer, respectivement, les profils verticaux des aérosols et une valeur intégrée dans la colonne (AOD) de ces profils. En outre, les données d'un lidar spatial (CALIOP) sont utilisées pour fournir un contexte pan-arctique et des statistiques saisonnières pour supporter les mesures au sol. Ces dernières ont été obtenues aux stations arctiques d'Eureka (80° N, 86° W) et de Ny Ålesund (79° N, 12° E) durant les hivers polaires de 2010-2011 et 2011-2012. L'importance physique des petites variations d'amplitude de l'AOD est typique de l'hiver polaire en Arctique, mais suppose une vérification pour s'assurer que des artefacts ne contribuent pas à ces variations (par exemple un masque de nuage insuffisant). Une analyse des processus basée sur des événements (avec une résolution temporelle $\approx$ une minute) est essentielle pour s'assurer que les paramètres optiques et microphysiques extensifs (grossiers) et intensifs (par particules) sont cohérents et physiquement conformes. La synergie photomètre stellaire-lidar nous permet de caractériser plusieurs événements distincts au cours des périodes de mesures, en particulier : des aérosols, des cristaux de glace, des nuages fins et des nuages polaires stratosphériques (PSC). Dans l'ensemble, les modes fin ($<1\mu m$) et grossier ($>1\mu m$) de l'AOD obtenus par photométrie stellaire (τ_f et τ_c) sont cohérents avec leurs analogues produits à partir des profils intégrés du lidar. Cependant certaines inconsistances causées par des facteurs instrumentaux et environnementaux ont aussi été

trouvées. La division de l'AOD du photomètre stellaire τ_f et τ_c a été davantage exploitée afin d'éliminer les épaisseurs optiques du mode grossier (le filtrage spectral de nuages) et, par la suite, de comparer τ_f avec les AODs obtenues par le filtrage de nuages traditionnel (temporel). Alors que les filtrages temporel et spectral des nuages des cas étudiés au niveau des processus ont conduit à des résultats bons à modérés en termes de cohérence entre les données filtrées spectralement et temporellement (les épaisseurs optiques des photomètres stellaires et lidars étant toutes deux filtrées temporellement), les résultats saisonniers semblent être encore contaminés par les nuages. En imposant un accord en utilisant un second filtre, plus restrictif, avec un critère de ciel clair ("enveloppe minimale du nuage"), les valeurs saisonnières moyennes obtenues étaient de 0.08 à Eureka et 0.04 à Ny Ålesund durant l'hiver 2010-2011. En 2011-2012, ces valeurs étaient, respectivement, de 0.12 et 0.09. En revanche les valeurs d'épaisseur optique de CALIOP (estimées entre 0 et 8 km) ont légèrement diminué de 2010-2011 à 2011-2012 (0.04 vs. 0.03).

Zusammenfassung

Optische Charakterisierung von polaren Winteraerosolen und Wolken

Die Arktis reagiert auf Klimaveränderungen besonders empfindlich und hat in jüngster Zeit größere Veränderungen erfahren einschließlich einer dramatischen Abnahme der Meereisbedeckung. Die Möglichkeiten Klimaänderungen zu modellieren und potentiell abzuschwächen sind begrenzt. Dies beruht zum Teil auf den Unsicherheiten beim Strahlungsantrieb wegen der direkten und indirekten Aerosoleffekte, welche ihrerseits vom Verständnis der Aerosol- und Wolkenprozesse abhängen. Die Aerosolbelastung kann über die Aerosol Optische Dicke (AOD) charakterisiert werden. Sie ist der wichtigste Strahlungsparameter des Aerosols und wohl der wichtigste Indikator des Aerosolverhaltens. Eines der wichtigsten Defizite in unserem Verständnis des arktischen Aerosols ist das Verhalten während des polaren Winters. Einer der Hauptgründe dafür ist der Mangel an AOD–Messungen in der Dunkelheit der Polarnacht.

Im Rahmen der vorliegenden Arbeit wurden Lidarinstrumente und Sternphotometer in der Arktis eingesetzt um sowohl vertikal aufgelöste Aerosolprofile als auch säulenintegrierte Darstellungen dieser Profile (AODs) zu erhalten. Zusätzlich wurden Daten von einem satellitengetragenem Lidarsystem (CALIOP) genutzt um einen gesamt-arktischen Zusammenhang und saisonale Statistiken für die Unterstützung von boden-gebundenen Messungen zu erstellen. Die bodengebundenen Messungen wurden an den Stationen Eureka (80° N, 86° W) und Ny-Ålesund (79° N, 12° O) in der hohen Arktis während der polaren Winter von 2010-11 und 2011-12 durchgeführt. Die physikalische Signifikanz der Variationen der amplitudenmodulierten AODs, welche typisch für die arktischen Polarwinter sind, benötigt eine Verifikation um sicherzustellen, dass artefaktuelle Beiträge (wie z.B. unvollständiges Wolkenscreening) nicht zu diesen Variationen beitragen.

Eine ereignisbasierte Analyse auf Prozessebene (mit einer Zeitauflösung von ≈ Minuten) ist unerlässlich um sicherzustellen, dass extrahierte, extensive ("Bulk") und intensive (pro Partikel), optische und mikrophysikalische Indikatoren kohärent und physikalisch konsistent sind. Durch Zunutzemachung der Sternphotometer–Lidar-Synergie konnte eine Reihe unterschiedlicher Ereignisse in den betrachteten Messzeiträumen insbe-sondere Aerosole, Eiskristalle, dünne Wolken und Polare Stratosphärische Wolken (PSCs) charakterisiert werden. Im allgemeinen waren "fine" ($<1\mu m$) und "coarse mode" ($>1\mu m$) Aerosol Optische Dicken, die mit den Sternphotometern (τ_f und τ_c) bestimmt wur-

den, kohärent mit ihren Lidar-Analogen, die von integrierten Profilen abgeleitet wurden. Allerdings wurden auch einige nicht übereinstimmende Beobachtungen gemacht, die auf instrumentelle und Umweltfaktoren zurückzuführen sind.

Die Einteilung der Starphotometer AOD's in τ_f und τ_c Komponenten wurde weiter untersucht um "coarse mode" Wolken AOD's zu eleminieren ("spectral cloud screening") und folglich τ_f mit "cloud-screened" AOD's zu vergleichen unter Verwendung eines traditonellen (zeitbasierten) Ansatzes. Während zeitliche und spektrale Fallstudien des "cloud screenings" mit Auflösungen auf Prozessniveau gute bis moderate Ergebnisse bezüglich der Kohärenz zwischen spektralen und zeitlich "cloud gescreenter" Daten (sowohl zeitlich "gescreente" Sternphotometer - und Lidar - Optische Dicken) lieferten, beinhalteten saisonale Ergebnisse noch wolkenkontaminierte Daten. Die Herbeiführung einer Übereinstimmung mittels Anwendung eines restriktiveren, "second-pass, clear-sky" Kriteriums (minimale Wolkenbedeckung) lieferte mittlere, saisonale AOD-Werte von 0,08 für Eureka und 0,04 für Ny-Ålesund. Im Winter 2011-12 lagen die entsprechenden Werte bei 0,12 und 0,09. Im Gegensatz dazu zeigten die AODs von CALIOP (0 – 8 km) für die hohe Arktis eine leichte Abnahme im Zeitraum der Winter von 2010-2011 bis 2011-2012 (0,04 zu 0.03).

Acknowledgements

Foremost, I'd like to thank Dr. Norm O'Neill for his genuine curiosity for the unknown, his rigour and his seemingly endless source of ideas. It has been a challenging, yet rewarding journey into the world of aerosols and Arctic landscapes!

Many thanks to Drs. Otto Schrems and Andreas Herber who courageously agreed to co-supervise a joint PhD despite the inevitable bureaucratic burden of such an activity. Their help and support, especially while in Germany, is very much appreciated.

I heartily acknowledge Dr. Christoph Ritter for his hospitality and attention while at AWI-Potsdam. His humour, enthusiasm and inquisitive mind made it a joyful and memorable stay.

I'm thankful to Drs. Tom Duck and Alain Royer for agreeing to review this manuscript.

Liviu Ivanescu and Siggi Debatin provided valuable instrumental support at Eureka and Ny Ålesund respectively.

The CRL data was kindly supplied by Dr. Tom Duck. I also thank Chris Perro for all the help with CRL data processing.

Dr. Karl-Heinz Schulz provided valuable technical guidance and advice while operating the SPSTAR starphotometer.

I am also indebted to a long-time friend and colleague, Dr. Yann Blanchard, for help with CALIOP processing and all of the last-minute French revisions. He has also been a great company and help while on Eureka missions – a source of souvenirs that will last a lifetime.

I'm thankful to the amazing and diverse group at CARTEL, many of whom I'm lucky to call friends!

Lastly, I acknowledge my family who always followed me in my thoughts to the remote places of the planet and who were always present when I needed them. Their care and love makes everything possible!

Contents

List of Figures

List of Tables

Chapter 1

Introduction

1.1 Arctic region in the context of climate change

Because of its unique, perturbation sensitive conditions, such as cold temperatures, highly reflective snow and ice cover as well as a extreme seasonal cycle in solar radiation, the Arctic is often viewed as an early indication system for many aspects of climate change. Global mean surface temperatures are currently increasing at an unprecedented rate, a phenomenon referred to as global warming. The Arctic, however, is warming even faster than the rest of the world with larger changes being projected (Figure 1). In fact, the Arctic region has been recently undergoing major alterations including alarmingly increasing temperatures, retreating sea-ice cover and record low ozone concentrations in the winter (*Moritz et al.*, 2002; *Wang and Key*, 2003; *Manney et al.*, 2011; *Duarte et al.*, 2012).

Global Circulation Models (GCMs) are used to simulate climate processes and are essential in our ability to predict future climate. The current GCMs underestimate the rate of sea-ice decline (*Stroeve et al.*, 2011) and differ substantially in terms of their projections (*Kattsov and Källén*, 2005). The differences between observations and model simulations and the scatter among models are due to the uncertainties in the underlying physical processes. In particular, the lack of understanding associated with the complexity of aerosol and cloud processes remains one of the major obstacles in accurately reproducing and predicting the Arctic climate (*Kattsov and Källén*, 2005; *Inoue et al.*, 2006).

The role of aerosols is also considered to be crucial in our potential ability to lessen or moderate climate change. The greenhouse gases, principally carbon dioxide (CO_2) and

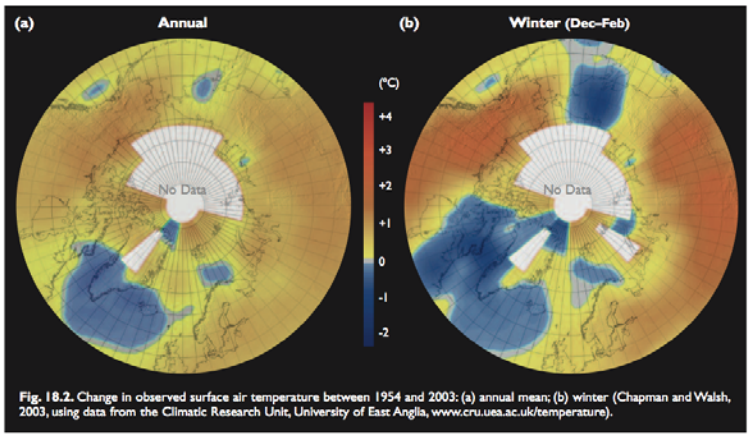

Figure 1: Change in observed surface air temperature between 1954 and 2003: a) annual mean; b) winter. Annual average surface air temperatures increased by 2 to 3° C in Alaska and Siberia . The increase during the winter months has been up to 4° C (from *Huntington et al.*, 2005, p3))

methane (CH_4), exert the strongest forcing on climate and are thought to be the main agents responsible for global warming (*Forster et al.*, 2007). The CO_2 concentrations have increased by more than 30% since the preindustrial levels, a rise that has been mainly attributed to human activities. The reduction of the atmospheric CO_2 concentrations is the backbone of any meaningful effort to mitigate climate change. However, even if CO_2 emissions were rapidly decreased, the current warming and thawing of the Arctic might persist, given the long life time of the CO_2 ($\approx$200 years) that is already present in the atmosphere. Hence, the goal of impeding the drastic changes in the Arctic may better be achieved, in the short term, by modifying the contributions of short-lived climate forcers, notably aerosols (*Shindell and Faluvegi*, 2009; *AMAP*, 2011; *Duarte et al.*, 2012).

1.2 Aerosol effects on climate

Aerosols are small particles suspended in the atmosphere with sizes ranging from $\approx$0.01 to 100μm in diameter (*Hinds*, 1999). Some aerosol examples include biomass burning plumes, desert dust and particles from erupted volcanoes. One of the principal difficulties with studying aerosols, is that they exhibit a multitude of shapes, sizes and chemical compositions and are highly variable in time and space. Aerosol particles can be characterized by their extensive and intensive properties. The former refer to the amount of aerosol (number density or concentration) while the later pertain to single-particle

attributes such as size and type. While the dominant optical effects of aerosols are associated with their extensive properties, their intensive properties can also be important (eg. *Dusek et al.*, 2006). Aerosols can significantly alter the Earth's radiative balance[1] , both directly by absorbing and scattering solar and terrestrial radiation, and indirectly by influencing cloud properties through their critical role as cloud condensation nuclei and ice forming nuclei. Depending on their properties as well as the underlying surface albedo[2] , aerosols can either warm or cool the atmosphere. The extent of aerosol influence is currently among the largest uncertainties in climate studies (*Forster et al.*, 2007). The net effect is thought to be cooling, but this is a general statement. The existence of highly reflecting surfaces during the Arctic spring means, for example, that even a moderately absorbing aerosol can cause warming (*Pueschel and Kinne*, 1995). Moreover, *Shindell and Faluvegi*, 2009 argue that for the period 1976-2007, the reduction in sulphate (scattering) aerosols and the increase in black carbon (absorbing) aerosols might account for more than half of the observed surface temperature increase in the Arctic. Aerosols are especially poorly understood in the Arctic. This is a region where their effects are particularly important but where our knowledge of the actual aerosol load, transport as well as physical and chemical properties is very limited. Furthermore, the winter period – from roughly late October to late March – is associated with the largest gap in aerosol data inasmuch as available optical measurements are largely based on the extinction or scattering of solar radiation. There are various methods to study aerosol properties including in-situ measurements (eg. air sampling and particle counting) as well as remote sensing techniques. The latter comprise primarily passive photometry observations and active laser-based lidar measurements.

1.3 Photometry and lidar aerosol measurements

Aerosol optical depth (AOD) is the most important (extensive) aerosol radiative parameter. It is an indicator of the total column vertical extinction (absorption and outscattering) due to aerosols in the atmosphere. Furthermore, AOD spectral shape (i.e. coincident AOD measurements at different wavelengths) serves as an indication of particle size. AOD has historically been estimated using ground-based sunphotometers that measure the at-

[1] the balance between the incoming and outgoing energy (or radiation) in the Earth-atmosphere system

[2] a fraction of the total incoming radiation that is reflected by the surface

tenuation of the solar radiation propagating through the atmosphere (*Shaw*, 1983). It should be noted, that if column extinction measurements include aerosols and/or clouds it is more appropriate to talk about POD (particulate optical depth, e.g. *Liu et al.*, 2009). In the past decade there has been substantial progress in deriving AOD products from passive, space-borne sensors (*Kaufman et al.*, 2002; *Kokhanovsky and de Leeuw*, 2005). Their notable handicap, similarly to sunphotometry, is that they are limited to the daytime periods. This data gap is aggravated at the Earth's poles, where no optical data can be taken during the Polar winter. Several photometry techniques have been developed to address the lack of night-time AOD measurements including broadband photometry (eg. *Musat*, 2004 and moonphotometry (*Berkoff et al.*, 2011; *Barreto et al.*, 2012). Both techniques, however, have their own disadvantages: broadband measurements lack or are limited in their spectral information content while moonphotometry observations are limited by the lunar cycle down to approximately one week per month. The relatively recent technique of starphotometry, employing bright stars as sources (eg. *Leiterer et al.*, 1995; *Herber et al.*, 2002; *Pérez-Ramírez et al.*, 2008a) represents a nighttime analogue to sunphotometry. Starphotometry excels where other techniques struggle: it can be used whenever the stars are visible in the sky and it supplies spectral information needed for particle size estimations. This technique, however, is still associated with a number of operational difficulties mostly due to high pointing accuracy requirements[3] and weak star light sources. The difficulties are further exacerbated in the Arctic because of the extreme environmental conditions and logistical constraints. There are currently only two starphotometers installed in the Arctic region: at Eureka (Nunavut, 79° 59'N, 86° 56'W) and Ny Ålesund (Svalbard, 78° 55'N, 11° 55'E). Part of the reason for deployment of starphotometers at these sites was the presence of lidar instruments: CRL (CANDAC Raman Lidar) at Eureka and KARL (Koldewey Aerosol Raman Lidar) at Ny Ålesund.

Ground-based lidars (LIght Detection And Ranging) provide vertically resolved aerosol and cloud profiles (see, for example, *Weitkamp*, 2005) based on the propagation delay of backscattered laser pulses. Ultimately, a lidar is a backscatter-measuring instrument, but the signal can also be vertically integrated to yield a measure of AOD during the night. The accuracy of the lidar-estimated AODs, however, typically depends on one's ability to disentangle the extinction and backscatter information contained in the lidar

[3]starphotometer fields of view (FOV) are a fraction of a degree (≈ a few tenths of a degree) while a typical in-situ sunphotometer FOV is on the order of 1-3 degrees and can reach up to 4-5 degrees for airborne instruments

return. One possible solution is to assume an extinction to backscatter (intensive parameter) ratio (or lidar ratio, S_a) but its estimation, in terms of achieving accuracies that are commensurate with sunphotometry or starphotometry, is a non-trivial task. The advanced Raman technique (*Ansmann et al.*, 1992; *Wandinger*, 2005) allows a direct measurement of the lidar ratio but, given the weakness of the Raman return and the low optical depths typically encountered in the Arctic, the resulting estimates will be, in the absence of a very strong aerosol event, of limited accuracy. Hence, photometers and lidars are exceptionally complementary: the former yield a robust measure of the total column extinction and its spectral variation, while the latter are best suited for measurements of vertically resolved backscatter profiles with limited spectral information.

Lidars can supply supplementary information about aerosols via depolarization and color ratios. The former refers to the capacity of particulates to change the polarization of the outgoing laser pulse and can serve as an indication of particle shape, and, to a certain extent, particle size. The latter is defined for multi-channel lidars as a ratio of two backscatter coefficients at different wavelengths.

CALIOP[4] (*Winker et al.*, 2003) launched on the CALIPSO satellite in 2006, is currently the only space-borne lidar. It can provide cross-Arctic, vertical-profile slices (curtains) of aerosols and clouds as well as limited information on particle size, type and shape (primarily from the depolarization ratio, or DR, profiles which this system generates). Unlike ground-based lidars CALIOP is capable of obtaining the measurements close to the ground, but has poorer spatio-temporal resolution and can not see through optically thick clouds. As far as estimating AOD is concerned, it suffers from the same requirement for reasonably accurate estimates of lidar ratio as ground-based lidars.

Simultaneously acquired starphotometer and lidar measurements can yield a better understanding of observed aerosol processes at temporal resolutions of the order of minutes. Such resolutions are typical of, for example, the time scales of turbulence in the atmospheric boundary layer (*Menut et al.*, 1999) and lend credence to arguments concerning our ability to optically observe process level events in the atmosphere. In the following section we provide more details on the synergism between starphotometer and lidar measurements.

[4]Cloud-Aerosol LIdar with Orthogonal Polarization

1.4 Characterization of Polar Winter Arctic aerosol events

While the Arctic is generally considered as a very pristine environment, radiatively important aerosol intrusions are typical for this region and can include biomass burning and forest fire smoke as well as volcanic plumes transported from mid-latitudes (*Stone et al.*, 2008; *Engvall et al.*, 2009; *Young et al.*, 2012). An event-based approach, in which one studies process level mechanisms as a necessary precursor to the analysis of phenomenological, large-scale statistics, is essential to understanding the fundamental physics that drive such events. The assemblage of validated or partly validated events can only help to lend confidence in our ability to characterize such events and lead to refinements in aerosol physics packages employed in aerosol transport models and eventually radiative forcing packages employed in climate models. Given the scarcity of Arctic datasets, one usually seeks to combine all-available ground-based, satellite and modeled data to validate the physical significance of any given event. In particular, the synergy of ground-based sunphotometer and lidar instruments has proven to be very effective in Arctic aerosol studies during the day-time. The combined use of sunphotometers and lidar, accompanied by supplementary backward trajectories (calculated from meteorological data), satellite and other data, has been successfully applied to characterize Arctic aerosol events during the summer time: (*O'Neill et al.*, 2008; *Hoffmann et al.*, 2010; *Saha et al.*, 2010; *Stock et al.*, 2012). The occurrence and characteristics of aerosols during the Polar Winter are studied to a much lesser extent. Polar Winter atmospheric conditions, however, are distinctly different from the Polar summer period : they are associated with a number of unique processes such as, for example, cloudless ice crystal precipitation, commonly termed "diamond dust" (*Curry et al.*, 1990; *Intrieri and Shupe*, 2004). Furthermore, the winter period is associated with maximum seasonal aerosol load, a phenomenon termed Arctic Haze (*Quinn et al.*, 2007). A better characterization of Polar Winter aerosols thus represents an important step towards a more comprehensive year-round view of Arctic processes. One of the principal obstacles towards this goal is the lack of night-time AOD measurements.

Eureka and Ny Ålesund are currently the only two stations in the Arctic with a significant Polar Winter AOD record (consisting of starphotometry observations and lidar profiles which could be transformed into low-accuracy AODs given prescribed values of lidar ratio). *Herber et al.*, 2002 present multi-year AOD dynamics at Ny Ålesund derived

from a combination of a sun-, star- and, to a lesser extent, moonphotometry observations. This work was based on daily AOD averages and did not focus on individual events or sub-diurnal variations. Furthermore, no coincident lidar data was available for the study period.

In terms of photometry observations and starphotometry measurements in particular, the physical significance of small-amplitude AODs, typical for the Arctic, is by no means well defined. Variations in AOD can be < 0.01 (*O'Neill et al.*, 2008), which is at the lower limit of or even below nominal instrumental measurement capabilities. In reality little is known about the lower limit of instrumental sensitivity (below the nominal limit determined from calibration considerations) in the presence of real aerosol variations. Whatever that lower limit is, it is certain that spectral curvature-based retrieval algorithms (that, for example, can be employed to calculate fine mode (submicron) and coarse mode (supermicron) contributions to the AOD) can be problematic in clear atmospheres as the error varies (roughly) as the inverse of the AOD (*O'Neill et al.*, 2003). Lidar-derived aerosol products suffer from numerous limitations : AOD estimates, for example, depend on prescribed lidar ratio values, vertical profiles of backscatter signal can have uncertainties in the lowest altitudes because of the incomplete overlap between the divergence of the laser beam and the receiver field of view.

These types of photometry and lidar issues impact the confidence one can attribute to the analysis of any single event. Consequently, process-level analysis (on a time scale of minutes) of simultaneously acquired starphotometry and lidar data is an important tool to ensure that the extracted extensive (bulk) and intensive (per particle) optical and microphysical indicators are coherent and physically consistent. Within the synergistic analysis of the two datasets one can, for example, study the correlation of startphotometry AODs with lidar-integrated backscatter profiles.

The lidar DR is predominantly a function of particle habit (i.e. the gamut of possible shapes between spherical particles and complex crystals). It is also, invariably, a means of discriminating fine mode particles from coarse mode particles, whether the former are smoke, pollution related or volcanic sulfates (see *O'Neill et al.*, 2012 for example). This could, at least in part, imply that non spherical fine mode particles (such as smoke particles, known to be of complex shape near the source) would, on average, progressively evolve towards more spherical shapes as they were transported through the atmosphere and subjected to condensation processing. However it is also, in part (or largely) due to the fact that fine mode particles, of a few tenths of μm in radius, are characterized by

low (linear) depolarization ratios almost independently of particle shape (see for example, Fig. 1 of *Mishchenko and Sassen*, 1998 where their simulated DR is $\lessapprox 10\%$ for typical fine mode effective radii extremes between 0.1 and 0.3 μm and a range of particle shapes and Fig. 10 (c) of *You et al.*, 2006 where the DR of their simulated smoke particles of 0.1 μm effective radius is also $\lessapprox 10\%$ for a range of particle shapes and small optical depths).

Photometry-lidar process-level analysis has not, as far as we can determine, ever been addressed in the literature in any kind of substantial fashion until *O'Neill et al.*, 2008 were able to exploit the presence of a continuously operating, high spectral resolution lidar at the Eureka (PEARL) site deployed alongside a sunphotometer acquiring high frequency (3 minute sampling time) AOD data. The synchronicty of the two sensors in terms of (a) the covariance of the backscatter coefficient with the AOD, coupled with (b) the Lidar depolarization ratio and its coherence with the separation of the AODs into sub and super-micron components showed there was significant, process level correlation in spite of the fact that the sensors were separated by 15 km and made measurements along different lines of sight (zenith looking for the lidar versus sun-looking for the sunphotometer).Furthermore, while *Alados-Arboledas et al.*, 2011 showed the feasibility of combining starphotometry and lidar data to study fresh biomass burning at mid-latitudes, there currently exist no works dealing with starphotometry-lidar synergistic processing of Arctic aerosol events.

This thesis is aimed to mitigate, to a certain extent, the problems of the extreme scarcity of Polar Winter AOD measurements in the Arctic and the absence of process-level analysis of starphotometry and lidar data. During the Polar Winters of 2010-11 and 2011-12 starphotometers and lidars were operated in tandem at Eureka and Ny Alesund whenever possible. Within the context of this work we seek to analyze the datasets obtained with an eye towards a better understanding of the process-level dynamics of distinct aerosol and thin cloud events. Complimentary CALIOP data and backward trajectories will be employed in an attempt to give additional temporal and spatial context to the ground-based data. The accumulation of detailed event studies is a critical component towards an evolved understanding of aerosols as well as the inter-dynamics of aerosols and clouds.

The rest of the document is structured as following. Chapter 2 presents the hypotheses and objectives of the current work. Chapter 3 provides theoretical considerations relative to measurement techniques and discusses problems relative to the Arctic. Chapter 4

describes project methodology based on the photometry-lidar synergy while chapter 5 provides the description of measurement sites and instrumentation. Chapter 6 contains principal results obtained within the context of the current work. Finally, chapter 7 summarizes project findings and gives an outlook for future work.

Chapter 2

Hypotheses and objectives

2.1 Hypotheses

1. Measurements of starphotometry yield PODs results which are optically coherent with lidar backscattering profiles as well as physically consistent with theoretical considerations.

The validation of this first hypothesis can be partially achieved using comprehensive data comparisons between starphotometers and lidars during the polar winter. A particular test will include the correlation between starphotometer PODs and integrated lidar backscatter profiles. Also, spectral PODs from starphotometry will be analyzed in terms of the extensive particle information contained in the fine and coarse mode PODs.

2. A better understanding of process-level optical phenomena will provide insights into critical aerosol processing protocols such as AOD cloud screening and important climatological level behavior such as seasonal AOD statistics.

To validate the second hypothesis, we will analyze the starphotometry and lidar data on a night-by-night basis, trying to pinpoint and characterize the presence of aerosols, as was done semi-qualitatively in *Baibakov*, 2009. This synergy analysis can be supported by other supplementary information, such as satellite data and backward trajectories. The intensive and extensive analysis will also clearly represent an integral part of aerosol-event characterization.

2.2 Project Objectives

Based on polar-night AOD measurements acquired at the Canadian CANDAC High Arctic observatory at Eureka and the Ny-Ålesund German AWIPEV observatory, CALIOP and other supplementary data, we seek to better understand the temporal and spatial variability of Arctic aerosol concentration, size and type. In particular the following objectives are defined.

2.2.1 Acquisition and processing of a significant and representative night-time AOD dataset

The primary (methodological) objective of the proposed work is to acquire and analyze a significantly long and representative time series of nighttime AOD values. While the feasibility of starphotometry measurements in the Arctic has already been shown in *Herber et al.*, 2002 the installation, calibration and operation of the starphotometer in harsh Arctic environment remains a non-trivial task. Some of the difficulties include optical and mechanical alignment of the instrument, automatic star tracking and ice crystal deposition on the collecting optics. All of these can result in data artifacts or inconsistencies and need to be addressed. Furthermore, the accuracy of the starphotometry data obtained with the one-star method (the dominant operational mode, see below) is directly dependent on the accuracy of the calibration values. Accordingly, the starphotometer calibration procedures need to be carefully established and performed (*Gröschke*, 2009).

2.2.2 Characterization of polar-winter AOD variability based on starphotometry and lidar data

The main task is to characterize Polar-winter AOD variability at Eureka and Ny Ålesund based on the synergy of starphotometry and lidar data. On a short time scale ($\approx$ 1-3 days), the emphasis will be on process-level analysis of particular events (or features) detected by the two instruments. In addition, pan-Arctic curtains of CALIOP data and HYSPLIT backward trajectories will also permit a better understanding of the spatio-temporal extent of the ground-based measurements. On a longer time scale ($\approx$ months) we seek to analyze AOD trends for seasonality patterns such as enhanced aerosol concentrations in spring, a phenomenon known as Arctic Haze (*Quinn et al.*, 2007).

Chapter 3

Theoretical and measurement background

3.1 Light extinction and optical depth

3.1.1 Total optical depth

As light propagates through the atmosphere, it gets gradually attenuated by various atmospheric constituents, namely gases and particles. Consider a beam of radiation passing through an arbitrary thin atmospheric layer in Figure 2.

The beam's monochromatic radiance I_λ is decreased by:

$$\frac{dI}{I_\lambda} = -\kappa(s)ds \tag{1}$$

where ds is the differential path length along the ray path of the incident radiation and κ the *extinction* (attenuation plus scattering) *coefficient* with typical units of inverse length (km^{-1}). It is important to note that the latter quantity is a fundamental property of the medium (i.e. independent of the light field) representing the fraction of light, which will be attenuated per unit distance in any direction. It is the product of the extinction cross section per particle (the effective optical area of a single interacting particle), σ (typical units of μm^2), times the particle number density, N (typical units of cm^{-3}) (see *Rees*, 2001 for example):

$$\kappa = \sigma N \tag{2}$$

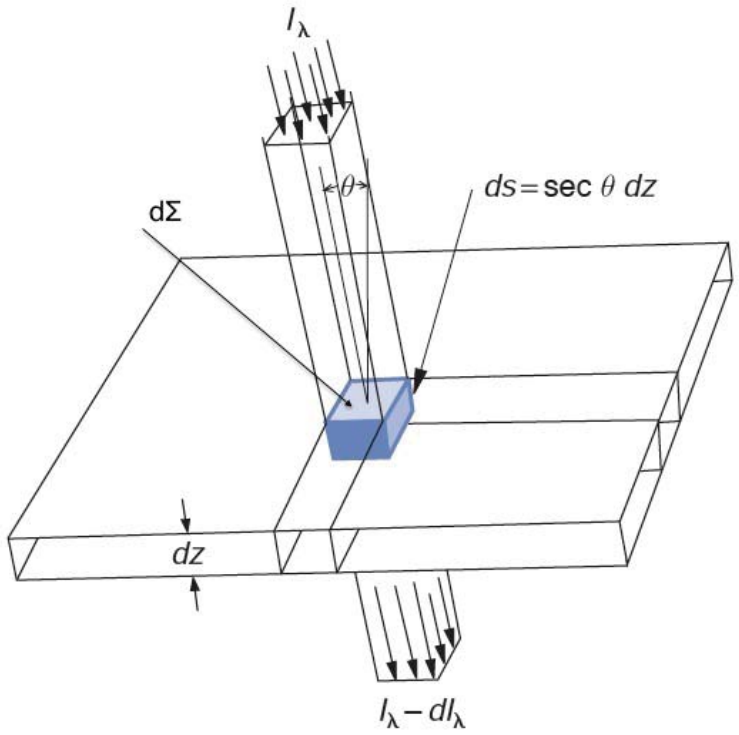

Figure 2: Extinction of a parallel beam radiation as it passes through the infinitesimally thin atmosphere (from *Wallace and Hobbs*, 2006, p123)

This simple concept of a single type of particle becomes more involved when a size distribution is involved. We leave that discussion to the Aerosol optical depth section below. The quantities I and κ are expected to be wavelength dependent. The negative sign in 1 indicates a loss in radiance when propagating through the thickness ds. Equation 1 may be integrated from a particular height (z=Z) to the top of the atmosphere (z=∞) to determine the fractional loss of the incident radiation. In this case, z is decreasing in the direction of propagation of radiation, so the negative sign disappears. Assuming horizontal homogeneity (κ is a function of z only) then with $ds = \sec\theta dz$ (Figure 2):

$$\int_Z^\infty \frac{dI}{I} = \sec\theta \int_Z^\infty \kappa(z)dz \tag{3}$$

$$\ln\left(\frac{I(\infty)}{I(Z)}\right) = \sec\theta \int_Z^\infty \kappa(z)dz \tag{4}$$

Taking the antilog of both sides yields

$$I(Z) = I_0\, e^{-m\tau} \tag{5}$$

where $I_0 = I(\infty), m = \sec\theta$ and $\tau(z) = \int_Z^\infty \kappa(z)dz$

Equation 5 is known as Beer-Lambert-Bouger law. The quantity $\kappa(z)dz$ represents an incremental measure of the *total optical depth* in the zenith direction. Its value between ground level (z=0) and the top of the atmosphere is given by:

$$\tau = \int_0^\infty \kappa(z)dz \tag{6}$$

For a plain parallel atmosphere, the air mass, m, is simply $\sec\theta$ (which is what we have been assuming above). Such a definition of m presumes that the spherical geometry of the atmosphere is not an important factor. This is generally an acceptable approximation for $\theta < 70^\circ$ (see *Thomason et al.*, 1983 for a discussion of m).

The value of τ can be decomposed as (*Shaw et al.*, 1973):

$$\tau = \tau_{ray} + \tau_{aer} + \tau_{O_3} + \tau_{H_2O} + \tau_{NO_2} \tag{7}$$

where τ_{ray} is the optical depth of molecular scattering (Rayleigh scattering) and τ_{aer} is the optical depth due to aerosols. The remaining three terms, τ_{O_3}, τ_{H_2O}, and τ_{NO_2} are the optical depths due to absorption by ozone, water vapor, and nitrogen dioxide respectively. These three molecular components dominate the molecular absorption in the visible and near infra red (NIR) regions of the electromagnetic spectrum (*Seinfeld and Pandis*, 2006). The estimation of aerosol optical involves the estimation of all non-aerosol components in order to back out τ_{aer} from equation 7.

The following subsections discuss the estimation of each of the individual components of 7 when processing starphotometry data.

3.1.2 Optical depths of atmospheric gases

Rayleigh optical depth, τ_{ray}

The value of τ_{ray} can be estimated with a help of an empirical formula derived for standard molecular profiles (*Frohlich and Shaw*, 1980):

$$\tau_{ray} = \frac{p \cdot 0.00865 \cdot \lambda^{-\left(3.916+0.074\cdot\lambda+\frac{0.05}{\lambda}\right)}}{p_0} \tag{8}$$

where p is the measured atmospheric pressure, p_0 is the standard atmospheric pressure at sea level (1013 hPa), and λ is the wavelength (in microns). There are a number of such empirical expressions in the literature : equation 8 is the one employed for our starphotometer.

Ozone optical depth, τ_{O_3}

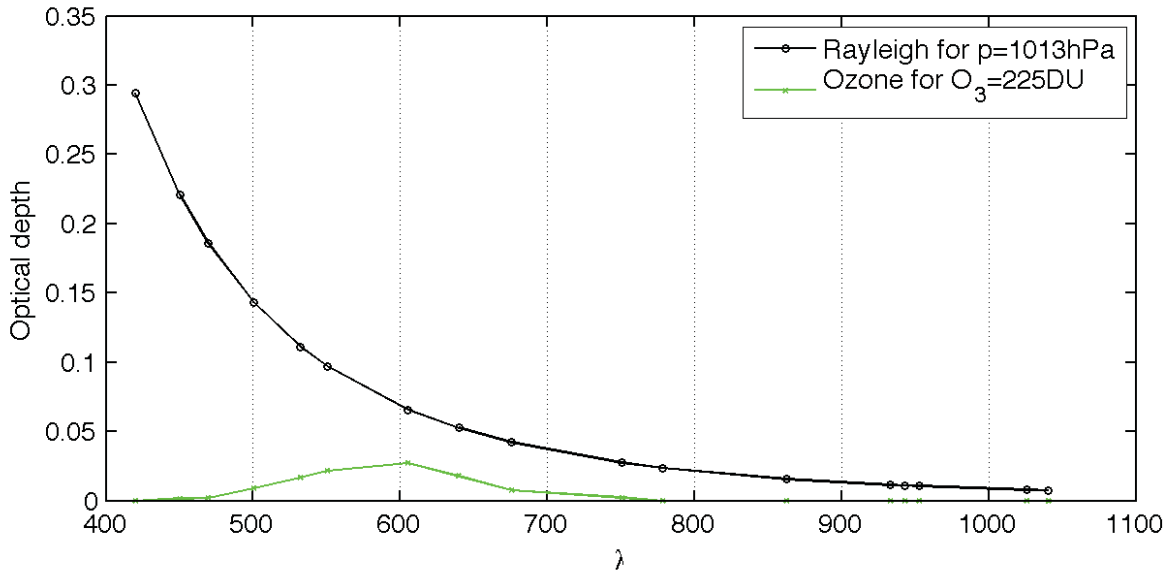

Figure 3: Typical τ_{ray} and τ_{O_3} spectra for the representative values of p=1013hPa and $[O_3]$ = 225DU

The following equation was employed for the evaluation of the ozone optical thickness (from *Schulz*, 2007):

$$\tau_{O_3} = \frac{k_{O_3}^{\lambda}\,[O_3]}{1000} \tag{9}$$

where: $k_{O_3}^{\lambda}$ is the spectrally dependent ozone absorption cross section, [milli-cm^{-1}] and $[O_3]$ is the concentration of ozone expressed in Dobson units, DU. (1 DU corresponds to 2.69×10^{16} molecules of ozone per cm^2 of atmospheric column for standard temperature and pressure (STP) conditions of T = 273°K, P = 1013 hPa). A value of 1 DU / 1000 numerically corresponds to the height in milli-cm of an atmospheric column of a given gaseous constituent if that constituent were compressed to STP conditions.

The $k^{\lambda}_{O_3}$ coefficients are presented in Table 1 (*Schulz*, 2008). Ozone absorption is negligible after 778.5nm. The units of are milli-cm^{-1}

Table 1: Spectral ozone absorption coefficients

λ(nm)	450.9	469.3	500.4	532.7	550.1	605.2	640.4	675.5	750.0	778.5
$k^{\lambda}_{O_3}$	0.003	0.018	0.031	0.065	0.083	0.123	0.079	0.038	0.008	0.0025

The ozone values used in this work were obtained from weekly balloon soundings acquired during starphotometer measurement periods. Figure 3 shows the τ_{ray} spectra from equation 8 and τ_{O_3} from equation 9 for the representative values of p=1013hPa and $[O_3]$ = 225DU.

Water vapor optical depth, τ_{H_20}

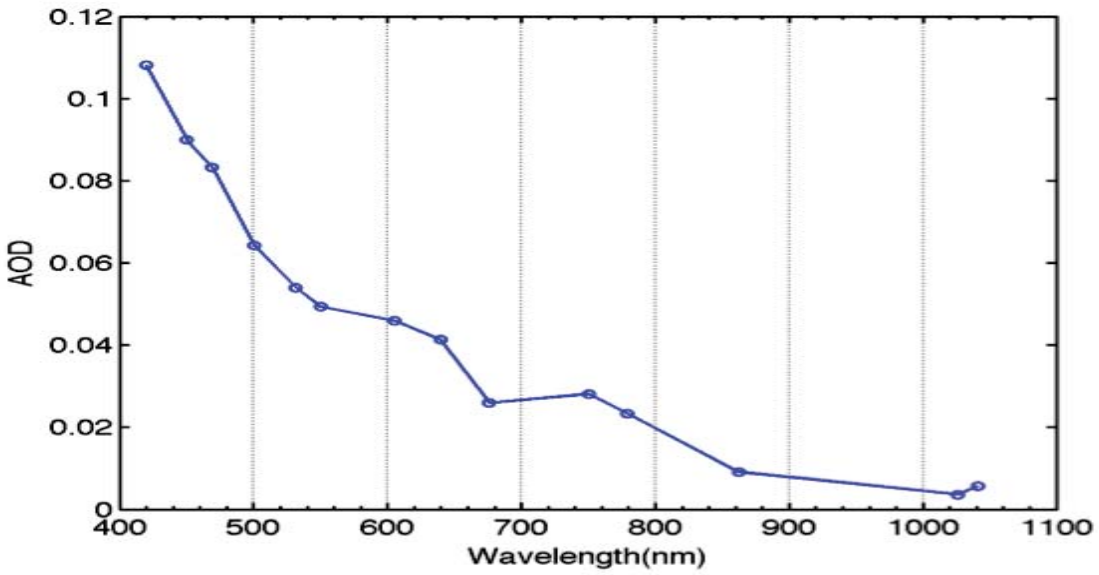

Figure 4: Typical two-star method AOD spectra obtained at Eureka on Mar 19, 2012 at 04:25UTC. The 933.5, 943.2 and 952.8nm channels are not shown as they are specifically designed for the estimation of water vapor.

To eliminate the need for water vapor correction, one usually chooses the spectral measurement bands where the water absorption is negligible and thus $\tau_{H_2O} \approx 0$. In reality this is not always a good approximation, especially in the case of the spectrally extensive infrared bands. For the discussion of the possible water vapor effects on the starphotometry AOD measurements at mid-latitudes see *Baibakov*, 2009, p.13. No water

vapor correction was performed for the visible bands principally employed in this work (420-860nm). This is justified by the very weak water vapor absorption in the measurement channels as well as by the extreme dryness of the Arctic winter atmosphere. A typical starphotometry AOD spectrum obtained at Eureka is shown in Figure 4.

One can exploit the strong water vapour absorption in the near-infrared channels about 940 nm to estimate the column integrated precipitable water vapor concentrations. In the AERONET case, a standard water vapor correction is performed by calculating the value of the water vapor content using a 940nm channel and subsequently employing this value to estimate τ_{H_2O} at all the other spectral bands (*Halthore et al.*, 1997). *Pérez-Ramírez et al.*, 2012a show how a similar water vapor content estimation can be performed from the starphotometry data.

Nitrogen dioxide optical depth, τ_{NO_2}

In the troposphere, nitrogen dioxide (NO_2) is a pollutant that can be produced through human activities such as running an automotive engine. In the stratosphere NO_2 plays an important role in the ozone chemistry. At mid-latitudes, NO_2 concentrations are highly variable and the values of τ_{NO_2} can change by more than a factor of 100 for an urban location (from less than 0.001 up to 0.175, *O'Neill*, 1999[1]). The case for values larger than 0.01, however, is weak (idem). The NO_2 cross section peaks at around 400 nm and decreases to negligible values around 550 nm where the cross section is $\approx \frac{1}{10}$ of the cross section at 400 nm. Satellite observations (such as SCIAMACHY) show similar NO_2 trends at Eureka and Ny Ålesund with the maximum summer values below $6 \times 10^{15} molec/cm^2$. These are approximately equal to ground-based measurements (for example, *Melo et al.*, 2004 report spring NO_2 values at Eureka being in the range 2-4x$10^{15} molec/cm^2$). Using the reference cross-section $5 \times 10^{-19} cm^2$ of *O'Neill*, 1999, the optical depth corresponding to 6×10^{15} molec$/cm^2$ is only: $\tau_{NO_2} = 6 \times 10^{15}$ molec$/cm^2 \cdot 5 \times 10^{-19} cm^2 = 0.003$, which is mostly negligible for the purposes of this work.

3.1.3 Aerosol optical depth, τ_{aer}

Aerosol optical depth can be calculated from 7 as a difference between the total optical depth and the sum of the atmospheric components:

[1]The NO_2 optical depth estimates we give here represent the same wavelength range employed by O'Neill, to wit; "In what follows, the NO_2 optical depths are referenced to an absorption cross section of $5 \times 10^{-19} cm^2$ or 13.4 cm^{-1} (any NO_2 cross section between 325 and 480 nm is $\geq 5 \times 10^{-19} cm^2$)."

$$\tau_{aer} = \tau - (\tau_{ray} + \tau_{O_3} + \tau_{H_2O} + \tau_{NO_2}) \tag{10}$$

Its amplitude is an indicator of aerosol abundance while its spectral form contains information on particle size and refractive index. This information partition is determined by the fundamental division of optical depth into abundance (number density) and optical cross section (σ). If $\sigma_{aer}(m, r, \lambda)$ is the extinction cross section for a single particle of refractive index m_{ri} [2] and radius r at a wavelength λ, then the total cross section per unit volume across the size distribution n(r) is given by :

$$\frac{d\sigma_{aer}}{d\Sigma dz} = \int_0^\infty \sigma_{aer}(m_{ri}, r, \lambda) n(r) dr \tag{11}$$

where $d\Sigma$ is the area facing the beam in the small volume shown in Figure 2. But, if $d\sigma_{aer}$ is the effective optical area blocking the beam, then $d\sigma_{aer}/d\Sigma$ is nothing but the fraction of the beam that is attenuated by aerosols and $d\sigma_{aer}/d\Sigma$ is the aerosol attenuation coefficient:

$$\kappa_{aer} = \frac{d\sigma_{aer}}{d\Sigma dz} = \frac{\int_0^\infty \sigma_{aer}(m_{ri}, r, \lambda) n(r) dr}{\int_0^\infty n(r) dr} \int_0^\infty n(r) dr = \overline{\sigma}_{aer} N \tag{12}$$

where N is the total number density of particles in the size distribution and $\overline{\sigma}_{aer}$ is average cross section per particle.

One can then integrate for total aerosol optical depth :

$$\tau_{aer} = \int_0^\infty \kappa_{aer}(z) dz = \int_0^\infty \sigma_{aer}(m_{ri}, r, \lambda) \int_0^\infty n(r, z) dz dr = \int_0^\infty \sigma_{aer}(m_{ri}, r, \lambda) a(r) dr \tag{13}$$

where a(r) is the column integrated differential number density or differential abundance (= dA / dr where A is the radius-integrated abundance). Accordingly :

$$\tau_{aer} = \frac{\int_0^\infty \sigma_{aer}(m_{ri}, r, \lambda) a(r) dr}{\int_0^\infty a(r) dr} \int_0^\infty a(r) dr = \overline{\sigma}_{aer} A \tag{14}$$

where $\overline{\sigma}_{aer}$ is now averaged using a differential abundance weighting scheme.

[2] particle optical property relative to the surrounding medium and, hence, an indication of particle type. $m_{ri} = n + ik$ where the real and imaginary parts, n and k, represent the particle nonabsorbing and absorbing components, respectively

3.1.4 Angstrom Exponent

The *Angstrom exponent*, α (*Angstrom*, 1964) is another key parameter in sun and starphotometery analysis. It expresses an approximate power dependence of AOD on the wavelength and is defined by the fundamental Angstrom relation:

$$\delta_\lambda = \beta\lambda^{-\alpha} \tag{15}$$

where : λ is the wavelength, expressed in microns; τ_λ is the aerosol optical depth at a wavelength λ; β is the Angtsrom turbidity coefficient (which equals τ_λ at $\lambda = 1\mu m$) and α is the Angstrom exponent.

The Angstrom exponent provides information about the size of the aerosols with the higher values of α corresponding to smaller particle sizes. Typical α values (for wavelength ranges which extend from the visible to the near IR) range from higher than 2 for small particles associated with forest fires or the sub-products of fossil fuel combustion down to nearly 0 for particles relatively large such as desert dust, sea salt aerosols and clouds (*Eck et al.*, 1999; *Schuster et al.*, 2006).

The Angstrom exponent can be calculated from two AOD measurements τ_1 et τ_2 by rationing equation 15 at the respective wavelengths λ_1 and λ_2 and taking the logarithm of both sides. Solving for α yields:

$$\alpha = -\frac{\ln\left(\frac{\tau_{\lambda_1}}{\tau_{\lambda_2}}\right)}{\ln\left(\frac{\lambda_1}{\lambda_2}\right)} \tag{16}$$

In practice α is calculated as a negative slope of a regression between the logarithm of AOD and the logarithm of the wavelength for several spectral bands. Once the Angstrom exponent is calculated, it can be used to estimate optical depth at any wavelength: equation 15. It should be noted that the standard Angstrom approach in sunphotometry presumes that spectral variation is first order in log(AOD) versus $\log\lambda$ space. This approximation serves many useful first order purposes but is known to be inappropriate (especially for certain aerosol types such as smoke; see *Eck et al.*, 1999). In such cases one must resort to second or third order AOD spectrometry. This means that the Angstrom exponent becomes wavelength dependent and can (probably should be) calculated in a differential calculus fashion at a single reference wavelength (*O'Neill et al.*, 2001a). This is, as a matter of fact, what is done implicitly in the application of the SDA algorithm

discussed below.

3.1.5 Spectral Deconvolution Algorithm

While the Angstrom exponent (equation 15) is a simple and robust indicator of average aerosol dimensions, it essentially contains a mixture of information from both the fine (submicron) and coarse (supermicron) mode particles (*O'Neill et al.*, 2001b). The simple separation of aerosols into two fundamental modes is often sufficient to study most of the aerosol phenomena related to modeling and radiative transfer processes (*O'Neill et al.*, 2001a). The fine mode, for example, is dominated by aerosols that result mainly from biomass burning (forests, agriculture, etc.) and anthropogenic pollution (industrial processes, electricity generation, etc.) The coarse mode, on the other hand, is associated with naturally produced aerosols such as desert dust (as well as clouds). Assuming a bimodal particle size distribution one can use the spectral shape of AOD in order to extract the optical information related to the fine and coarse modes (idem). In this work the task was performed with the Spectral Deconvolution Algorithm (SDA) of *O'Neill et al.*, 2003. The coarse mode optical depth has proven to be a reliable indicator of the presence of thin and homogeneous clouds (idem). The SDA was applied to starphotometry data in the range: 419.9-862.3nm.

3.2 Intensive aerosol properties

Aerosols exhibit a multitude of shapes, sizes and chemical compositions and are highly variable in time and space. This large variability can, in part, be attributed to the variety of aerosol forming processes. Figure 5 shows some main sources and sinks as well as atmospheric residence time of aerosols as a function of their size.

3.2.1 Aerosol type and single scattering albedo

Aerosol type influences such properties as the degree of absorption affecting incoming radiation and the propensity for condensation-induced particle growth. IPCC (Intergovernmental Panel on Climate Change) lists the following types of aerosols that have a measurable influence on the radiative atmospheric balance: sulphates, black carbon (BC) and organic carbon (OC) aerosols from fossil fuel burning, biomass burning aerosols, nitrates and mineral dust (Figure 6).

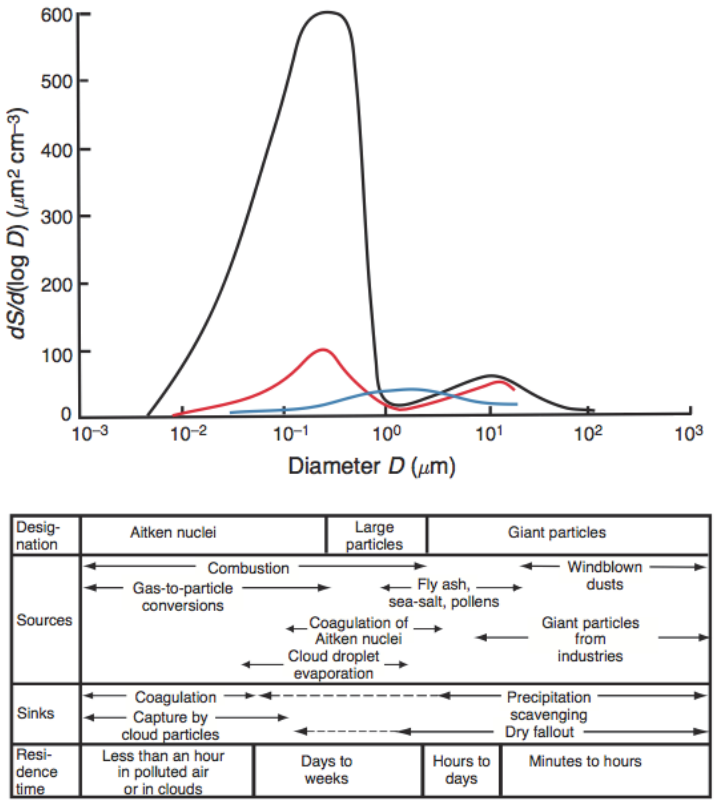

Figure 5: Particle surface area distributions ($\frac{dS}{dlog(D)}$) for urban polluted air (black), continental air (red), and marine air (blue). The differential dS is the total surface area of particles per unit volume with diameters between $log(D)$ and $log(D)+dlog(D)$. Bottom: principal aerosol sources and sinks and typical residence times in the atmosphere (both figures are from *Wallace and Hobbs*, 2006, p177).

Sulphates and black carbon are the main aerosol types emitted through human activities. They are also the most significant aerosol climate forcers in terms of their direct effect (Figure 6). They consist of sulphuric acid (H_2SO_4) particles that are partly or totally neutralized by ammonia and are present as liquid droplets or partly crystalized. The main source of sulphate aerosols is SO2 emissions from fossil fuel burning and consequent gas-to-particle conversion (72% by mass). Marine phytoplankton production, volcanic eruptions and biomass burning amount to 19, 7 and 2% respectively (*Forster et al.*, 2007, p160). Sulphates are almost entirely scattering aerosols across the solar spectrum with a small degree of absorption in the near-infrared (idem). This scattering effect amounts to net cooling in the atmosphere, thus masking, to a certain extent, the warming due to the increase in greenhouse concentrations. Over the past 20-30 years suphate emissions have

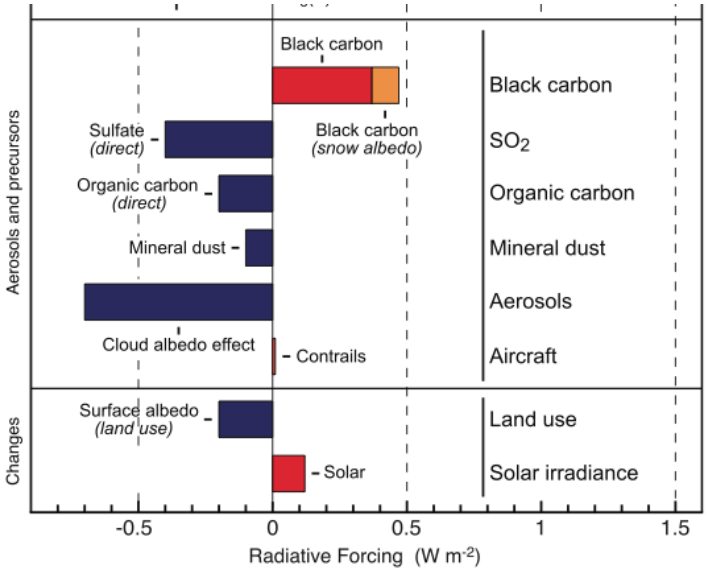

Figure 6: Components of radiative forcing for emissions of aerosols and aerosol precursors. Values represent RF in 2005 due to emissions and changes since 1750 (from *Forster et al.*, 2007, p205).

significantly decreased in Europe and USA, but have been increasing in Asia. BC aerosols are emitted directly at the source from incomplete combustion processes such as fossil fuel and biomass burning. Within hours individual particles collapse together forming densely packed clusters (*AMAP*, 2011). BC aerosols are the most efficient among the atmospheric particulates in absorbing visible light, thus causing net atmospheric warming. In reality, aerosol plumes rarely consist of a single type (except near emission sources) but rather often become mixed as they age (idem). The observed aerosol layers thus frequently exhibit both scattering and absorbing behavior. The relative contributions of scattering and absorption can be quantified at an intensive parameter level via *single scattering albedo* (SSA) defined as the ratio of scattering cross-section to the to the total (scattering + absorption) cross section of particles (*Seinfeld and Pandis*, 2006):

$$\omega_0 = \frac{\sigma_{sc}}{\sigma_{sc} + \sigma_{abs}} \tag{17}$$

3.2.2 Aerosol size

Size is one of the most important intensive aerosol properties. The modal distributions which typically characterize a multi-modal aerosol size distribution can be can be individually represented by the *effective radius* (*Hansen and Travis*, 1974):

$$r_{eff} = \frac{\int_{r_1}^{r_2} r^3 n(r) dr}{\int_{r_1}^{r_2} r^2 n(r) dr} \tag{18}$$

where r is the particle radius and $n(r)$ is the particle size distribution (number of particles per cm^2 with radius in the range r and $r + dr$ microns) and the limits or r_1 to r_2 can be taken across the approximate extent of a given mode or from 0 to ∞ in general. The variations in r_{eff} of various particle types (which typically correspond to a particular mode) influence the radiative aerosol properties (such as the spectral shape of the AOD). *Dusek et al.*, 2006 have also argued that aerosol size is more important than aerosol chemistry in cloud nucleation processes. Because of the fundamental differences in production and removal mechanisms, chemical composition and optical properties, aerosols can be often partitioned into too distinct modes: fine (submicron) and coarse mode (supermicron) aerosols (*Seinfeld and Pandis*, 2006). The fine particles can be further subdivided between the Aitken (or nucleation) mode ($r < 0.1\mu m$) and large particle or accumulation mode ($0.1\mu m < r < 1\mu m$) (*Junge*, 1955). The class names originate from the following reasons. The nucleation mode particles are usually formed by gases condensing onto existing particles[3] (nuclei). Thus formed aerosols can then coagulate together to form larger, accumulation mode particles. The name comes from the fact that the removal processes are least efficient in this mode, causing particles to accumulate (Figure 5). For the purposes of this work, however, we don't make a distinction between the Aitken and the accumulation modes. The reason for this (and the reason for the division into fine and coarse modes) is that much of the optical behavior that one observes can be largely represented by the simple model of two modes in the sub and supermicron regions (*O'Neill et al.*, 2001b).

3.3 Starphotometry measurements

Starphotometry permits the measurement of the irradiance from bright stars. The basic principle of starphotometry can be expressed by an equation similar to equation 5. Starphotometry, like astronomy, uses magnitudes which are logarithms of the measured star flux. If CN is the number of counts for a particular star measured by starphotometer,

[3]gases may also condense to form new particles

the associated star magnitude M can then be defined as:

$$M = -2.5 \log_{10}(CN) \tag{19}$$

In reality, starphotometer takes a series of brightness measurements (usually 5) of both a star and background immediately in the vicinity of the star. The CN value used in calculating the star magnitude (equation 19) is the difference between the mean star count (SC) and background count (HC):

$$CN = SC - HC \tag{20}$$

Adopting the definition of equation 19, the Beer-Lambert Law can be written in a following form (Leiterer et al., 1995):

$$M = M_0^* + 1.086\tau m \tag{21}$$

where M is the measured magnitude on the ground, M_0^* is the extra-terrestrial magnitude and m is the air mass. The factor 1.086 in equation 21 comes from the product $2.5 \cdot \log e$.

There currently exist two methods to obtain the optical depths (and consequently aerosol optical depths using equation 10) values from the starphotometry measurements: the two-star method, TSM (*Leiterer et al.*, 1995) and a one-star method which is the analogue to classical sunphotometry, OSM (*Herber et al.*, 2002).

3.3.1 Two-star method

The differential two-star method is a relative approach that does not require calibration values. It is based on the measurement of two bright stars having a substantial air mass difference. Figure 7 shows two stars (1 and 2) where M_i and M_{0i}^* are the star measured and extra-terrestrial magnitudes, respectively, m_i represents the air mass and h_i the elevation of star i. Air masses m_1 and m_2 should be selected such that $\Delta m \geq 1$, where $\Delta m = m_1 - m_2$ (*Schulz*, 2007).

Using the relationship 21 for each of the two stars and subtracting one equation from another, yields:

$$M_1 - M_2 = M_{01}^* - M_{02}^* + 1.086\tau_T(m_1 - m_2) \tag{22}$$

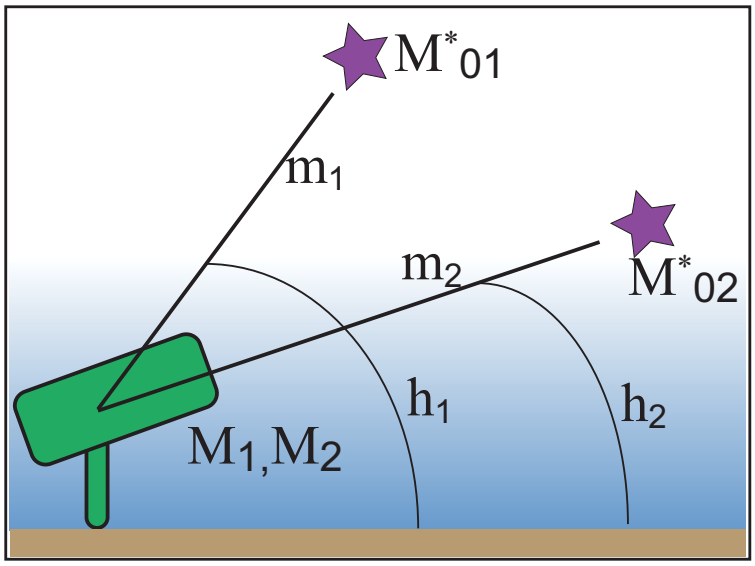

Figure 7: Conceptual diagram of the two-star measurement principle employed in starphotometry.

Solving equation 22 for τ_T yields:

$$\tau_T = \frac{1}{1.086} \frac{(M_1 - M_2) - (M_{01}^* - M_{02}^*)}{m_1 - m_2} \tag{23}$$

In TSM, starphotometer constantly alternates between the two stars, providing AOD values every 5-6 minutes depending on the length of the star centering procedure.

3.3.2 Sensitivity of the two-star method

While the TSM method is based on the inherent assumption of a horizontally homogeneous atmosphere, real atmospheric conditions exhibit some degree of inhomogeneity. It is then expected that AOD values obtained using the TSM will be sensitive to changes in the measured star magnitudes of M_1 and M_2 which are not due to nominal homogeneous differences. In general, it can be shown from equations 23 and 24 that with the other parameters held constant, a star with a greater air mass, m, (lower elevation), produces greater perturbations in the TSM signal. For details on the sensitivity of TSM, see section 3.3.2.3 of *Baibakov*, 2009.

3.3.3 One-star method

For the one-star method (OSM), one first has to establish an extraterrestrial calibration constant, M_0 - the magnitude that the instrument would measure outside of the atmosphere (Figure 8).

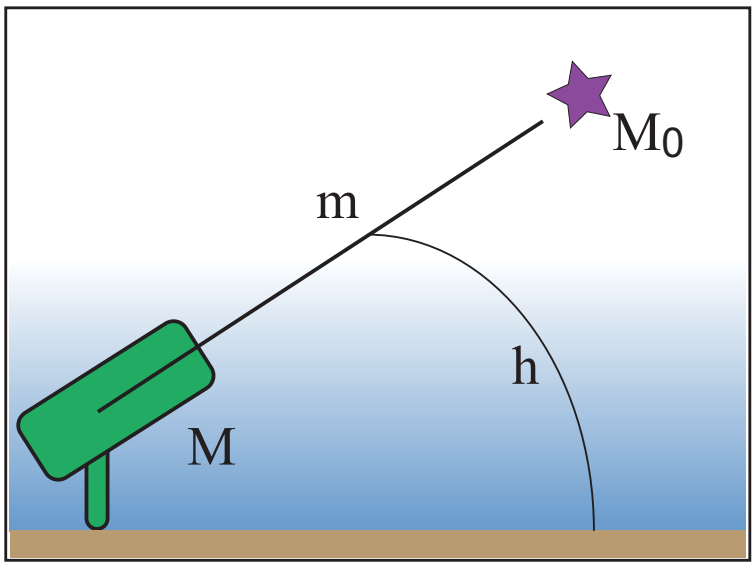

Figure 8: Conceptual diagram of the one-star measurement principle employed in starphotometry. The notation is the same as in Figure 7 except that M_0 represents the instrumental extraterrestrial magnitude

Once the M_0 values are established using calibration techniques of section 5.3.1, it is possible to calculate τ with one star:

$$\tau = \frac{M - M_0}{1.086 * m} \tag{24}$$

The OSM temporal resolution is 2-3 minutes. This method is also operationally more robust than TSM, as only one star needs to be continually followed. The accuracy of the calibration set ultimately determines the accuracy of the OSM AODs.

3.4 Lidar measurements

An atmospheric lidar (LIght Detection And Ranging) is a ranging system that operates in the optical and near IR part of the spectrum to retrieve vertical profiles of atmospheric properties. Modern lidar technology has its origins in 1960s shortly after the invention of

the laser (for a fundamental description of lidars see for example *Hinkey*, 1976; *Measures*, 1984; *Weitkamp*, 2005). Its operating principles, which are similar to (microwave) radar, are summarized in Figure 9. A laser pulse is emitted into the atmosphere (1) where, in addition to the absorption processes, it is scattered in all directions and at every altitude by the various atmospheric constituents (2). Some light gets scattered directly back to the ground and is collected by the receiver (3) which includes a telescope and highly sensitive photodetectors.

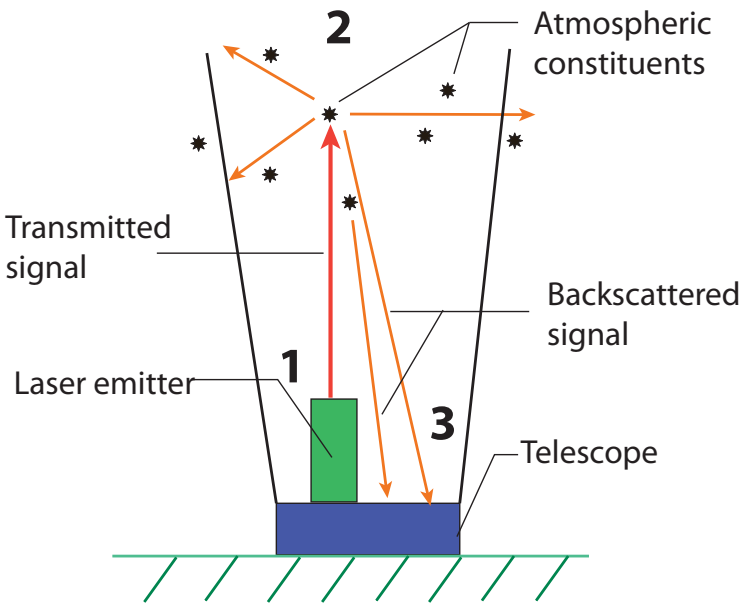

Figure 9: Lidar operating principle. (1) A laser pulse is emitted into the atmosphere; (2) in addition to the absorption processes, the light is scattered in all directions by various atmospheric constituents; (3) some of the light is scattered directly back to the ground where it is collected by the receiver optics.

Range information is provided by measuring the delay between the transmitted and return signals. Lidars are well-known for their very high spatial resolution where, in theory, scattering from an air parcel of a few cubic meters can be detected from a range of tens of kilometers (*Carswell*, 1983). Useful measurements, however, will have a lower resolution than that. The detected lidar signal can be expressed formally using the lidar equation.

3.4.1 Lidar equation

In what follows, we assume that the lidar is pointed in the zenith direction and the term 'range' refers to altitude (z). For a particular wavelength, the power P received from a distance z can be written in terms of the lidar equation (*Weitkamp*, 2005):

$$P(z) = KG(z)\beta(z)T(z) \tag{25}$$

where K is the system constant of the lidar system, $G(z)$ the quantity that describes the range-dependent measurement geometry, $\beta(z)$ the backscatter coefficient at a distance z and $T(z)$ - transmission to distance z and back

The parameters K and G(z) are completely determined by the lidar setup and are theoretically known a priori (in reality, the determination of K can be complicated and depends, in part, on the type of lidar; idem). All the information about the atmospheric parameters is contained in $\beta(z)$ and T(z). The backscattering coefficient $\beta(z)$ determines the strength of the return lidar signal and describes how much light is scattered into the backward direction (Figure 9, region 3). Assuming that the light is scattered mostly by air molecules (index 'm') and aerosols (index 'a') (*Carswell*, 1983; *Weitkamp*, 2005), we can correspondingly express $\beta(z)$ as:

$$\beta(z) = \beta_m(z) + \beta_a(z) \tag{26}$$

Some works make use of backscatter ratio defined as:

$$BSR = \frac{\beta_m + \beta_a}{\beta_m} \tag{27}$$

BSR of 1 indicates a purely molecular atmosphere without aerosols.

The transmission factor T(z) in equation 25 represents the fraction of light that is attenuated while propagating to the scattering volume and back:

$$T(z) = \exp(-2\int_0^Z \kappa(z)dz) \tag{28}$$

where the extinction coefficient, κ (equation 1), describes the combined capacity of all the particles, encountered along the outgoing and return beam trajectories, to diminish the laser beam intensity. The extinction occurs because of the scattering (other than in the backward direction) (index 'sca') and absorption (index 'abs') of light by molecules

and aerosols. We can thus express κ as :

$$\kappa(z) = \kappa_{m,sca}(z) + \kappa_{m,abs}(z) + \kappa_{a,sca}(z) + \kappa_{a,abs}(z) \tag{29}$$

where the separation into components is coherent with equation 7. The difficulty with equation 25 is that it relates profiles of one measured quantity, P(z), to profiles of two unknowns, namely backscattering coefficient $\beta(z)$ and extinction coefficient $\kappa(z)$. In order for the equation to be solvable, one needs to make certain assumptions regarding the relationship between $\beta(z)$ and $\kappa(z)$ and this is done with the (intensive parameter) lidar ratio (also known as the extinction to backscatter ratio):

$$S(z) = \frac{\kappa(z)}{\beta(z)}; S_m(z) = \frac{\kappa_m(z)}{\beta_m(z)}; S_a(z) = \frac{\kappa_a(z)}{\beta_a(z)} \tag{30}$$

where

$$S(R) = \frac{\beta_a S_a + \beta_m S_m}{\beta_a + \beta_m} \tag{31}$$

Molecular lidar ratio, S_m can be determined from Rayleigh scattering theory (eg. *Bodhaine et al.*, 1999) but the values of the aerosol lidar ratio, S_a are dependent, to a degree, on particle size, shape and refractive index (particle type) and must be estimated (eg. *Cattrall et al.*, 2005). Furthermore, while the derivation of backscatter profiles is only weakly dependent on the chosen lidar ratio, the accuracy of the resulting $\kappa_a(z)$ values, obtained from $\beta_a(z)$, is dependent on the accuracy of the estimated S_a to a much stronger degree. The output of some lidars such as CALIOP is attenuated backscatter coefficient (or attenuated backscatter ratio). This is a pseudo intrinsic optical parameter, $\beta(z)' = \beta(z) \times T(z)$, which can be derived directly from lidar backscatter signals without the need for assumptions such as a prescribed estimate of S_a (see *Campbell et al.*, 2002 for more details).

3.4.2 AOD estimates from the lidar profile

One can estimate τ_{aer} from the values of β_a by using the following reasoning. The backscattering coefficient β_a can be expressed as:

$$\beta_a \quad = \quad \kappa_{a,sca} \frac{\rho_a(\cos \pi)}{4\pi}$$

$$= \kappa_a \, \omega_{0,a} \frac{\rho_a(\cos \pi)}{4\pi} \tag{32}$$

where $\kappa_{a,sca}$ is the scattering coefficient (fraction scattered per unit length; c.f. the definition of extinction coefficient above), $\omega_{0,a}$ - aerosol single scattering albedo (equation 17), $\frac{\rho_a(\cos 180°)}{4\pi}$ is the fraction of radiation scattered by aerosols into the direction which is opposite to the incidence direction (180° scattering angle) per unit solid angle. The quantity ρ_a is called the scattering phase function (see *Hansen and Travis*, 1974, for example).

Rearranging yields:

$$\kappa_a = \frac{\beta_a}{\omega_0 \frac{\rho_a(180^{\circ})}{4\pi}} \tag{33}$$

The lidar ratio of equation 30 is accordingly:

$$S_a = \frac{\kappa_a}{\beta_a} = \frac{1}{\omega_0 \frac{\rho_a(180^{\circ})}{4\pi}} \tag{34}$$

Using equations 6 and 34 one arrives at:

$$\tau_a = \int_0^{\infty} \kappa_a(z) dz = \int_0^{\infty} \beta_a(z) \, S_a(z) dz = S_a \int_0^{\infty} \beta_a(z) dz \tag{35}$$

Once the β_a profiles are derived, they can be summed over the entire atmosphere and multiplied by a suitable lidar ratio to yield an approximation for the aerosol optical depth. The difference in the line of sight between the lidar and starphotometer, however, can result in moderate to significantly different results depending on the star choice (low or high).

3.4.3 Depolarization ratio

An inherent property of light is that the electric field (E-vector) of the electromagnetic wave at any point in time exhibits some orientation in space (*Sassen*, 2005). Pulsed lidars produce linearly polarized light with a fixed orientation of the E-vector. Interaction between atmospheric molecules and aerosols with the incident laser radiation can depolarize light by introducing a component, orthogonal to the plane of the transmitted signal, into the backscattered signal. The ratio of the measured cross-polarized power

($P_\perp$) to the co-polarized power, ($P_\parallel$) is defined as the linear depolarization ratio, DR :

$$DR = \frac{P_\perp}{P_\parallel} \tag{36}$$

DR often allows one to differentiate between the types of particles seen in lidar data. In section 1.4 we made the point that fine mode aerosols will be characterized by low DRs and therefore small DR is a necessary condition, but not a unique condition for the presence of fine mode particles (low DR might also be due to large spherical cloud droplets but then we could probably separate out that case based on the amplitude of the backscatter coefficients).

3.4.4 Color ratio

The lidar color ratio, CR, can be defined simply as the ratio of the backscatter coefficients at two wavelengths 1 and 2 : $CR = \beta_2(z)/\beta_1(z)$.

CR is sensitive to particle size in a non-monotonic fashion (see, for example, *Perro*, 2010). For example, one needs to use widely separated wavelengths (such as by mixing lidar and radar data) for the relationship to be monotonic.

It nonetheless has been employed to discriminate between generic aerosols and clouds using lidar channel pairs of 532 & 355 nm (Raman lidar) as well as radar (MMCR) / lidar channel pairs of 8.6 mm & 532 nm (*Perro*, 2010) or between fine and coarse mode aerosol / cloud components using a 1064 / 532 nm pair of channels (*Daou*, 2014).

3.5 Problems specific to the Arctic

3.5.1 Polar Winter characteristics

The polar winter is of special interest in Arctic studies. A key feature of the transport patterns in the winter is a formation of the "polar dome" - cold dry air that inhibits penetration of the warmer moist air masses. Figure 10 shows a significant extension of the Arctic front (dome limits) relative to summer time.

The Arctic winter is characterized by a special chemistry regime due to the absence of sun-driven photochemistry reactions. In the stratosphere a large-scale vortex circulation (called a polar vortex) is formed (a general description of the stratospheric processes including the polar vortex and its chemical and physical dynamics can be found in *Wallace*

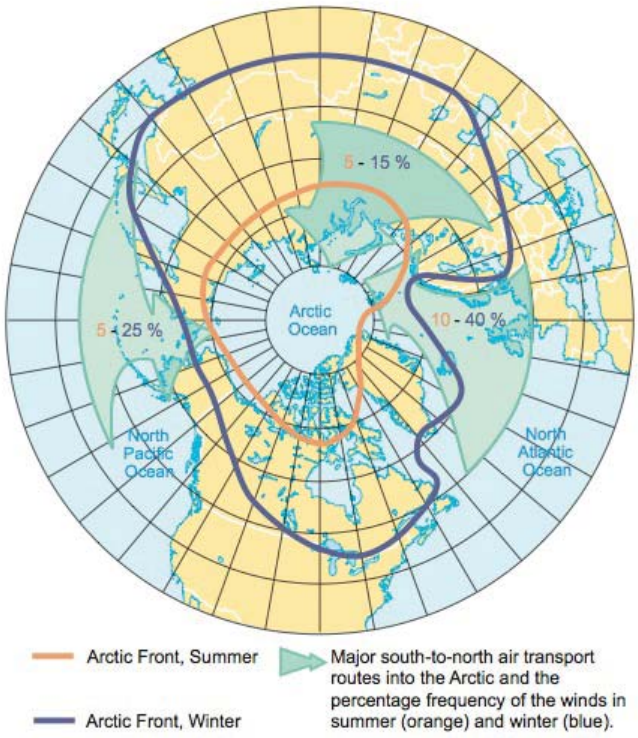

Figure 10: Polar dome boundaries during summer and winter. The percentage values refer to the frequency of the major transport routes into the Arctic (from *Quinn et al.*, 2006, p31)

and Hobbs, 2006, section 5.7 and *Mohanakumar*, 2008). Bounded at its perimeter by strong winds encircling the pole, the polar vortex serves as a giant chemical reactor that has important implications for ozone chemistry. High-level clouds, called polar stratospheric clouds (PSC), are formed at the cold core of the vortex where temperatures can fall below -80° C. Sulphate aerosols, either gradually formed (Junge layer) or rapidly injected via volcano eruptions, serve as PSC condensation nuclei. Several important reactions can occur on the surface of PSC particles resulting in liberation of active Cl (and Br) atoms from otherwise dormant reservoirs. In spring, as the sun rises, the ozone is actively destroyed through a cycle of catalytic reactions involving Cl and ClO. Human emissions of chlorofluorocarbons, a common refrigerant rich in Cl, have triggered regular and pronounced ozone losses over the Antarctic that are referred to as the ozone hole. The Arctic is less susceptible to ozone losses, as the low temperatures do not, in general, stay long enough to maintain PSCs. This, however, appears to be changing (*Manney et al.*, 2011).

During the Polar Winter period the radiation budget is almost entirely determined by longwave fluxes (starlight and moonlight are considered to be negligible shortwave sources). Such a radiative imbalance between surface emissions and the shortwave fluxes results in strong (up to $30^\circ C$ in $< 1km$) temperature inversions during the winter months (*Bradley et al.*, 1992). This corresponds to a very stable lower troposphere that inhibits vertical heat and moisture transfer as well as reduces the aerosol deposition rate.

Strong inversion layers, low atmospheric temperatures and humidity profiles, and the presence of pollution particles create complex aerosol-cloud interactions whose mechanisms and/or effects are not very well understood. Aerosols, acting as cloud condensation or ice forming nuclei (CCN or IFN) can modify cloud properties and precipitation rates in the polar winter atmosphere and can lead, for example, to the hypothesized dehydration-greenhouse effect (*Blanchet and Girard*, 1994). In this process the polluted aerosols containing sulphuric acid produce fewer nuclei on which the water vapor can condensate. This results in a larger individual particle size and, consequently, an increased precipitation rate. The net result is the faster dehydration of the atmosphere and a reduced greenhouse effect of the water vapor. Another Arctic phenomenon is "diamond dust" (suspended ice crystals, *Curry et al.*, 1990) which is most prevalent during the dark season. It is not completely understood if and when diamond dust can be radiatively important. For example, the earlier diamond dust studies were often based on subjective and at times erroneous visual observations (see *Intrieri and Shupe*, 2004 and references therein for more details). Furthermore, surrounding topography can have an important impact on the production of ice crystals. At Eureka ice crystals are reported frequently during the winter period. *Lesins et al.*, 2009 show that at least some of these ice crystals are due to the advection of snow from nearby ridges. Crystals formed in this fashion will exert a different radiative influence compared to classical diamond dust. In fact, the dehydration effect may be replaced by a net moistening of the boundary layer resulting from the higher water vapor content associated with the residual blowing snow (idem). The complexity of ice crystals processes thus warrants further observations with improved measurement techniques.

3.5.2 Aerosol transport to the Arctic regions

There are practically no local aerosol sources in the sparsely populated Arctic region. The aerosols observed in the Arctic (excluding consistently present background aerosols)

mainly originate at mid-latitudes and get transported northward. *Stohl*, 2006 highlights three main pathways of air pollution transport into the Arctic: low-level transport followed by ascent in the Arctic, low-level transport alone, and uplift outside the Arctic followed by the decent in the Arctic. The author also argues that only the last pathway is frequent for pollution from North America and Asia, while European pollution can follow all three pathways in the winter. *Koch and Hansen*, 2005 suggest, on the other hand, that South-East Asia is a dominant source of black carbon aerosols in the spring. This claim is supported by *Stock et al.*, 2012 who showed the transport of March forest fire plumes from near Khabarovsk (Russia's far East region) to Ny Ålesund in the European High Arctic. The recent modeling study of *Bourgeois and Bey*, 2011 show that 59% of all sulphate aerosols in the Arctic comes from the oxidation of SO_2 emitted in Siberia (19%), Europe (18%), Asia (13%) and North America (9%). As for the BC burden in the Arctic, Siberia, Asia, Europe and North America contribute 29, 27, 25 and 17% respectively.

During the late winter-early spring period (February-April) the polar dome shrinks in size and the established meteorological conditions facilitate pollution transport into the Arctic. The resulting effect is *Arctic Haze* - a climatologically important, anthropogenically-produced phenomenon, resulting in rapid transfer of aerosol pollution from mid-latitudes into the Arctic region (*Shaw*, 1995; *Quinn et al.*, 2007).

3.5.3 AOD dynamics in the Arctic

The ability to measure or derive polar AODs and parameters such as r_{eff} is, in terms of sunphotometry, limited to about a dozen ground-based stations spread unevenly across the Arctic and sub-Arctic region. Satellites help to mitigate the lack of spatial coverage, but the retrieval procedures are problematic during the sunlight periods because of the high-latitude viewing geometry, algorithm uncertainties over snow and ice (eg. *Istomina et al.*, 2011) and virtually non-existent for passive sensors during the polar night. Furthermore, satellite products (notably aerosol profiles from the CALIOP lidar and aerosol precursor products such as OMI[4]-SO_2) have been subject to little validation in the Arctic region.

While the Arctic is generally considered as a very pristine environment due to its remoteness and lack of local pollution sources, Arctic aerosols can achieve concentrations

[4]Ozone Monitoring Instrument

comparable to polluted mid-latitude regions (e.g. *Stohl et al.*, 2007). Seasonal variations and multi-year AOD trends for some of the Arctic locations can be found in *Bodhaine and Dutton*, 1993; *Quinn et al.*, 2007 (Barrow, Alaska), *Herber et al.*, 2002 (Ny Ålesund, Spitzbergen) and *Tomasi et al.*, 2007 (pan-Arctic stations). These works indicate that, in general, AOD values are minimal in the summer and fall and reach their maximum in late winter and early spring. *Herber et al.*, 2002 report an annual range of $0 <$ AOD < 0.2 at 532nm with continuous seasonal transitions. The maximum AOD values are associated with the Arctic Haze.

Chapter 4

Methodology

4.1 Photometry-lidar synergy

Sunphotometers and lidars are now often used in a tandem for the complementary characterization of aerosol properties. This combined use helps to circumvent, to a certain extent, the limitations associated with each instrument. Sunphotometers provide column integrated aerosol extinction at multiple wavelengths throughout the visible and near-IR parts of the spectrum (e.g. 400-1000nm). They also supply the particle size dependent Angstrom exponent. The measurements, however, do not yield any vertical information and are often impaired by cloud presence. Lidars provide vertically resolved aerosol and (optically) thin cloud profiles, but are usually limited to 1-3 operating wavelengths (e.g. 355, 532, 1064nm). Furthermore, even though the advanced Raman technique theoretically allows the direct determination of the lidar ratio, in practice it is not a straightforward task and photometric AOD data is often used for validation and comparison purposes. The column-integrated S_a value, estimated, from the sunphotometry data, can be used to constrain the integrated backscatter coefficient as per equation 35.

In general, the empirical, event-driven approach where one gains certain physical insights into the aerosol properties through the medium of example appears to be common to the community. The combination of the sunphotometry and lidar data has been employed to study various types of aerosols events at the mid-latitudes, such as dust (*Müller*, 2003; *Papayannis et al.*, 2007), pollution (*O'Neill et al.*, 2004) and biomass burning (*Balis*, 2003; *Alados-Arboledas et al.*, 2011).

In the High Arctic, the instrument synergy has been used to characterize the transported aerosol layers from forest and agricultural fires (*O'Neill et al.*, 2008; *Saha et al.*,

2010; *Stock et al.*, 2012) as well as volcano eruptions (*Hoffmann et al.*, 2010; *O'Neill et al.*, 2012). *Müller et al.*, 2004 also give optical and microphysical properties of the Arctic polluted air mass that was readvected back to Europe. A particular aerosol event is usually characterized in terms of its optical and microphysical properties. The former consist of AOD, Angstrom exponent, and volume particle size distribution from sunphotometry as well as backscatter and extinction coefficients and the S_a ratio from the lidar data. Column- or range-integrated α and colour ratio values can also be calculated from the lidar data. Effective radius and particle size distribution are the main reported microphysical properties. *Pahlow et al.*, 2006 present a mathematical formalism for the derivation of the microphysical properties from a combined sunphotometry-lidar dataset.

The validation of the physical significance of any event depends on how well one can piece together a convincing set of ground-based measurements, satellite data, model simulations and physical justifications. The dramatic improvement in spatio-temporal remote sensing coverage, instrumental quality and dimensionality as well as modeling results over the past decade has substantially increased the chances of being able to confirm a given Arctic or pan-Arctic event hypothesis. In this work we extend the holistic event-based analysis into the Polar Winter period using the starphotometry and lidar measurements at Eureka and Ny Ålesund, space-borne CALIOP lidar data and Pan-Arctic model simulations.

Chapter 5

Research sites and instrumentation

5.1 Eureka (Nunavut, 79° 59'N, 85° 56'W)

Eureka is host to an operational meteorological station in the High Canadian Arctic. It is located on the Ellesmere Island, the northernmost island of the Canadian Arctic Archipelago. The Archipelago is surrounded by the Arctic Ocean from the north and west, the Archipelago to the south and Greenland to the east.

The essential climate statistics at Eureka are given in *Lesins et al.*, 2010. The average Jan-Mar (coldest months) and Jun-Aug (warmest months) temperatures are -37° C and 3° C respectively. The prevalent wind direction in the winter is from the west. Strong surface-based temperature inversions are a consistent feature of the Eureka atmosphere. The average inversion temperature (the maximum temperature in the troposphere) is -23° C. The average values of the inversion thickness[1] and inversion lapse rate[2] are 1200m and 14° C/km, respectively.

The winters are extremely dry with an average precipitable water vapor column of less than 2mm. The atmosphere is in fact so dry that its transparency ranks Eureka among the best places in the world for astronomical observations[3] (*Steinbring et al.*, 2012) and defines the region as a desert.

Low-level humidity inversions are also common in the Arctic and result from the

[1]Height difference between the inversion temperature and the coldest temperature in the boundary layer (typically occurs at the surface)

[2]Difference between the inversion temperature and the minumum boundary layer temperature divided by the height difference between the two temperatures

[3]The extremely cold and dry air is associated with decreased infrared sky emissions and increased transmission of infrared radiation from astronomical objects.

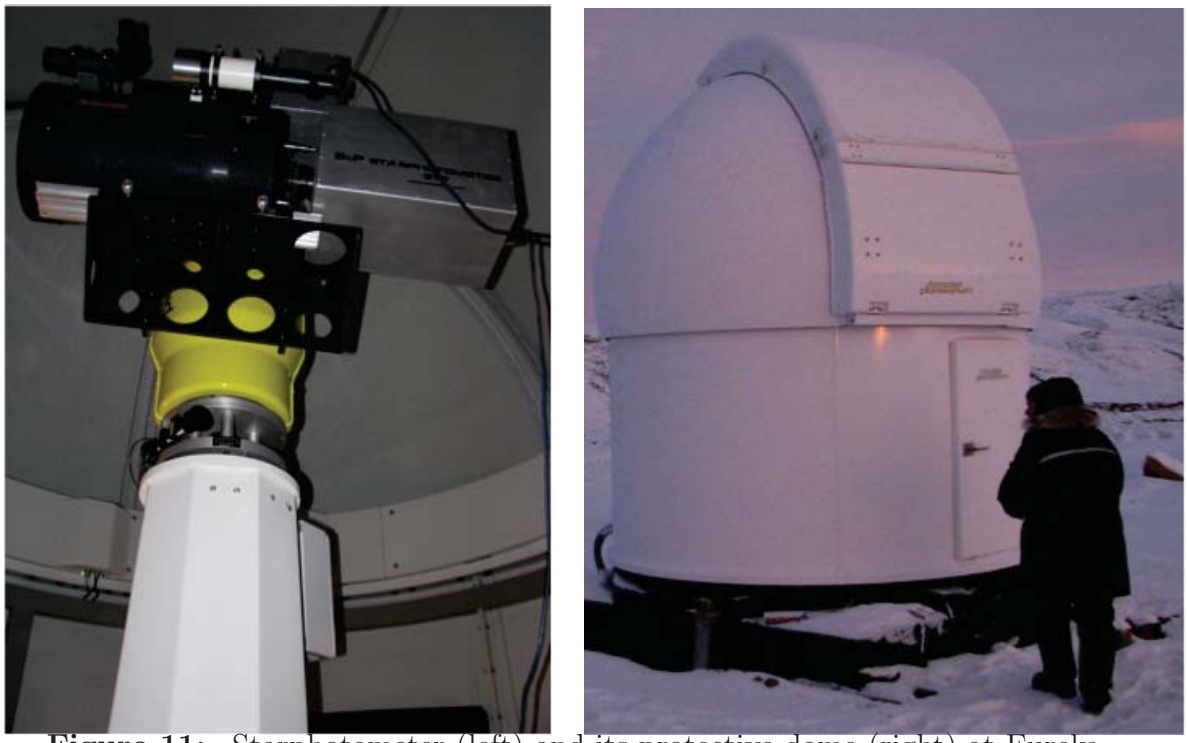

Figure 11: Starphotometer (left) and its protective dome (right) at Eureka.

advection of relatively warm moist air over the cold underlying surface (*Curry et al.*, 1995). The surface air is very close to ice saturation during the winter, which explains the persistent presence of ice crystals occurring about 50% of the time (*Lesins et al.*, 2010; *Steinbring et al.*, 2012). The consequent fallout of these ice crystals dehydrates the atmosphere, a process that can potentially be enhanced by the presence of sulphate aerosols (*Blanchet and Girard*, 1994; *Girard et al.*, 2005). The upper atmosphere on the other hand is subjected to regular water vapor intrusions occurring about 30% of the winter period (*Doyle et al.*, 2011). These large-scale intrusions drastically increase the water vapor mixing ratio[4] and the corresponding downward longwave irradiance at the surface.

In addition to hosting a meteorological station, Eureka has also served as a CANDAC (CAnadian Network for the Detection of Atmopsheric Change) research center since 2005. The CANDAC instrumentation suite is both extensive and unique, comprising more than 25 atmospheric instruments mainly divided between the PEARL (Polar Environment Atmospheric Research Laboratory, 610m altitude) and 0PAL (Zero Altitude PEARL Auxilary Laboratory, 0m altitude) sites. PEARL and 0PAL are approximately 15km

[4]A ratio of the mass of the water vapor in a parcel to the mass of the remaining dry air

apart and are complemented by a third smaller flux site (SAPHIRE) located about 5 km from 0PAL. The CANDAC scientific equipment includes an SPSTAR starphotometer (Figure 11), CRL-RMR lidars, two CIMEL CE-318 sunphotometers, an all-sky noctural imager as well as an aerosol mass spectrometer for the in situ analysis of aerosol chemical properties separated into particle size bins.

In terms of optical measurements, *Ishii et al.*, 1999 present four winter seasons of Arctic Haze observations with a Mie lidar during the period from 1993-97. The authors report on the scattering and depolarization properties of the haze, which occurs mainly in the lowest 3km. The summer time synergy of starphotometry and lidar measurements at Eureka has permitted the detection of weak forest fire plumes from Russia and Canada in the summer of 2007 (*O'Neill et al.*, 2008) and moderate strength forest and agricultural fire plumes from Russia and northern Kazakhstan in the summer of 2008 (*Saha et al.*, 2010). *Bourdages et al.*, 2009 used the combination of lidar and radar data from complete winters between 2005 and 2008 to study the following types of classes: boundary-layer ice crystals, ice clouds, mixed-phase clouds, and aerosols. The authors give the occurrence probabilities of these phenomena against depolarization, radar/lidar colour ratio and height.

5.2 Ny Ålesund (Svalbard, 78° 55'N, 11° 55'E)

The AWIPEV[5] station located at Svalbard, is a joint French-German observatory. It is located within the Ny Ålesund scientific village on the island of Spitsbergen (archipelago of Svalbard, Norway) and hosts a variety of instruments for atmospheric measurements. AWIPEV instrumentation suite resembles that of Eureka: meteorological measurements including radiosondes, a SPSTAR starphotometer, a KARL[6] Raman lidar and a sunphotometer. There is also a PREDE sunphotometer / sky radiometer and an MPLNET (continuously operating) lidar at the nearby Japanese observatory (less than a few hundred meters from AWIPEV).

The sunphotometry AOD measurements at Ny Ålesund started in 1991. The subsequent addition of the SPSTAR starphotometer in 1995 allowed AOD measurements to be acquired during the night. Figure 12 shows a continuous AOD time series during the period 1991-1999 (*Herber et al.*, 2002).

[5]Alfred Wegner Institute Paul Emile Victor
[6]Koldeway Aerosol Raman Lidar

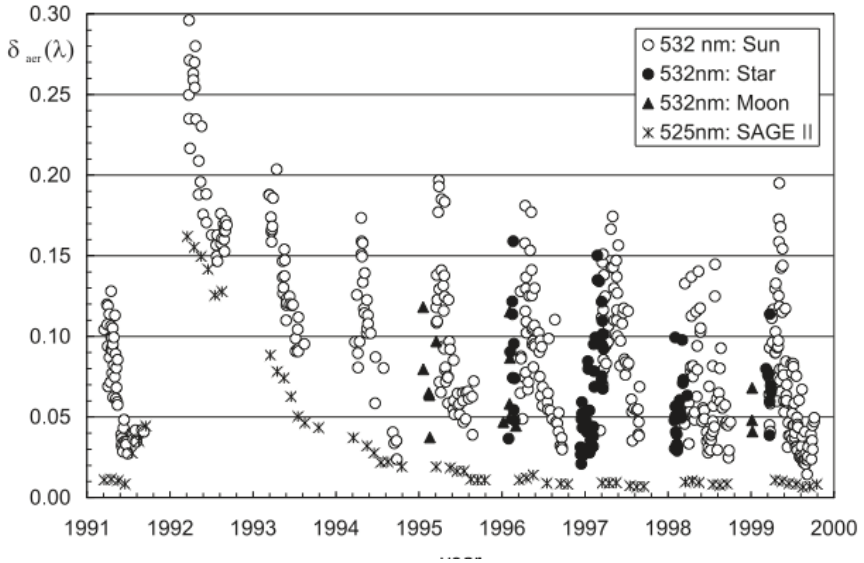

Figure 12: Annual AOD dynamics at Ny Ålesund from 1991 to 1999 (from *Herber et al.*, 2002)

The enhanced 1992-1995 AODs are due to the major Mt. Pinatubo eruption in June 1991. The Ny Ålesund aerosol concentrations, as inferred from the AOD measurements, reach their maximum in spring (March-May) with the lowest aerosol load at the end of summer (August-September).

Besides the regular Arctic Haze episodes, Ny Ålesund is often subjected to aerosol transport from mid-latitudes. *Stohl*, 2006, for example, show how North American fire plumes in 2004 impacted the whole Arctic, including Ny Ålesund. *Stohl et al.*, 2007 also describe an exceptionally strong pollution event that originated from agricultural fires in Eastern Europe. *Stock et al.*, 2012 report two early spring aerosol events detected with sunphotometry at Ny Ålesund. The first event was traced back to forest fires near Khabarovsk in Russian Far East, while the second points to the source in the vicinity of Norilsk – home to a giant nickel smelting plant north of the Arctic Circle. While in most cases the reported polluted air masses are transported from the mid-latitudes towards the Arctic, *Müller et al.*, 2004 describe an episode of Arctic Haze particles advected from the north into the European latitudes where they were mixed with urban aerosols. The Stratosphere over Ny Ålesund is characterized by the occasional volcanic aerosol events (*Hoffmann et al.*, 2010; *O'Neill et al.*, 2012) as well as more regular PSC formation during the winter period (*Maturilli et al.*, 2005; *Cordoba-Jabonero et al.*, 2009).

5.3 SPSTAR03 starphotometer

The SPSTAR starphotometer was developed by a German company (Dr. Schulz and Partner GmbH). The principal components of this instrument are depicted in Figure 13 while a schematical diagram is shown if Figure 14. These include a Celestrone C11 telescope (aperture/focal length 280mm/2800mm) to collect star light, a Baader AZ2000 altazimuth mount for precise star tracking, a viewfinder for visually observing stars, two CCD (charge-coupled device) cameras for centering a star's image on the measuring diaphragm and finally a measuring unit containing a grating spectrometer, a CCD detector and other secondary optics.

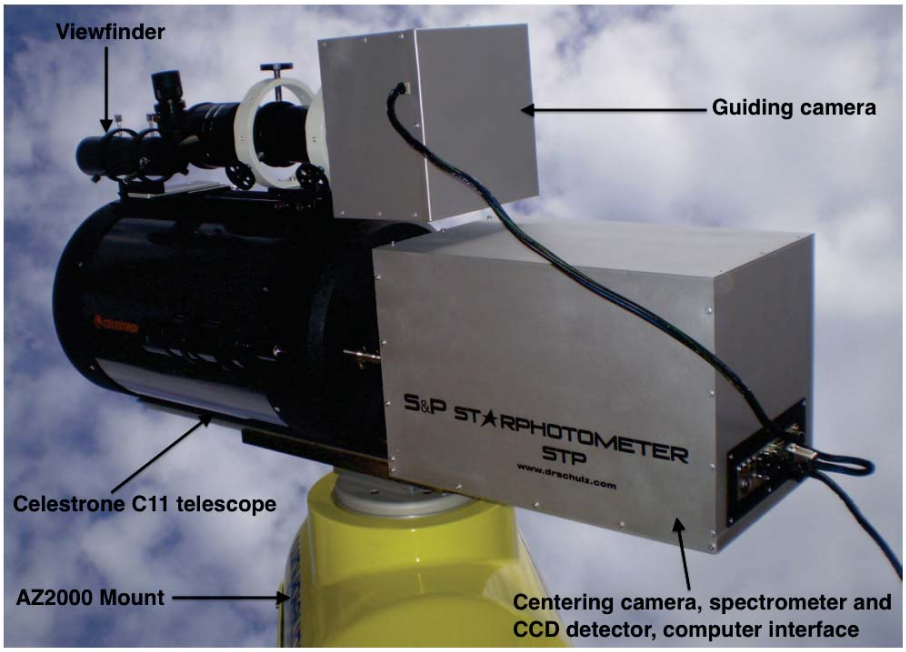

Figure 13: Principal components of SPSTAR starphotometer

Initially, the instrument is pointed towards a certain star with the help of the AZ2000 mount. The stellar light is captured by the primary and secondary telescopes and is directed to the measuring unit and guiding camera (camera 2) respectively. Inside the measuring unit, the light is divided by a beam splitter and approximately 10% of the signal is directed towards the centering camera (camera 1). Both cameras 1 and 2 are used to center the star image in the middle of the detector. The rest of the light is guided into the grating spectrometer where it is spectrally separated and subsequently measured by the CCD detector.

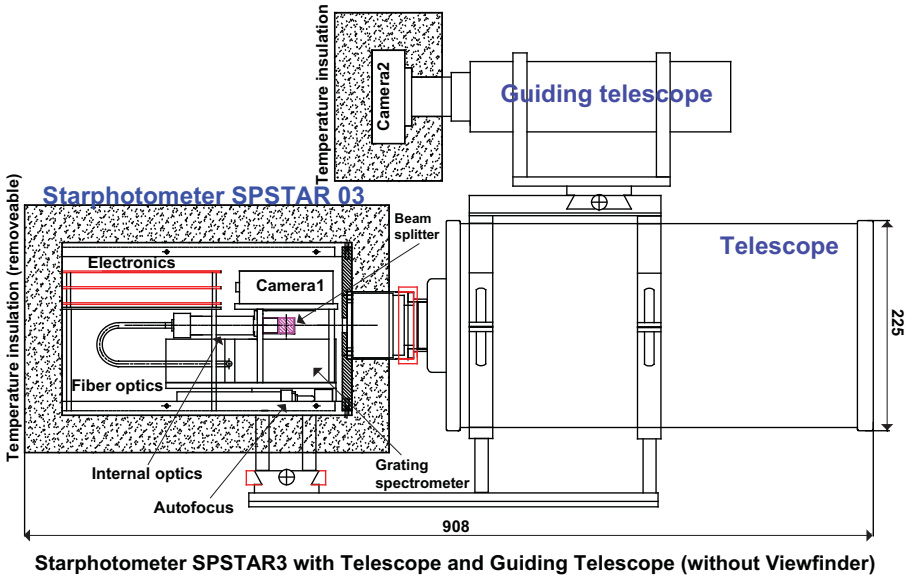

Figure 14: SPSTAR schematical diagram

The SPSTAR signal is estimated using a Hamamatsu S7031 CCD sensor that transforms the star intensity into digital numbers (CN). The CN value is adjusted to take into account the dark current (an electronic signal generated in the absence of incoming light) as well as the background irradiance of the sky and is subsequently transformed into an apparent star magnitude (M) using equation 19.

The SPSTAR takes measurements of the spectral radiance in 17 bands): 419.9, 450.2, 469.2, 500.2, 531.7, 549.8, 605.4, 639.7, 676.1, 750.7, 778.9, 862.3, 933.5, 943.2, 952.8, 1026.0 and 1040.7 nm (spectral bandwidth is less than 8nm full width half-maximum). When in the TSM mode, the measurements are taken in so-called "triplets". Each such triplet consists of a star brightness measurement of a lower elevation ("low" star), a higher elevation star ("high" star) and finally of the low star again. This allows one, by evaluating the difference between the "low-high" and "high-low" pairs of measurements, to check the stability of the atmospheric conditions. For a stable, horizontally homogeneous atmosphere this difference should be minimal.

The temporal resolution of the instrument, when in the TSM mode, is associated with the measurement time of a single triplet. This time is around 5 minutes depending on the speed of the stellar centering procedure in the measuring diaphragm. The temporal resolution of the OSM mode, where only one star needs to be continually followed, is 2-3minutes. The SPSTAR is specified to produce AOD measurements with a stated accuracy of 0.01. More details on the design of the instrument can be found in *Schulz*,

2007.

5.3.1 Starphotometry calibration

Despite the obvious advantage of TSM not requiring a priori calibration of a starphotometer, OSM is considered to be the main operational method. OSM does not necessitate atmospheric homogeneity and has a higher temporal resolution. Furthermore, *Gröschke*, 2009 argues that the accuracy and error analysis is not straight forward for TSM given its differential nature.

In order to make measurements with OSM or extract individual AODs related to the low and high stars in TSM, one needs to derive extraterrestrial star magnitudes, i.e. magnitudes that a starphotometer would measure outside of the atmosphere (M_0 in equation 24). This can be done either by using Langley-type procedures or by calculations from the TSM data. The two methods are briefly discussed below.

Langley calibration

The Langley method (*Shaw et al.*, 1973), used extensively in sunphotometer calibration, allows to estimate the extra-terrestrial sun or star signal based solely on the instrument measurements (ie. without any additional catalogue values). In this procedure one obtains a series of brightness measurements as a function of varying air mass, m. Plotting a graph (a Langley plot) of m versus $\log CN$ yields, in the presence of a stable (fixed AOD) atmosphere, a linear dependence whose intercept corresponds to the signal at zero air mass (i.e. extraterrestrial signal). Given that star magnitudes are logarithmic values (equation 19), it is useful to plot m versus M as shown in Figure 15. The intercept is equal to M_0 while the slope of the dependence corresponds to atmospheric optical depth.

Langley plots require stable atmospheric conditions and are usually performed at the high-altitude locations to avoid boundary-layer turbulence and aerosols. However, some horizontal inhomogeneities are often present even at the most stable calibration locations. To compensate for the variable atmosphere, *Gröschke*, 2009 proposed a two-star Langley calibration with one rising and one setting star. Langley starphotometer calibrations are reported in *Pérez-Ramírez et al.*, 2008b. *Pérez-Ramírez et al.*, 2011 describe a slight modification to the Langley method (called Astronomical Langley) involving a division by the air mass: the linear fit is made by plotting 1/m versus log(CN)/m. This change yields better results when a short range of air masses is used. Astronomical Langley is

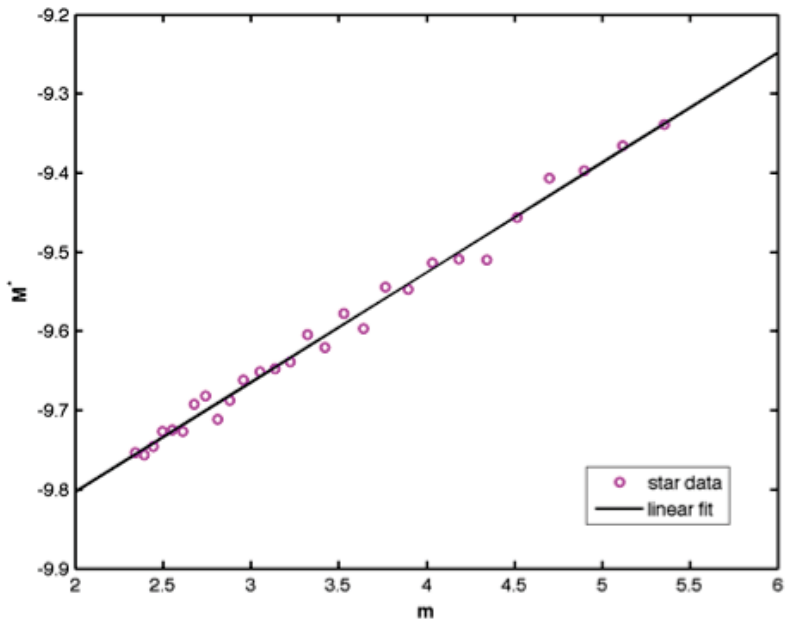

Figure 15: A typical Langley plot for star HR7001 (Vega) obtained at Izana Observatory (alt. 2390m) on Oct 14, 2008. 500nm.

also less susceptible to the atmospheric turbulence (idem).

One of the main difficulties of Langley calibration in the Arctic is that it takes many hours for some of the measurement stars to go through a sufficient air mass change (*Herber et al.*, 2002). This results in variable measurement conditions and, correspondingly, calibration inaccuracies. Another method of starphotometry calibration is using the a priori acquired TSM data.

TSM calibration

Extra-terrestrial star magnitudes (M_0) can be calculated from TSM data using equation 21. Theoretically, only one TSM point is needed to derive M_0 for a particular star. In practice however, one has to analyze at least several nights of measurements, and preferably the entire dataset, to ensure the consistency and stability of the calibration values (*Gröschke*, 2009). The problem with equation 21 is that the analysis has to be made separately for each measurement star, which is a lengthy and tedious procedure. Instead, one can analyze the difference between the measured and the catalogue extra-terrestrial magnitudes, C:

$$C = M_0^* - M_0 \tag{37}$$

Once C is established from a particular subset, M_0^* can be easily calculated for all stars using equation 37. The procedure is referred to as calibration transfer in *Pérez-Ramírez et al.*, 2008b. An advantage of this method is that every measurement, regardless of the choice of stars, can potentially be used for calibration. While theoretically it should be the same for all measurements, C often varies because of the inherent variability in the TSM data, due to contamination by clouds, ice deposition on the optics and instrumental temperature variability. As a result, several conditions should be satisfied in order to accept a calibration point. Figure 16 graphically shows the result of the consecutively applied selection criteria on the entire C dataset for 2010-12 at Eureka.

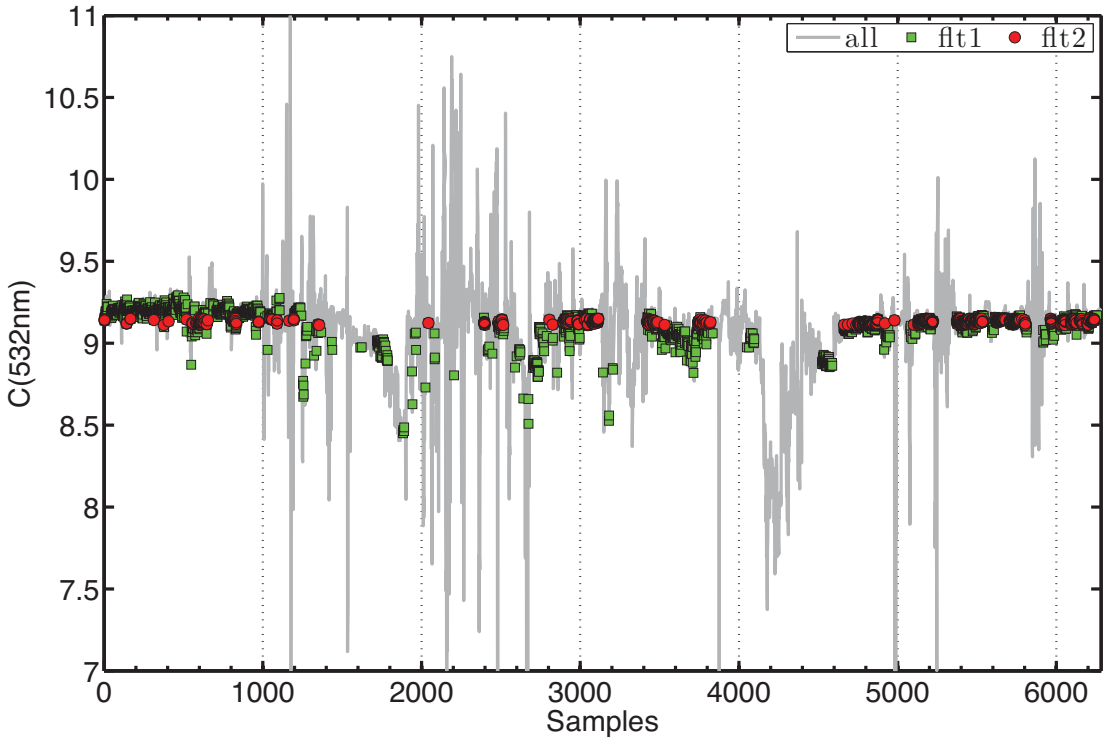

Figure 16: Results from the selection procedure of the calibration coefficient C for 2010-11 at Eureka. 'flt1' corresponds to cloud screened data in the range 0<AOD(532nm)<0.1 while 'flt2' shows only 'flt1' points satisfying the uncertainty criterion $\delta_\tau \leq 0.005$. Final calibration value is taken as a mean of all points satisfying selection criteria (red dots).

First, points identified as clouds by cloud screening algorithm (section 5.3.2) were not

considered for the estimation of C. In addition, we required that TSM values used for calibration were in the 0<AOD(532nm)<0.1 range which is representative of the Arctic atmosphere that is aerosol and cloud free (the points satisfying this initial screening are shown in green in Figure 16). Furthermore, if C is derived from a measurement associated with significant uncertainties in optical depth (δ_τ), it is not used for calibration. We used $\delta_\tau \leq 0.005$ as the selection condition which is representative of the accuracy one expects from starphotometry measurements. The resulting calibration vector was chosen as an average of the points satisfying criteria described above (red points in Figure 16).

Validation of calibration quality

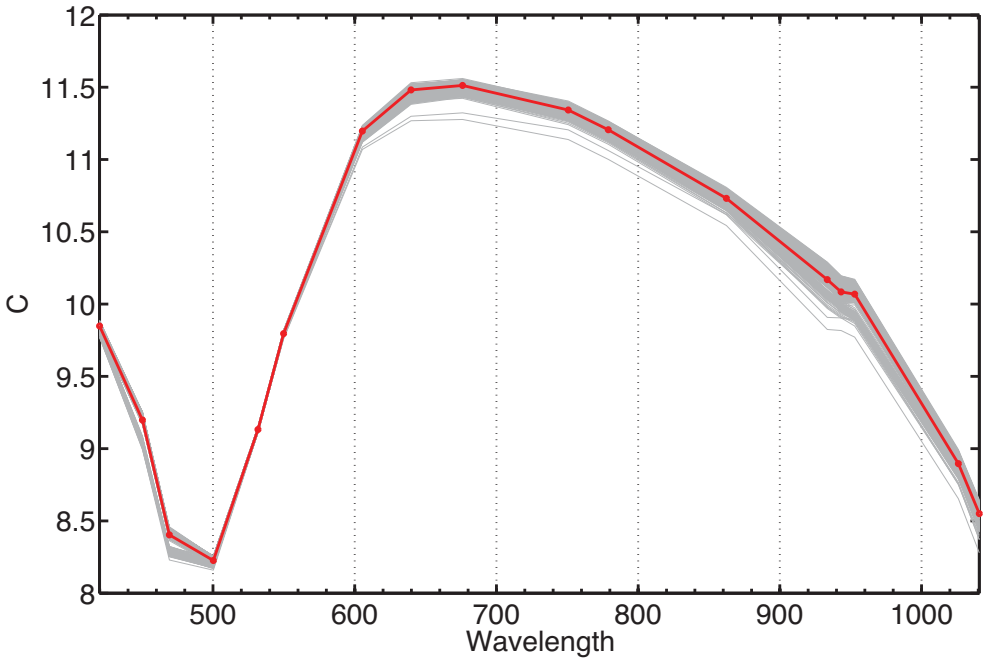

Figure 17: The spread of potential C calibration profiles that satisfy cloud screening, AOD range and measurement uncertainty criteria. The final spectral calibration values are shown in red.

Starphotometer sensitivity might change over time due to the optics degradation, optical alignment and other factors (*Baibakov*, 2009; *Gröschke*, 2009). It is thus important to monitor the evolution of the calibration values during a program of long-term measurements (months and years). Ideally, one would calibrate the starphotometer before and after each measurement season as is done with CIMEL sunphotometers at PEARL. This,

however, is extremely impractical given the complexity of the starphotometer installation and the Arctic shipping logistics. The procedure described above, nevertheless, presents a robust way to monitor calibration quality. The entire seasonal dataset is taken into account. Figure 17 shows the spread of potential C calibration spectral profiles, from which a final (mean) calibration curve is obtained. The mean standard deviation for the bands in the range 420-862nm was 0.027 corresponding to the AOD error of 0.025 (see Section 5.3.5 for details on error analysis) .

5.3.2 Cloud screening procedure

Photometry data needs to be routinely cloud screened to yield aerosol trends. *Smirnov et al.*, 2000 describe an algorithm based on temporal AOD variations used in the AERONET global sunphotometry network. Similarly, *Pérez-Ramírez et al.*, 2012b apply temporal cloud screening procedures (such as a moving average test) to starphotometry datasets. While this latter algorithm provides a consistent method to remove cloud-contaminated points, the approach and the necessary thresholds should be adapted based on the dataset (*Pérez-Ramírez*, 2012). We expect for example, that the Arctic atmospheric phenomena are optically different from those at mid-latitudes. The filters employed in this work are described in Table 2.

Table 2: Cloud filter protocol employed in this work. The three filters of the table are meant to be employed sequentially

Filter name	Condition	Description
1. Range	$0 < \tau < 0.35$	AOD values should lie within a climatologically defined range. All the points outside the range are removed
2. Moving slope	$a \leq 2$	Each point is taken as a middle of a 1h interval. The point is eliminated if the slope of the linear fit (y=ax+b) for 1h-data exceeds an empirically chosen threshold
3. Outliers	$\lvert\tau - \tau_{avrg}\rvert < 2.5\sigma$	A point is eliminated, if its difference relative to the average value for the whole night exceeds 2.5 standard deviations (σ). The procedure is repeated until all the differences are within 2.5σ

The filters of 2 are based on the methodology proposed by *Smirnov et al.*, 2000 and *Pérez-Ramírez et al.*, 2012b. Clouds are significantly more variable in time than aerosols, hence one of the main cloud filtering tests is an AOD temporal derivative. *Smirnov*

et al., 2000 defined a "triplet stability criterion" that employs three measurements taken 30 seconds apart over a total of a 1-minute period. For the cloud-free atmosphere, the difference between the maximum and the minimum AODs should not exceed 0.02, i.e. $(\tau_{max} - \tau_{min}) < 0.02$. However, in starphotometry the temporal resolution is significantly lower – 1 measurement every 3-10 minutes – and the triplet stability criterion is not directly applicable. Instead, *Pérez-Ramírez et al.*, 2012b used an absolute difference of 0.03 between two consecutive AOD values as a filtering condition, which essentially amounts to $d\tau/dt < 0.006/min$ for two measurements taken 5 minutes apart. This test turned out to be effective for many cloud scenes, except for temporally homogeneous clouds. We thus chose to use the moving slope as the main filtering criterion. The moving slope and the time derivative filters are similar and perform comparably, but the former is also sensitive to the short-duration (1-1.5h) homogeneous clouds (or coarse-mode features). We found that the empirically chosen 1h period performed well for the starphotometry datasets. One hour filtering is also used by *Pérez-Ramírez et al.*, 2012b to avoid the inclusion of any outliers.

The outliers filter of Table 2 is also a standard cloud-screening test considering that outliers are very likely to be clouds because of the high frequency variations associated with the latter. We have adjusted the threshold from 3σ of *Smirnov et al.*, 2000 and *Pérez-Ramírez et al.*, 2012b down to 2.5σ given the observed variations in AOD.

Finally, the range condition was applied to minimize the weaknesses of the other two filters in relation to cloud-dominant periods and/or homogeneous clouds. The threshold of 0.35 was chosen as an upper boundary of AOD in the Arctic based on the statistics of *Herber et al.*, 2002 and *Tomasi et al.*, 2007. It is expected that each filtering condition will have its own drawbacks. For example, the outliers filter will be dependent on the fraction of the cloud-free points in the time series, i.e. if the mean AOD value is too high, some cloud-contaminated values will be left in. When applied consecutively, however, we have found that most of the high-frequency variations associated with what we interpret as cloud features are removed.

Temporal cloud screening, nevertheless, can not eliminate homogeneous clouds with small point-to-point variations nor can it avoid eliminating highly variable aerosol events such as the incursion of a strong (fine mode) smoke plume (*O'Neill et al.*, 2003). A way to check the performance of the cloud filtering is to use the available spectral information to distinguish between clouds and aerosols (ibid). In fact, the coarse mode of the spectral deconvolution algorithm (SDA) is in most Arctic cases associated with large super-micron

cloud particles[7]. If aerosol optics are dominated by fine mode aerosols (as they are in the Arctic) then the application of the method results in a de facto cloud screening algorithm whose output can be compared (or combined) with a temporal cloud screening algorithm. Quantitatively, one can evaluate the root-mean square difference, δ_f, between the fine-mode AOD, τ_f and the temporally cloud-filtered AOD, τ_{flt}:

$$\delta_f = \sqrt{\frac{1}{N}\sum(\tau_f - \tau_{flt})^2} \tag{38}$$

where N is a total number of points in a time series.

We also compared the performance of the cloud filtering procedure with the lidar vertical profiles. In many cases, clouds tend to greatly enhance (and sometimes saturate) the lidar backscatter return. Evaluating the vertically integrated lidar signal (lidar optical depth) relative to the τ_{flt} (while being able to visually confirm the presence of cloud from its typically unique appearance as a high frequency, high intensity perturbation in the backscatter coefficient profile) is thus a natural way to ensure the quality of cloud screening.

Finally, we wanted to test the capacity of the BSRN data to serve as an additional validation method for cloud screening. BSRN (Baseline Surface Radiation Network) is a radiometric network related to climate research that, among others, include measurements of the up- and downwelling infrared radiation made using infrared radiometers such as Eppley Precision Infrared Radiometer (*Fairall et al.*, 1998). Considering that clouds are strong emitters of infrared radiation, the difference between the outgoing and incoming radiation, δ_{IR}, should be reduced in the presence of clouds compared to the cloud-free atmosphere (*Herber*, 2012). We analyzed δ_{IR} at Ny Ålesund in conjunction with the starphotometry and lidar data.

5.3.3 Calculation of optical depth uncertainty due to uncertainties in the star and background counts

If δ_{SC} and δ_{HC} are the uncertainties associated with the calculation of SC and HC (equation 20), respectively, then the RMS error in CN associated with a presumed random error in the SC and HC signals is simply the root of the quadrature sum:

[7]the course mode is also associated with large-size aerosols, such as desert dust, volcanic ash and marine salt

$$\delta_{CN} = \sqrt{\delta_{SC}^2 + \delta_{HC}^2} \tag{39}$$

where δ_{SC} and δ_{HC} are the RMS errors of the component measurements. The OSM RMS optical depth error associated with this measurement noise is then given by: $\delta_{\tau_{CN}} = \frac{1}{m}\frac{\delta_{CN}}{<CN>}$, where <CN> is the count average over the same sampling period as the RMS error estimates.

5.3.4 Sources of measurement and calibration errors

A variety of internal (related to the photometer itself) and external (related to the environment and pointing accuracy) factors can results in starphotometer measurement errors and inconsistencies. Most of the instrumental issues, such as detector linearity and temperature sensitivity as well as dark current, are discussed in detail in *Pérez-Ramírez et al.*, 2008b,a and *Gröschke*, 2009. Starphotometry AOD errors, nevertheless, can have multiple other sources. For example, TSM measurements are sensitive to the horizontal homogeneity of the atmosphere while the accuracy of the OSM measurements is directly dependent on the choice of the calibration values. Furthermore, some of the SPSTAR visible bands can suffer from inaccurate ozone (and possibly NO_2) correction, while the infrared channels can be affected by water vapor absorption. Setting aside the cases of the water vapour sensitive NIR channels (which we did not employ in this thesis) we can consider the impact of ozone, the most important gaseous absorber in the visible spectra region. Using equation (9) and an estimated ozone uncertainty of 31 DU (standard deviation from Eureka ozonesonde data) will result in a $\delta_{\tau,ozone}$ of 0.004 at 605 nm and 0.001 at 500 nm. This is substantially less than the nominal starphotometry calibration error of $\delta_{\tau,cal} = 0.01$ but is not insignificant (similar estimated errors were obtained for Ny Ålesund). The value of NO_2 optical depth that we employed for our NO_2 corrections (0.003 as per Section 3.1.2) was likely slightly high because of the tendency of NO_2 abundance to increase with the oncoming spring and summer season : measurements over Eureka during the late Polar winter of 2004 showed NO_2 columnar abundances between approximately 1.0 and 2.0 x 10^{15} molecules-cm^{-2} (*Kerzenmacher*, 2005). This yields an average range of τ_{NO_2} between approximately 0.0005 and 0.001 in the range of UV and visible wavelengths that are important to sunphotometry and starphotometry (*O'Neill*, 1999). A conservative estimate of the NO_2 relative optical depth error will thus be 100% (i.e. an absolute error 0.003). The estimated error in the

Rayleigh optical depth as given by *Frohlich and Shaw*, 1980 is 0.001% for the wavelength range of 300 to 900 nm : this yields a maximum Rayleigh optical depth error of 0.00043 at 380 nm. While this may be a bit optimistic for the Arctic (*O'Neill*, 2013) it is most likely of the correct order of magnitude and therefore negligible compared to O_3 and NO_2 errors.

One of the critical issues in starphotometry is pointing and tracking accuracy. During the duration of the brightness exposures (usually 5-30 seconds), a star image needs to stay within the detector sensitive region ("measuring diaphragm"). Cold Arctic temperatures can render the mount mechanics more difficult to perform precise tracking movements while moderate winds (>8 m/s) can shake the instrument. These two effects were minimized at PEARL by using the AZ2000 mount and a Baader dome. Both were designed to perform in the coldest environments, down to -80° C. The slit-type dome blocks the wind from everywhere but the pointing direction. The AOD is overestimated if a portion of the star signal is lost due to the star image not being entirely within the measuring diaphragm. We also encountered a problem when background exposures (designed to be void of any star signal) were contaminated by the star image not being completely outside of the measuring diaphragm. This overestimates background counts HC in equation 20 and equally results in overestimated AOD. Starphotometry measurements can be affected by light scattered in from other sources such as Moon or artificial lightning (light pollution). However, the small starphotometer FOV actually represents one distinct advantage over sunphotometry. In sunphotometry, the FOVs must be significantly larger than the solar disk of approximately 0.5° : scattering effects by aerosols and clouds (especially the latter) into a photometer FOV can result in a significant optical depth underestimation (*Shiobara and Asano*, 1994). For example the AERONET FOV is 1.2° or 4 times the starphotometer FOV : for the worst case of cloud-sized particles, the AERONET optical depth would be underestimated by ≈50% while the starphotometer error would be only about 6% of the sunphotometer error). One of the persistent measurement problems at PEARL was the ice/ice crystals condensation on the starphotometry optics. This issue is discussed in the following section.

Ice condensation effects

Ice condensation on the telescope is a known issue in polar astronomy and starphotometry, especially during the Polar Night where one must confront conditions of extreme temperature inversions and heat loses (*Durand et al.*, 2007; *Gröschke*, 2009). As an ex-

ample, Figure 18 shows an AOD time-series taken with a starphotometer (similar to that of Eureka) at Barrow, Alaska on Mar 14, 2013.

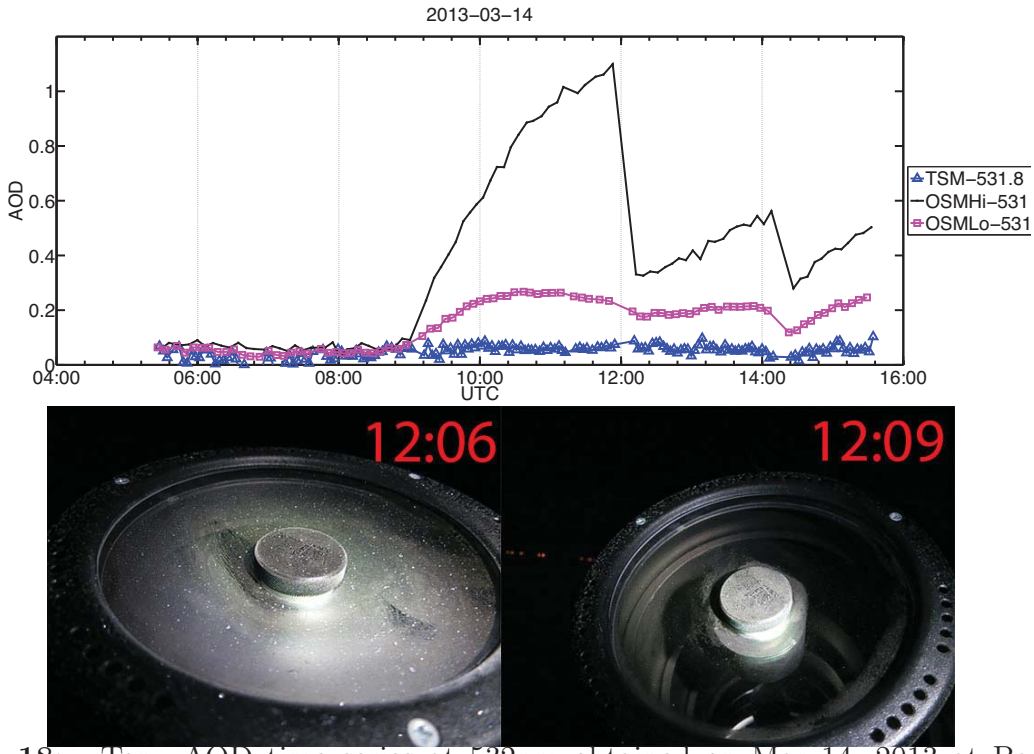

Figure 18: Top: AOD time series at 532nm obtained on Mar 14, 2013 at Barrow, Alaska. The increase in OSM AODs after 9:00 is due to ice condensation on the telescope. Bottom: photographs of the telescope before and after cleaning (left and right respectively) around 12:00

The top plot shows that both the TSM and OSM AODs stay relatively constant in the beginning of the night. Starting at 9:00, however, there seems to be an apparent increase in OSM AODs, followed by drastic drops around 12:00 and 14:20. The gradual increase was for the most part due to ice condensation on the telescope. In fact, the times associated with AOD drops are precisely those when the telescope was cleaned. The bottom of Figure 18 shows the photographs of the telescope before (left) and after (right) it was cleaned around 12:00. Points affected by ice deposition can be detrimental to the quality of the calibration values and/or OSM measurements and should be excluded from the calculation of C. That being said, it is not obvious how one can detect and characterize ice measurements. Most solutions to the icing problem involve elaborate heating procedures (idem) that are not yet technically feasible at Eureka. Instead, we have relied on the relative TSM-OSM differences, lidar data and, whenever possible, visual observations to detect AOD pseudo-increases similar to those of Figure

18. Furthermore, with the starphotometer dome closed, the ice condensation sublimates completely within hours, making it an acceptable solution in the short-term. Recently we incorporated a fan system and cameras to monitor and periodically clean the telescope remotely at Eureka.

5.3.5 Estimated total error in τ_{aer}

The total AOD error is a function of the errors in all the component parameters employed in its retrieval. Expressing equation (5) in terms of numerical counts yields :

$$CN = CN_0 e^{-m\tau} \tag{40}$$

where CN_0 is the extraterrestrial numerical count value for a given star at a given wavelength. Differentiating this expression yields:

$$dCN = e^{-m\tau} dCN_0 + CN_0(-m\tau)e^{-m\tau} \tag{41}$$

$$dCN = \frac{dCN_0}{CN_0} - md\tau \tag{42}$$

$$d\tau = \frac{1}{m}\frac{dCN_0}{CN_0} - \frac{1}{m}\frac{dCN}{CN} \tag{43}$$

Using equation (7) we can solve for the total error in the aerosol optical depth :

$$d\tau_{aer} = \frac{1}{m}\frac{dCN_0}{CN_0} - \frac{1}{m}\frac{dCN}{CN} - d\tau_{ray} - d\tau_{O_3} - d\tau_{NO_2} - d\tau_{H_2O} - etc \tag{44}$$

We will, from this point on, assume that Rayleigh optical depths errors are negligible and that H_2O optical depth errors are negligible in the UV and visible spectral regions (as per Section 5.3.4). Assuming that all remaining errors are randomly distributed, an average over a large number of samples at a given solar air mass will yield the mean square sum;

$$\langle d\tau_{aer} \rangle = \sqrt{\left(\frac{1}{m}\right)^2 \langle \left(\frac{dCN_0}{CN_0}\right)^2 \rangle + \left(\frac{1}{m}\right)^2 \langle \left(\frac{dCN}{CN}\right)^2 \rangle + \langle (d\tau_{O_3})^2 \rangle + \langle (d\tau_{NO_2})^2 \rangle} \tag{45}$$

We then approximate the differentials by their RMS difference relative to their true

value and the denominators by their mean to obtain ;

$$\delta(\tau_{aer}) = \sqrt{\left(\frac{1}{m}\right)^2 \left\{ \left(\frac{\delta(CN_0)}{\langle CN_0 \rangle}\right)^2 + \left(\frac{\delta(CN)}{\langle CN \rangle}\right)^2 \right\} + \delta^2(\tau_{O_3}) + \delta^2(\tau_{NO_2})} \tag{46}$$

In order to obtain an approximate estimate for $\delta(\tau_{aer})$ we set $\frac{\delta(CN_0)}{\langle CN_0 \rangle} = 0.024$ (Section 5.3.1), $\delta(CN) = 1$ (Section 5.3.3), a minimum[8] value for $\langle CN \rangle$ of 75 , $\delta(\tau_{O_3}) = 0.004$, and $\delta(\tau_{NO_2}) = 0.003$ (Section 5.3.4).

This then yields a total estimated error of;

$$\delta(\tau_{aer}) \lesssim \sqrt{\left(\frac{1}{m}\right)^2 \left\{ (0.025)^2 + \left(\frac{1}{75}\right)^2 \right\} + 0.004^2 + 0.003^2} \tag{47}$$

For m=1, $\delta(\tau_{aer}) \lesssim 0.03$.

AOD error in terms of the magnitude calibration constant (C)

Equation (37), written in terms of irradiances is;

$$C = M_0^* - M_0 = -2.5\, log \frac{F_0^*}{F_0} = -k\, ln \frac{F_0^*}{F_0} = k\, ln \frac{F_0}{F_0^*} \tag{48}$$

where the symbol F represents an irradiance dependent quantity (i.e. digital counts, CN, in the case of the starphotometer), "log" refers to "log10" and $k = 2.5\, log(e) \simeq 1.086$. The above expression underscores that the constancy of C (meaning it is only a function of the optics of the system) translates into a fixed starphotometer-irradiance to star-catalog-irradiance transformation ratio, viz;

$$\frac{F_0}{F_0^*} = K \tag{49}$$

where $C = k\, lnK$. Accordingly a differential (error) in C can be expressed as ;

$$dC = k\, dln \frac{F_0}{F_0^*} = k \left(\frac{dF_0}{F_0} - \frac{dF_0^*}{F_0^*} \right) \tag{50}$$

If we assume that the error of the star catalog fluxes are relatively small then expression becomes;

[8]this is a typical low value; CN counts vary in general from <10 to >7000 (420-862nm). In 2010-11 the mean CN value for Eureka was 610

$$dC = k\,\frac{dF_0}{F_0} \tag{51}$$

so that $\frac{dF_0}{F_0}\left(\frac{dCN_0}{CN_0}\right)$ can be replaced by $\frac{dC}{k}$ in equation (45) (and by a similar argument, $\frac{dF}{F}\left(\frac{dCN}{CN}\right)$ can be replaced by $\frac{dC}{k}$) to arrive at the RMS equation (46) expressed in terms of the mean square error in C.

AOD error due to incomplete cloud screening

The estimate of $\delta(\tau_{aer})$ above is for the list of error contributions that are readily quantified with some coarse degree of accuracy (or they can be highly inaccurate but very small). It also precludes "catastrophic errors" such as significant ice condensation on the optics or serious tracking errors in the star measurement or background measurement modes (as discussed in Section 5.3.4). The oftentimes inadequate nature of temporal cloud screening remains an error source which is highly variable. If we anticipate the results of our spectral versus temporal cloud screening comparison (Section 6.4) in the presence of (spatially inhomogeneous) clouds whose presence is readily filtered out (Figure 35) then we can at least get out an order of magnitude error associated with the shortcomings of temporal cloud screening in the presence of substantial clouds. Based on the RMS computations for the illustrative case of Figure 35 we obtain $\delta(\tau_{aer,post-cloud-sreening}) \lesssim 0.03$, a number which will be inflated by, for example, inaccuracies in the retrieval of τ_f and the possible presence of thin homogeneous cloud. This is an attempt to describe a worst case scenario : in the absence of competitive coarse mode signal, $\delta(\tau_{aer,post-cloud-sreening})$ will be significantly smaller.

5.4 CRL and KARL lidars

In this work we used the data from two lidar systems: the CANDAC Raman lidar (CRL) at Eureka and the Koldewey Atmospheric Raman Lidar (KARL) at Ny Ålesund. The essential characteristics of the lidars can be found in *Nott et al.*, 2012 and *Hoffman*, 2010 for CRL and KARL respectively. Both systems use the Raman technique to independently estimate the κ_{aer} and β_{aer} coefficients in 30. For the elastic or Rayleigh scattering channel, the frequency of the scattered photon is the same as the frequency of the incident photon. For the Raman or inelastic scattering channel, an incident photon changes the internal energy state of specific types of molecules in the path of the beam.

The resulting frequency shift of the scattered photon can be used to separate molecules from aerosols as the latter undergo only elastic scattering. Considering that the elastic lidar return signal is affected by both $\kappa_{aer}(\lambda_{elastic})$ and $\beta_{aer}(\lambda_{elastic})$, but the Raman lidar return by $\kappa_{aer}(\lambda_{inelastic})$ and $\beta_{Raman}(\lambda_{inelastic})$, the two profiles can be ratioed to obtain the backscatter ratio of total to molecular backscatter (and in the process eliminate K and G(R). Since the molecular backscatter coefficient can be derived from meteorological or standard atmosphere profiles and multiplied by the backscatter ratio, one obtains the total backscatter coefficient profile from which the aerosol backscatter coefficient profile can be extracted (again from a knowledge of the molecular backscatter coefficient). The process requires estimating $\kappa_{aer}(\lambda_{elastic})$ from $\kappa_{aer}(\lambda_{inelastic})$ using, for example, the Angstrom relationship (*Weitkamp*, 2005). Raman scattering, however, is very weak: the return signal is a factor of 20 to 500 lower than the Rayleigh signal. Consequently, the Raman technique is mostly used for abundant constituents, such as nitrogen, oxygen and water vapor. More details on the Raman lidar can be found in *Ansmann et al.*, 1992 and *Wandinger*, 2005. Both the CRL and KARL provide information in the following channels: 355 and 532nm for elastic scattering and 387nm (N_2), 407nm (H_2O), 607 nm (N_2) for Raman scattering. KARL also has additional 1064nm elastic and 660nm (H_2O) Raman channels.

5.4.1 Lidar Optical Depth: a simple threshold approach for separating fine and coarse mode contributions

As a part of the analysis, we integrated ground-based lidar profiles to calculate lidar fine and coarse mode optical depths (we adopted the notation whereby primed optical depths, τ'_f and τ'_c, are derived from lidar profiles whereas unprimed optical depths, τ_c and τ_f, are derived from the starphotometry data). To do this we had to assume lidar ratios based on the following binary particulate classification scheme. Features with backscatter coefficient values higher than a particulate threshold were considered clouds or ice crystals and assigned to a cloud / ice crystal class while all other backscatter coefficient samples were classified as fine mode aerosols (implicit in this assignment is the assumption that aerosol optical activity is dominated by fine mode aerosols). Cloud / ice crystal samples were assigned a lidar ratio value of Sa=20sr. This value is a typical cloud lidar ratio : it is similar to the 19-25sr range used for CALIPSO data processing (*ASDC*, 2013). All non-cloud layers were assigned a value of Sa=71sr (corresponding to the CALIOP

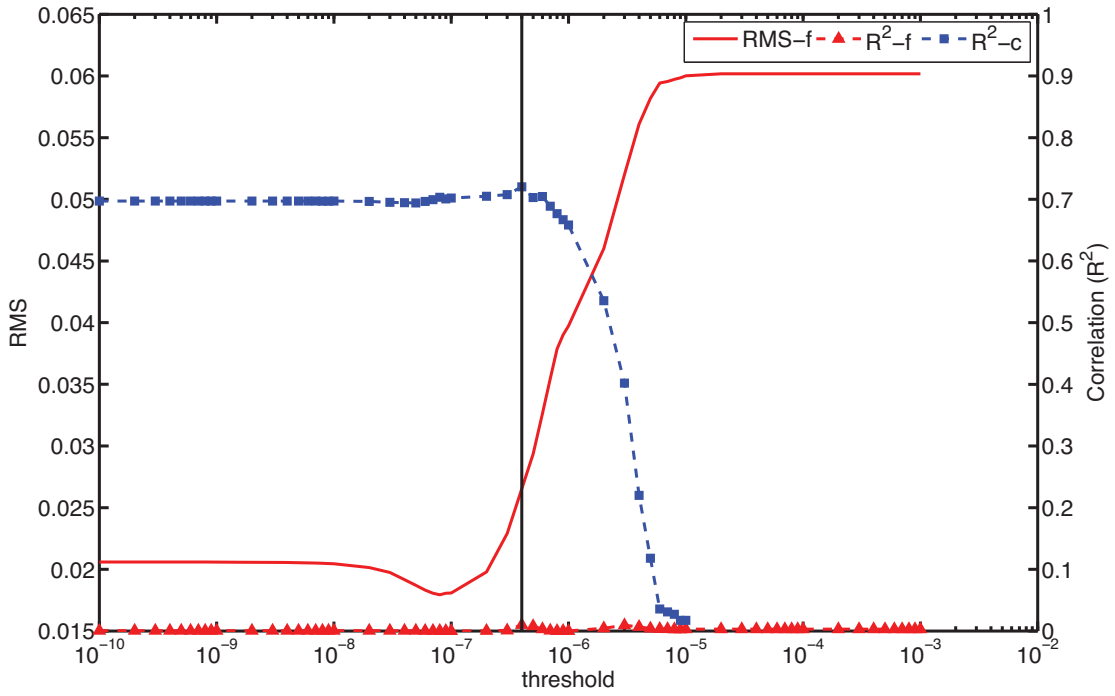

Figure 19: Backscatter threshold sensitivity study for Mar. 9, 2011 (Eureka). RMS-f coincides with RMS-c. Black vertical line represents the threshold chosen for this work: 4E-7 $m^{-1}sr^{-1}$

class "urban/industrial pollution", idem). While aerosols exhibit a natural variation in Sa, the chosen value was used for its capacity to perform well for most scenes observed at Eureka (*Perro*, 2013). In the case of Polar Stratospheric Clouds, however, we used Sa=42sr consistent with Mie calculations for large fine-mode particles (*O'Neill*, 2013)

To select a proper backscatter threshold that does not produce a significant bias in favor of either clouds or aerosols, we performed a sensibility study. Three Eureka cases were considered for which starphotometry and CRL lidar data was available: Feb. 21, 2011, Mar. 9, 2011 and Mar. 10, 2011 (the detailed discussion of these events is presented in section 6.3). We varied the threshold from 1E-9 (all/most features classified as clouds) to 1E-3 $m^{-1}sr^{-1}$ (all/most features classified as aerosols) and studied the variation of the mean RMS difference and correlation coefficient (R^2) between starphotometry and lidar optical depths. In what follows, τ'_c was calculated by direct integration (equation 35) while τ'_f was estimated from the total starphotometry optical depth: $\tau'_f = \tau_{aer} - \tau'_c$. This condition was necessary to avoid unbounded response in both τ'_f and τ'_c as a function of changing threshold. This also means that $\tau'_f - \tau_f = -(\tau'_c - \tau_c)$ and accordingly that

RMS differences will be the same for fine and coarse modes, i.e. $RMS_f = RMS_c$. As an example, Figure 19 shows the variation of RMS difference and correlation coefficient as a function of threshold for a predominantly coarse-mode event on Feb. 21, 2011.

The results are relatively insensitive to the choice of threshold in the range 1E-9 – 1E-7 $m^{-1}sr^{-1}$. As the threshold increases above 1E-7 $m^{-1}sr^{-1}$, the RMS difference grows and at 6E-6 $m^{-1}sr^{-1}$ eventually reaches a constant value when all features are classified as aerosols. The correlation coefficient for the coarse mode decreases drastically for thresholds larger than 1E-6. The fine mode correlation was insignificant whatever the threshold. Based on the RMS and R^2 values for all three cases (summarized in Table 2), the feasible threshold range (i.e. minimum RMS and maximum R^2) is between 1E-7 and 1E-6 $m^{-1}sr^{-1}$. We chose 4E-7 $m^{-1}sr^{-1}$ as the final threshold value as it produced a cloud/aerosol mask most consistent with qualitative observations (such as feature height, structure and depolarization ratio when available).

5.5 CALIOP lidar

The CALIOP lidar on board the CALIPSO satellite has been in operation since 2006 and provides vertical profiles of cloud and aerosol attenuated backscatter coefficient from the global perspective of a Polar orbit. CALIOP consists of a Nd:YAG laser operating at 532 and 1064nm. The two polarization-sensitive receivers at 532nm allow an estimation of the depolarization ratio at this wavelength. CALIOP is the only satellite operating in the visible spectrum that can provide regional aerosol information in the Arctic during the Polar Winter. Not only can CALIOP operate during night-time, its signal-to-noise ratio is distinctly better in the absence of solar background noise (*Campbell et al.*, 2012). Similar to ground-based lidars, CALIOP profiles can be vertically integrated to yield a measure of AOD. One of the notable CALIOP limitations, however, is its low sensitivity to faint aerosol layers typical for the Arctic (*O'Neill et al.*, 2008 cite the minimum detectable β of $1.1 \times 10^{-3} km^{-1}sr^{-1}$) leading to underestimated CALIOP extinction coefficients (*Di Pierro et al.*, 2013) and AODs. However, the importance of this effect during the Polar winter, in particular as it applies to AODs, has been the subject of little or no verification. The detected features in the CALIOP backscatter profiles are classified as either aerosols or clouds (*Liu et al.*, 2009) and are reported in separate products. In this work we used CALIOP Level 2 aerosol profile data (v3, *ASDC*, 2013) to study pan-Arctic aerosol dynamics in support of ground-based measurements.

Table 3: RMS difference and correlation values between starphotometry and lidar optical depths as a function of backscatter threshold

Threshold	RMS		R^2	
	fine	coarse	fine	coarse
	Feb.21, 2011			
1.0E-09	0.093	0.093	0.133	0.780
1.0E-08	0.094	0.094	0.133	0.780
1.0E-07	0.098	0.098	0.128	0.779
4.0E-07	0.104	0.104	0.127	0.779
1.0E-06	0.125	0.125	0.116	0.773
1.0E-05	0.276	0.276	0.263	0.594
1.0E-04	0.384	0.384	0.466	-
1.0E-03	0.384	0.384	0.466	-
	Mar 9, 2011			
1.0E-09	0.021	0.021	0.000	0.697
1.0E-08	0.020	0.020	0.001	0.697
1.0E-07	0.018	0.018	0.000	0.702
4.0E-07	0.027	0.027	0.010	0.720
1.0E-06	0.040	0.040	0.000	0.658
1.0E-05	0.060	0.060	0.003	0.017
1.0E-04	0.060	0.060	0.003	-
1.0E-03	0.060	0.060	0.003	-
	Mar 10, 2011			
1.0E-09	0.043	0.043	0.022	0.121
1.0E-08	0.043	0.043	0.023	0.121
1.0E-07	0.047	0.047	0.022	0.119
4.0E-07	0.056	0.056	0.025	0.123
1.0E-06	0.059	0.059	0.024	0.128
1.0E-05	0.061	0.061	0.023	0.104
1.0E-04	0.066	0.066	0.023	0.023
1.0E-03	0.067	0.067	0.020	-

Chapter 6

Results and Discussion

6.1 Pan-Arctic context

This section serves as an introduction to the analysis followed in the rest of the chapter and is meant to provide a broader Pan-Arctic context to the starphotometry and lidar measurements obtained during the Polar Winters of 2010-11 and 2011-12. *Di Pierro et al.*, 2013 discuss Arctic seasonal and inter-annual aerosol dynamics based on CALIOP data obtained between 2006 and 2012. Here we make a brief summary of their findings concerning the winter and spring-time aerosol loading. The authors confirm the presence of consistently low altitude (0-2km) aerosol layers associated with the Arctic Haze in the winter. For this altitude range, the authors also note that aerosol extinction in the High Arctic (69-82° N) is maximum in winter followed by a sharp decline in the summer (Figure 20).

This maximum in aerosol extinction was predominantly situated over Russia and (from our standpoint) is indicative of the important source role played by Russia in contributing to the Arctic Haze . The authors note that another winter surface maximum was located over the Norwegian Sea, but in this case the aerosols were thought to be of a marine origin (sea salt aerosols). Extinction enhancement was also noted over Eastern Russia in 2-5km stratum. In spring, extinction values were observed to decrease throughout the Arctic in the 0-2km range, while a maximum was noted in the middle and upper troposphere consistent with meridional transport of pollution from midlatitudes. Inter-annual 2006-2012 variability was mostly attributed to biomass burning and volcanic events in the middle and upper troposphere.

The authors also subdivide the Arctic into European (10-100° E), North American

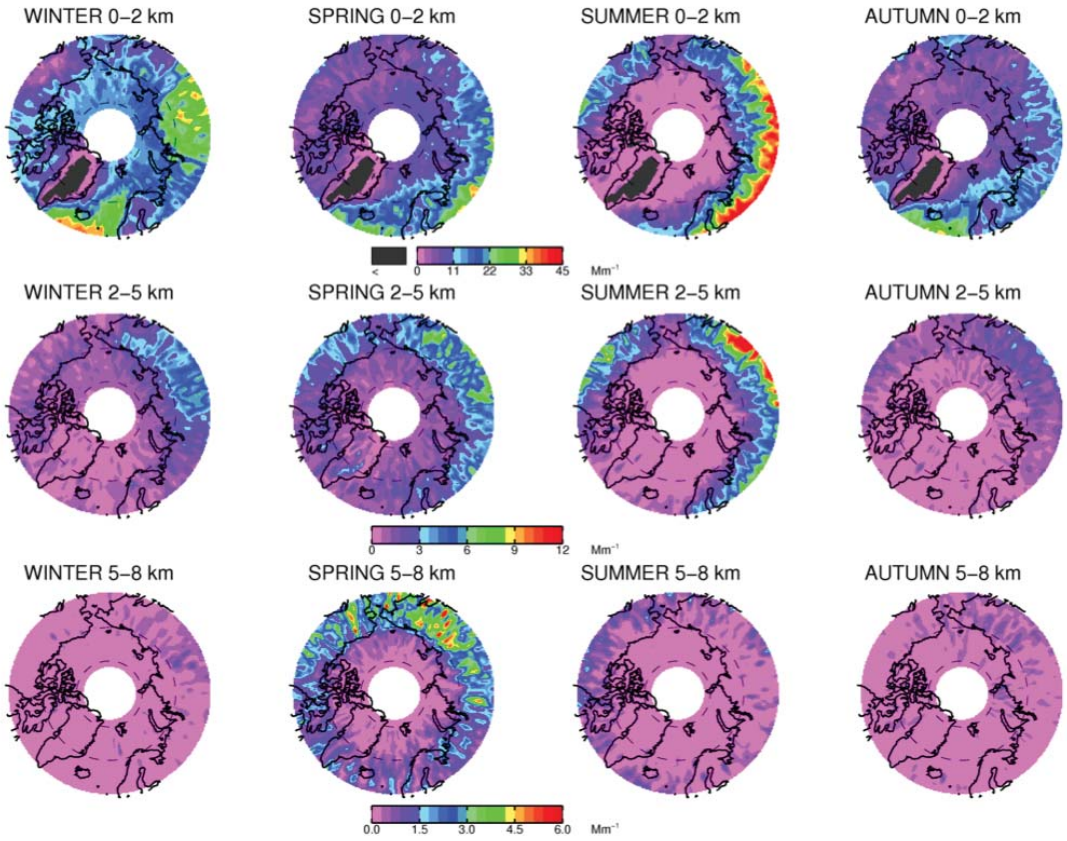

Figure 20: Reproduction of Figure 10 in *Di Pierro et al.*, 2013 with original caption: Spatial distribution of the 2006-2012 seasonal mean CALIOP nighttime-equivalent extinction. Maps are shown at 0-2 km (top panels), 2-5 km (middle panels) and 5-8 km (bottom panels) for winter (DJF), spring (MAM), summer (JJA) and autumn (SON). Note that the color scale saturation values are lowered at higher altitudes. Dashed lines mark the 70° N and 80° N latitude circles

(140-60° W), Atlantic (60° W-10° E) and Asian sectors (100° E-140° W). For the lower 0-2 km range, the European sector displays the highest wintertime extinction coefficients followed by the Asian sector. They indicate that in the free troposphere the extinction maximum over the Arctic occurs in March-April in 2-5km stratum and April in the 5-8km range.

The analysis discussed above was mostly limited to the troposphere. Furthermore, the statistics provided by *Di Pierro et al.*, 2013 were based on the mean extinction, rather than integrated values that are more relevant to the present work. To address these issues, we plotted daily-averaged CALIOP aerosol extinction profiles for the European sector (ERP, containing Ny Ålesund) and North American sector (NA, containing Eureka) in

2010-11 and 2011-12 (Figures 21-24, pane 1).

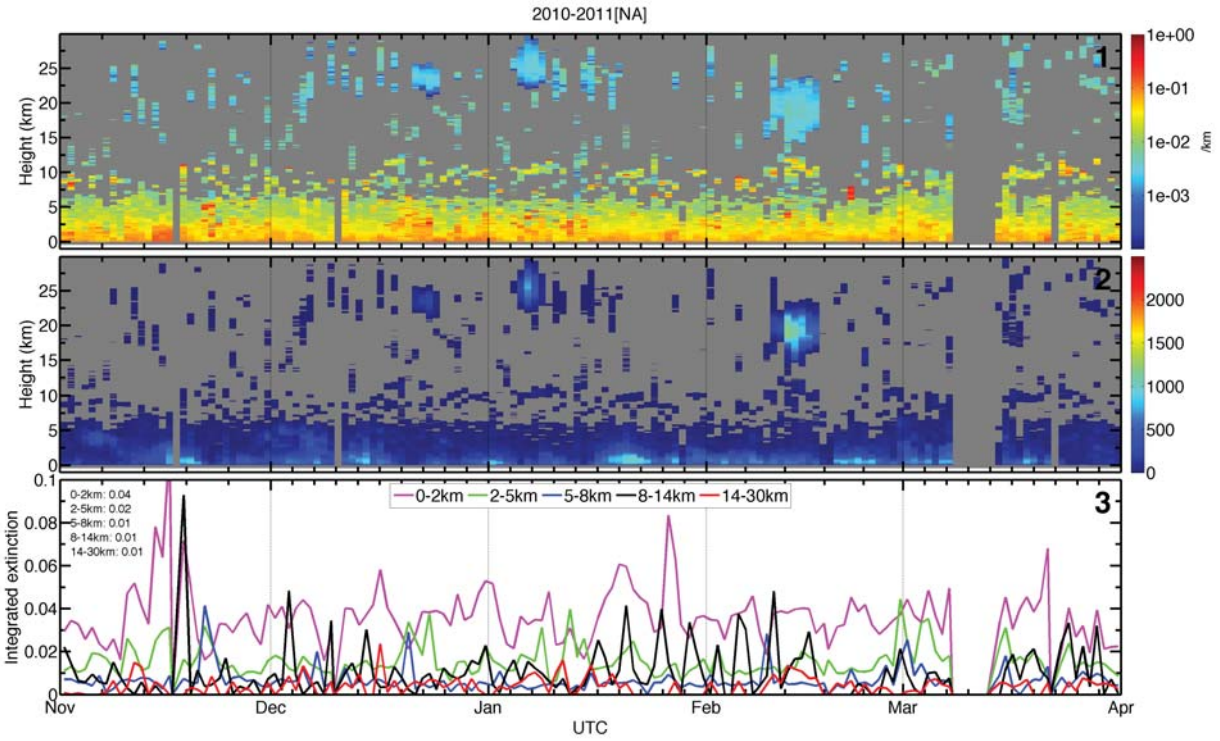

Figure 21: Pan-Arctic CALIPSO statistics for the North American sector, Nov-Apr 2010-11. Pane 1: daily averaged CALIOP extinction profiles at 532nm (km^{-1}); pane 2: number of detected aerosol occurrences at each altitude; pane 3: integrated aerosol extinction coefficient in different altitude ranges with average values given at the left.

Vertically integrated extinction gives an estimation of CALIOP AOD. Similarly to *Di Pierro et al.*, 2013 we removed all aerosol layers with unrealistically high extinction values ($>0.5km^{-1}$). In addition, we excluded ice crystals events by removing extinction values greater than $0.35km^{-1}$ in the lowest 2km (*Di Pierro et al.*, 2013 referred to these events as "diamond dust" : we prefer the more generic "ice crystal" label, especially in the light of the diamond dust versus ice crystal discussion of Section 3.5.1). This filtering assured against unrealistic and isolated AOD peaks that would have been encountered otherwise. The significance of the averages that are shown should probably be weighted differently depending on the number of profiles employed to calculate them (pane 2). In other words, average AODs computed from a higher number of profiles have more statistical significance than those associated with only a few profiles.

Despite following as close as possible their data processing scheme, we found that our

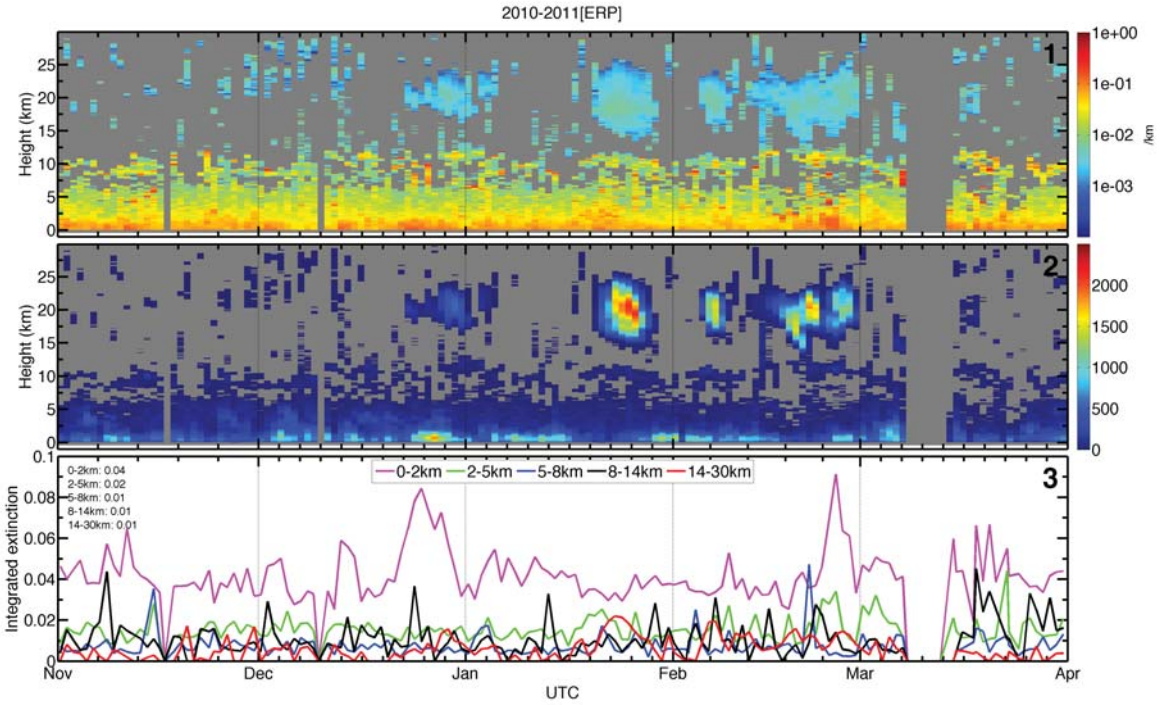

Figure 22: As in Figure 21 but for the European sector.

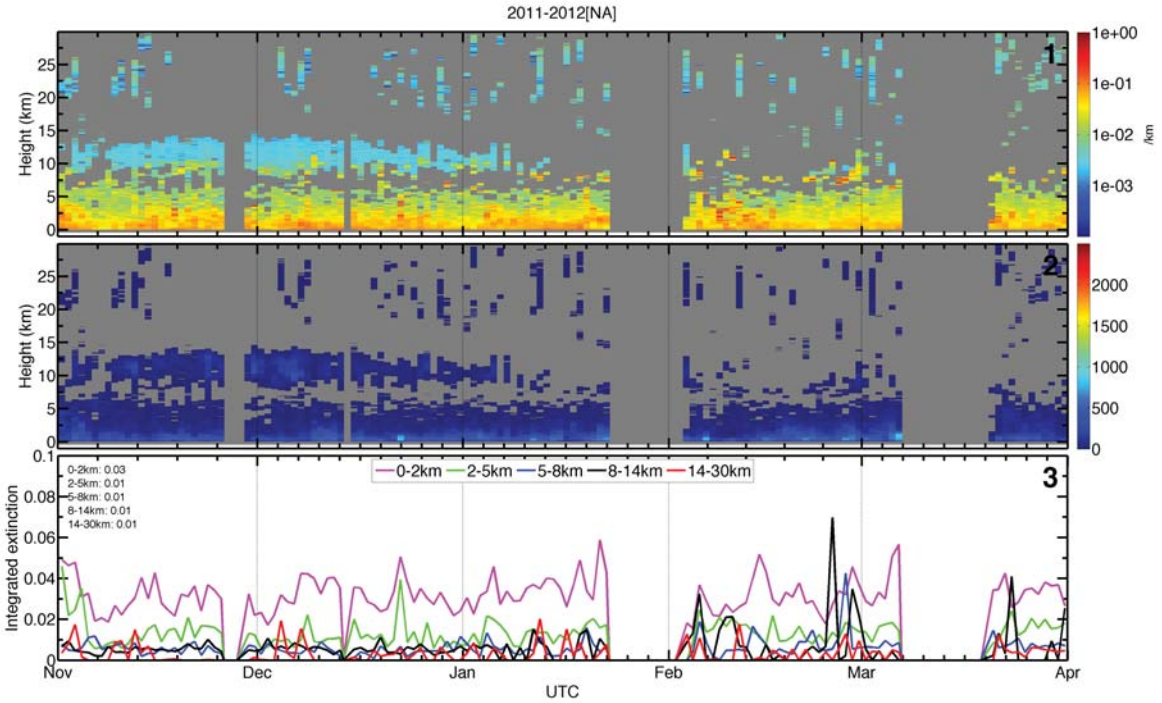

Figure 23: As in Figure 21 but for Nov 2011-Apr 2012.

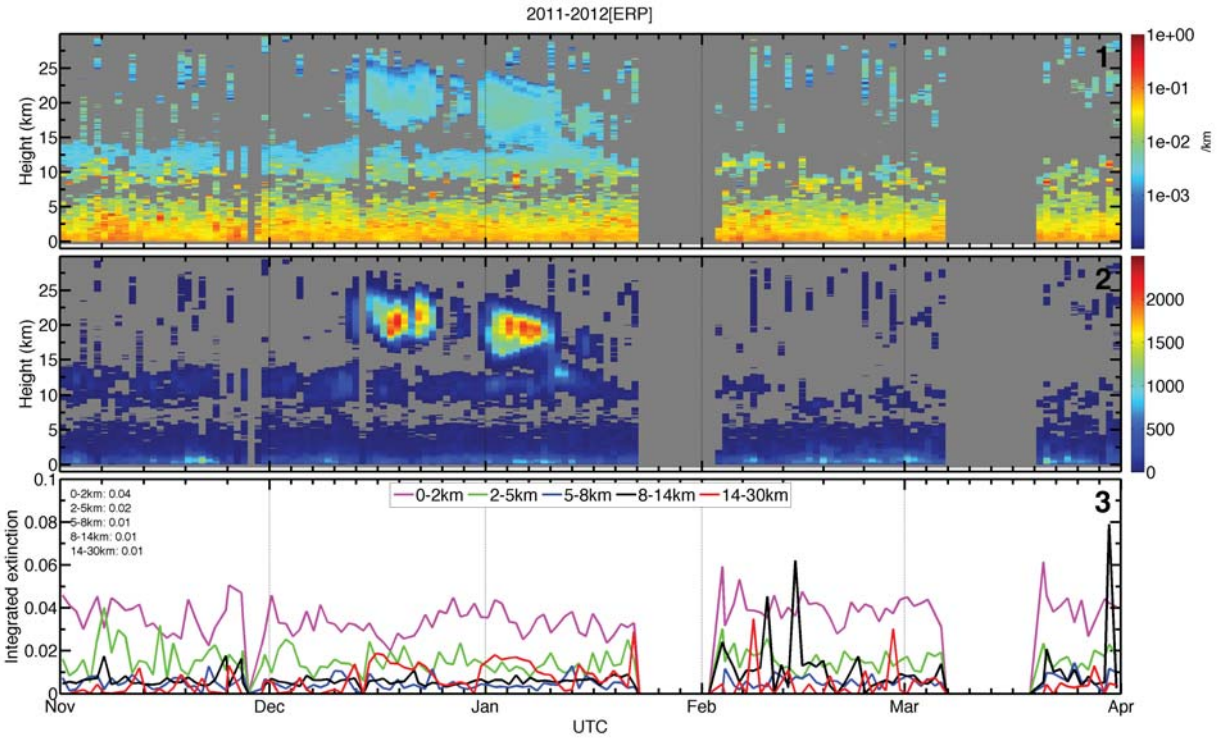

Figure 24: As in Figure 22 but for Nov 2011-Apr 2012.

seasonal values were higher than the 2006-2012 averages reported in *Di Pierro et al.*, 2013 (see Figure 42): the 0-8km averages for 2010-11 were 0.07 vs 0.03 and 0.07 vs 0.05 for the NA and ERP cases, respectively. In 2011-12 the values were 0.05 vs 0.03 and 0.07 vs 0.05 for the NA and ERP cases. The difference can be significant but in reviewing individual CALIOP profiles, it became clear to us that there were unrealistically large (nominally aerosol) backscatter contributions that could be eliminated or retained depending on the threshold employed. This sensitivity problem requires more analysis.

We have chosen the tropospheric stratification scheme as in *Di Pierro et al.*, 2013 (0-2km, 2-5km and 5-8km) adding two additional layers in the stratosphere: 8-14km and 14-30km corresponding to aerosols transported from mid-latitudes (and volcanic aerosols) and polar stratospheric clouds, respectively.

Of particular interest is a pronounced feature in the 2011-12 data (Nov 2011-Jan 2012) between approximately 9-14km. It is noticeable across the Arctic (i.e. including vertical profiles of the Atlantic and Asian sectors that are not shown below) and is probably due to a volcanic eruption. Preliminary investigation shows that the layer

might be associated with the eruption of the Icelandic Grímsvötn volcano in May 2011. In particular, *Dolgii et al.*, 2012 used ground-based lidar data to report the presence of a stable lower-stratospheric layer that was attributed to Grímsvötn and observed until the end of 2011. The AOD of the approximately 4 km thick plumes seen in Figures 23 and 24 ≈0.01 (assuming a typical sulphate lidar ratio of about 60 sr as suggested by *O'Neill et al.*, 2012).

During the two Polar Winters several PSC events are clearly identifiable between December and February for both sectors (with the notable exception of the North American sector in 2011-12). For the period of Jan 1-7, 2012 CALIOP indicates AODs of up to 0.06 associated with typical PSC heights in the European sector (14-25km). In section 6.3.5 we discuss a PSC event that was detected at Ny Alesund on Jan 5-6, 2012.

6.2 Measurement frequency overview

During the Polar Winters of 2010-11 and 2011-12 the starphotometers and lidars were run whenever possible with the exception of periods subject to unfavourable weather conditions or operational difficulties. Figure 25 gives the frequency of measurements, while Figures 38-41 show starphotometry daily averages and lidar profiles for when the instruments were operational.

6.3 Individual events

We have argued above that the process-level analysis of starphotometry and lidar data is an essential step to yield confidence in characterization of night-time atmospheric phenomena. This task is especially challenging and even more relevant for the Arctic, given the optically weak nature of many aerosol and cloud layers. Furthermore, each instrument is associated with a number of conceptual or operational particularities, that might translate into data artifacts or inconsistencies and that need to be detected and understood. In this section we present a detailed analysis of the following events: aerosols (Eureka: Mar 9-10, 2011, Mar 13-15, 2012), ice crystals (Eureka: Mar 10, 2011), thin clouds (Eureka: Feb 21, 2011), polar stratospheric clouds (Ny Ålesund: Jan 5-6, 2012, Dec.14, 2011).

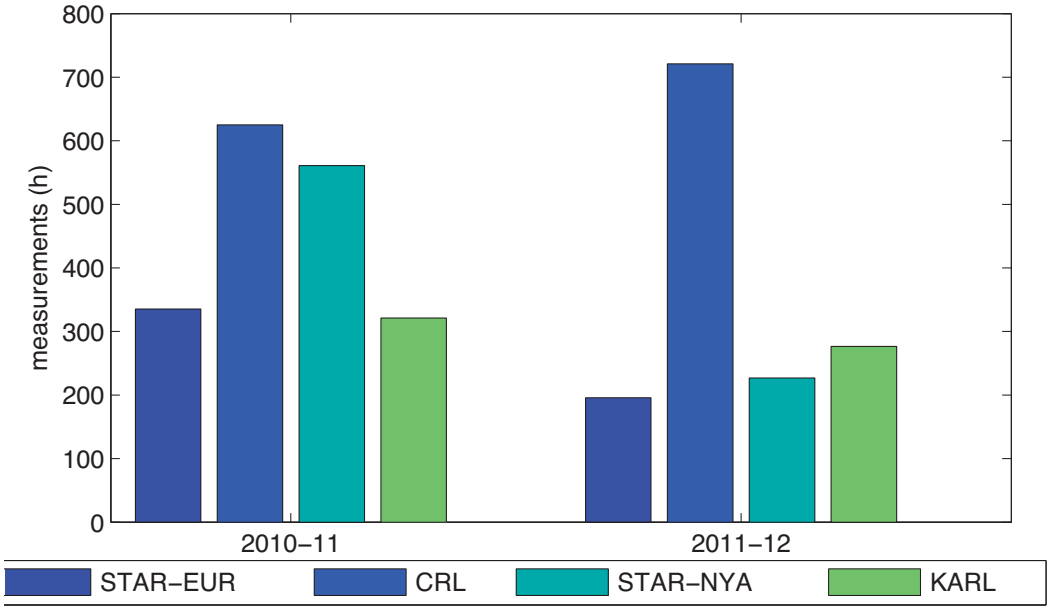

Figure 25: Frequency of starphotometer and lidar measurements at Eureka and Ny Ålesund. One lidar measurement corresponds to a profile of backscatter measurements with a temporal resolution of 10min at Eureka and 1.3 and 15min at Ny Ålesund for 2010-11 and 2011-12 respectively

6.3.1 Aerosol event (EUR: Mar 9-10, 2011)

Figure 26 shows starphotometry and lidar data obtained at Eureka between 00:00 on Mar 9 and 13:00 on March 10, 2011.

The top pane contains fine and coarse mode AODs from the SDA at 500nm (τ_f and τ_c respectively), while pane 2 shows CRL backscatter cross-section profiles at 532nm. Atmospheric complexity of the given time period is manifested in by the presence of what we interpret to be several distinct features: aerosol layers up to 6km, tropospheric clouds between 6 and 10km as well as PSC layers above 14km. In addition, Mar 10 is associated with surface layer ice-crystals in the lowest 500m, discussed in more detail below.

In general, the SDA shows an average τ_f of 0.06, generally dominated by the low-amplitude backscatter aerosol layers between 1 and 6km. Aerosol plumes were especially prominent on Mar. 9 gradually thinning out towards the end of the 2-day period.

Lidar fine and coarse mode AODs were calculated in accordance with section 5.4.1. In pane 1, we plotted τ'_f and τ'_c corresponding to the lidar ratio assignments derived for the aerosol/cloud classification of pane 3. We see that, in general, τ'_f agrees moderately well

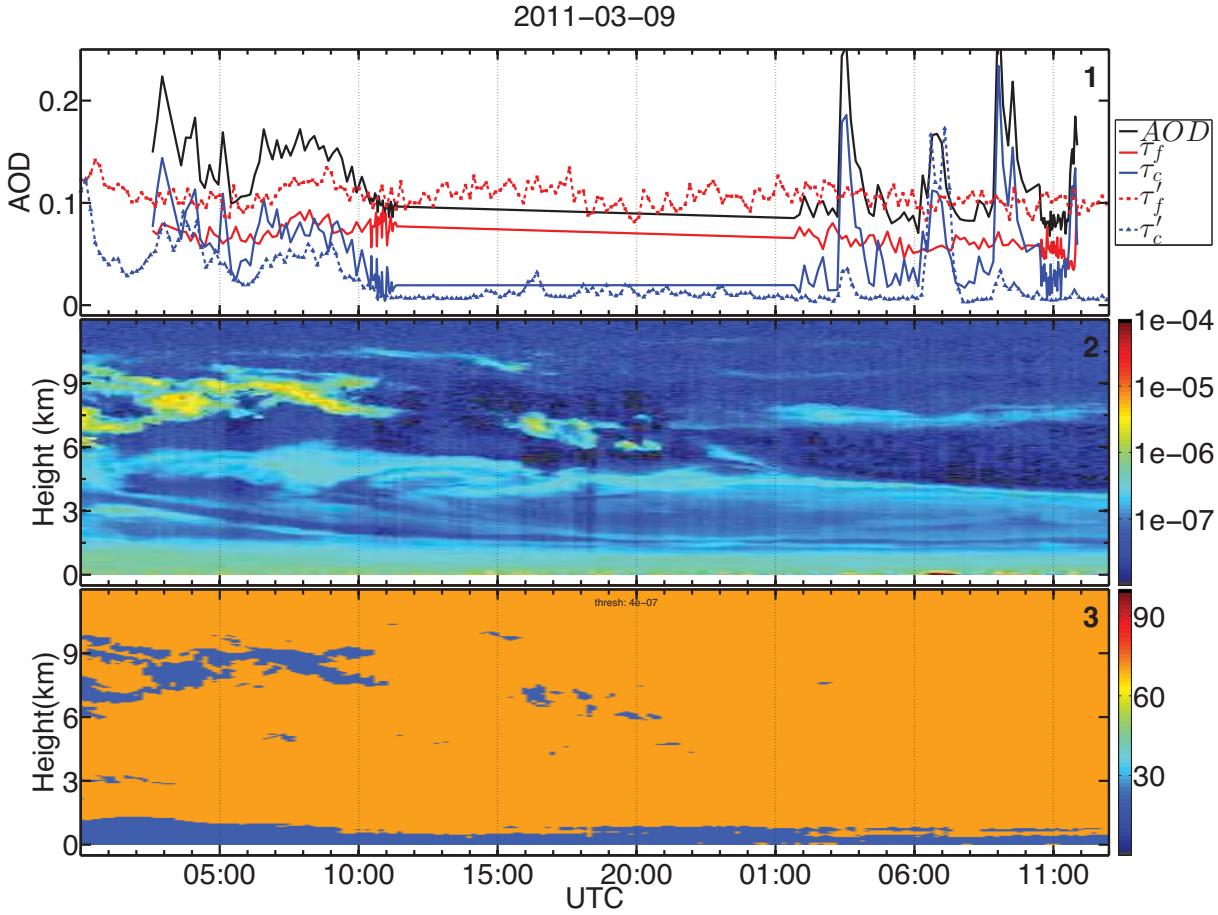

Figure 26: Eureka aerosol event Mar 9-10, 2011. Pane 1: starphotometry and lidar fine and coarse mode AODs; pane 2: CRL 532nm backscatter cross-section ($m^{-1}sr^{-1}$); pane 3: lidar ratio values.

with the starphotometry τ_f (RMS difference of 0.03) with τ_f being generally less than τ'_f. The degree of correlation between τ_f and τ'_f is marginal at best, since there are no strong temporal variations in these two parameters (aside from high frequency variations such as those that are especially evident in τ_f on March 10 at 11:00). However, as an illustration, we would argue that they both react (with a precision $<\approx 0.01$) to the most optically active portion of the (presumed) fine mode layer around 8 km altitude on Mar. 10 (between the dashed purple lines of Figure 27). Returning to Figure 26, we note that the PSCs at around 14km are characterized by an estimated τ_f value $<\approx 0.01$. τ'_c in turn corresponds moderately well with starphotometry τ_c, especially for the cloud feature in the first half of Mar 9 (RMS difference between τ'_c and τ_c is 0.04 for the whole period,

and 0.03 for Mar 9). Of particular interest are the three coarse mode peaks on Mar 10 that are evident in both starphotometry and lidar data. The signal enhancements are due to surface layer ice-crystals and are discussed in more detail in section 6.3.3.

All of these indicators would tend to confirm our original hypothesis that τ'_f and τ'_c can be approximately derived from the classifications of pane 3 and that the estimates are approximately coherent with the analogous estimates from the starphotometry. The lidar errors inherent in such a comparison include the original classification, the assigned lidar ratio values (probably no better than ≈10 sr or hence ≈ 10% error in predicted τ'_f or τ'_c values), and artifacts such as observed in Figure 27 (≈0.01 in that figure). The starphotometer errors include the estimated AOD calibration errors (≈0.02) and SDA errors (≈10%). The latter errors include the high frequency variation observable in the τ_f curves of Figure 27 : these are caused by subtle but real changes in spectral curvature (which in turn could be attributed to noise-like variations in the signal of any of the spectral channels).

No CALIOP data was available during the time frame of the event. In general, the presence of spatially contextual confirmation data from CALIOP can be of significant help in understanding the dynamics of a particular aerosol evens over ground-based lidar sites. It should be stated, however, that in this case the CALIOP lidar would have been near its lower limit of detectability given the observed weak optical depths (see *O'Neill et al.*, 2008 for a brief discussion of this lower limit).

6.3.2 Aerosol event (EUR: Mar 13-15, 2012)

Figure 28 shows another potential aerosol event detected on Mar 13-15, 2012 at Eureka.

We presume that the features visible in the CRL profiles starting at 10:00 on Mar 13 in the 2-4.5km altitude range are aerosol layers mixed with cloud. Given the limited sampling range of the starphotometry, however, it is hard to confirm this hypothesis without some additional information, such as lidar depolarization ratio. It is, also, of interest to remark the increase in coarse-mode starphotometry AOD between 02:00 and 07:00 on Mar 14. The high frequency components of this increase (the spikes of τ_c) are supported , to a degree, by the very low-altitude crystal layers that one sees in the backscatter coefficient profile below a few hundred meters and by τ'_c but with lower amplitude peaks (we refer the reader to the description associated with Figure 29 for a more detailed discussion of this type of phenomenon). The low frequency increase

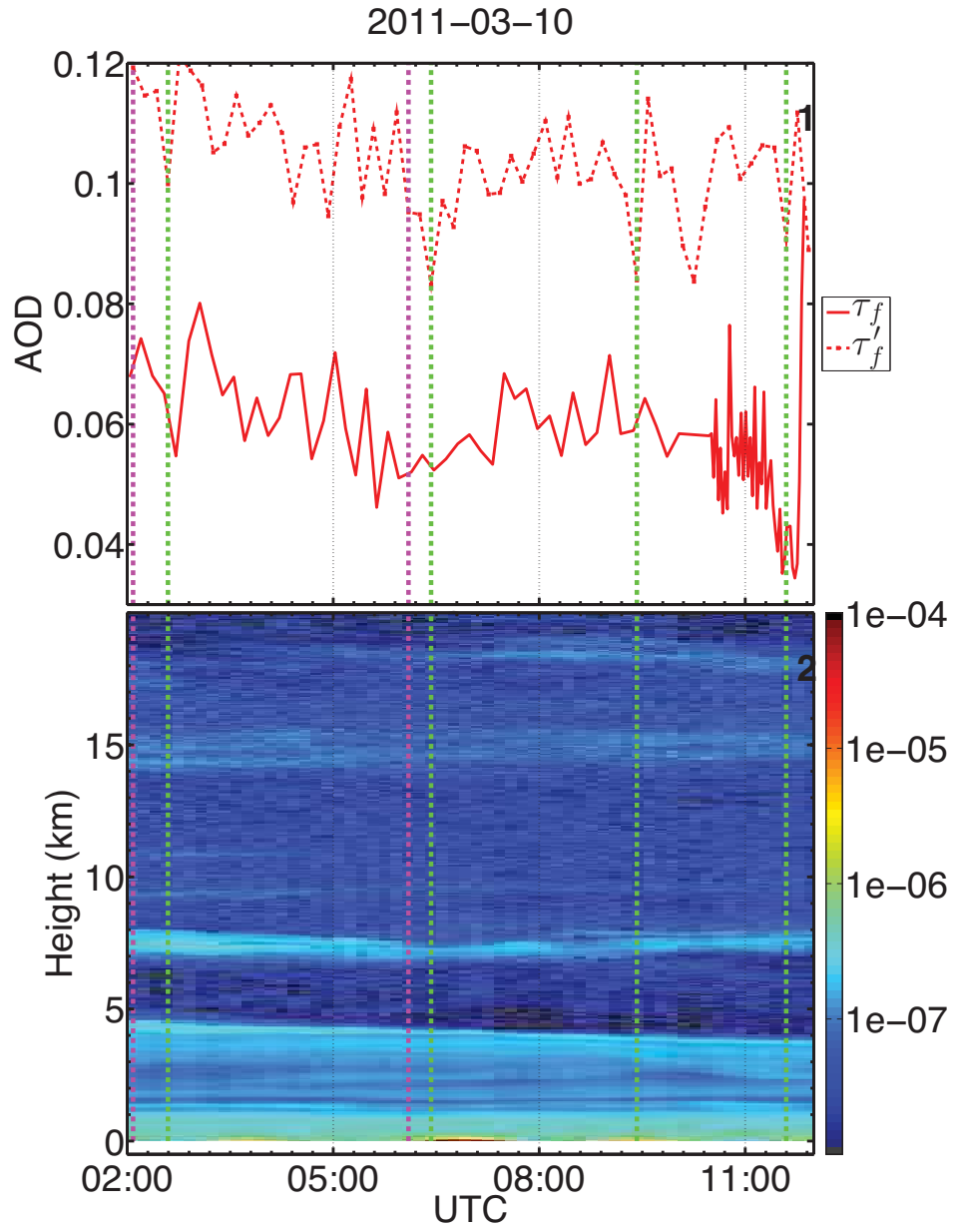

Figure 27: Zoom of the backscatter profile and the fine mode optical depths (τ'_f and τ_f) as a function of time on March 10, 2011. The purple dashed vertical lines show the approximate limits of where the plume at around 8 km altitude is at its most optically active. The dashed green lines indicate vertical striping artifacts in the backscatter coefficient profile which are likely due to error in the top-end initialization owing to the statistics of photon counting. This error will propagate downward (*Duck*, 2013).

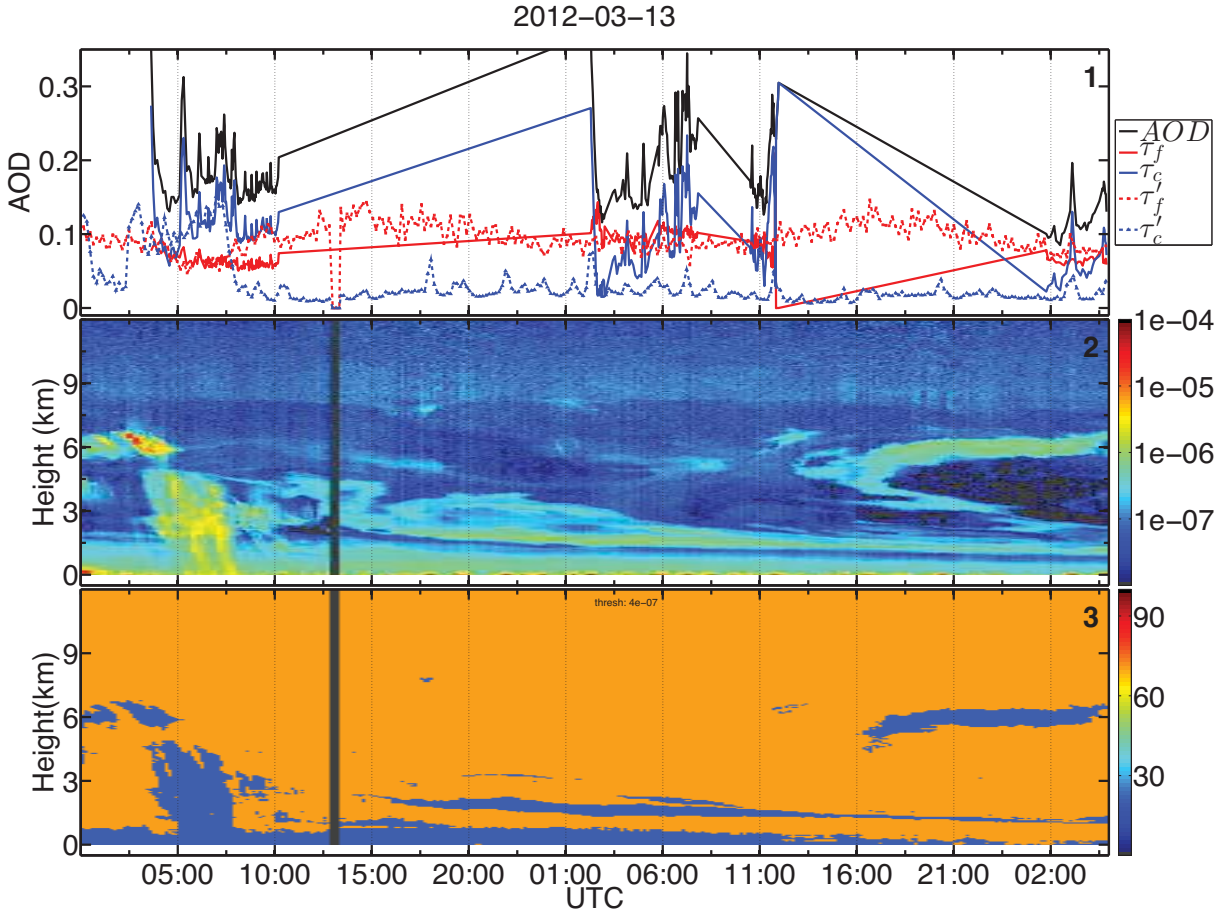

Figure 28: Same as Figure 21 but for Mar 13-15, 2012.

in τ_c, where these crystal layers appear to be missing, is however not supported by a low frequency increase in τ_c' (it stays relatively stable during the 5-hour time frame aside from the high frequency peaks). A possible explanation would be gradual ice crystals deposition on the telescope similar to that shown in Figure 18. Meteorological observations from the weather station at Eureka indicate indeed the presence of ice crystals. A better indication of the false OSM increase, however, would be a relatively stable TSM AOD. Unfortunately, the majority of data during the questionable AOD increase was obtained using the OSM mode and hence, no decisive conclusion can be made. While τ_f seems to indicate the presence of a moderately large fine mode event from 02:00 to 07:00 this event was chosen more to demonstrate how the star photometry support for the presence of a potential fine mode event seen in the lidar data can be fraught with difficulties if the starphotometer optical depth is acquired over a short time

period (during which there is no substantial change in fine mode optical depth) and if that observation period is contaminated with real or artifactual coarse mode events. No CALIOP data was available for the duration of the event.

6.3.3 Ice crystals (EUR: Mar 10, 2011)

The proper detection of the coarse mode optical depth, whether it represent coarse mode aerosols or cloud is an important test of the spectral curvature fidelity of the starphotometer optical depths, the performance of the SDA and the performance of any cloud screening algorithm. Figure 29 shows an extract of Figure 26 for March 10, 2011 with the lidar data in panes 2 and 3 displayed only for the lowest 2km.

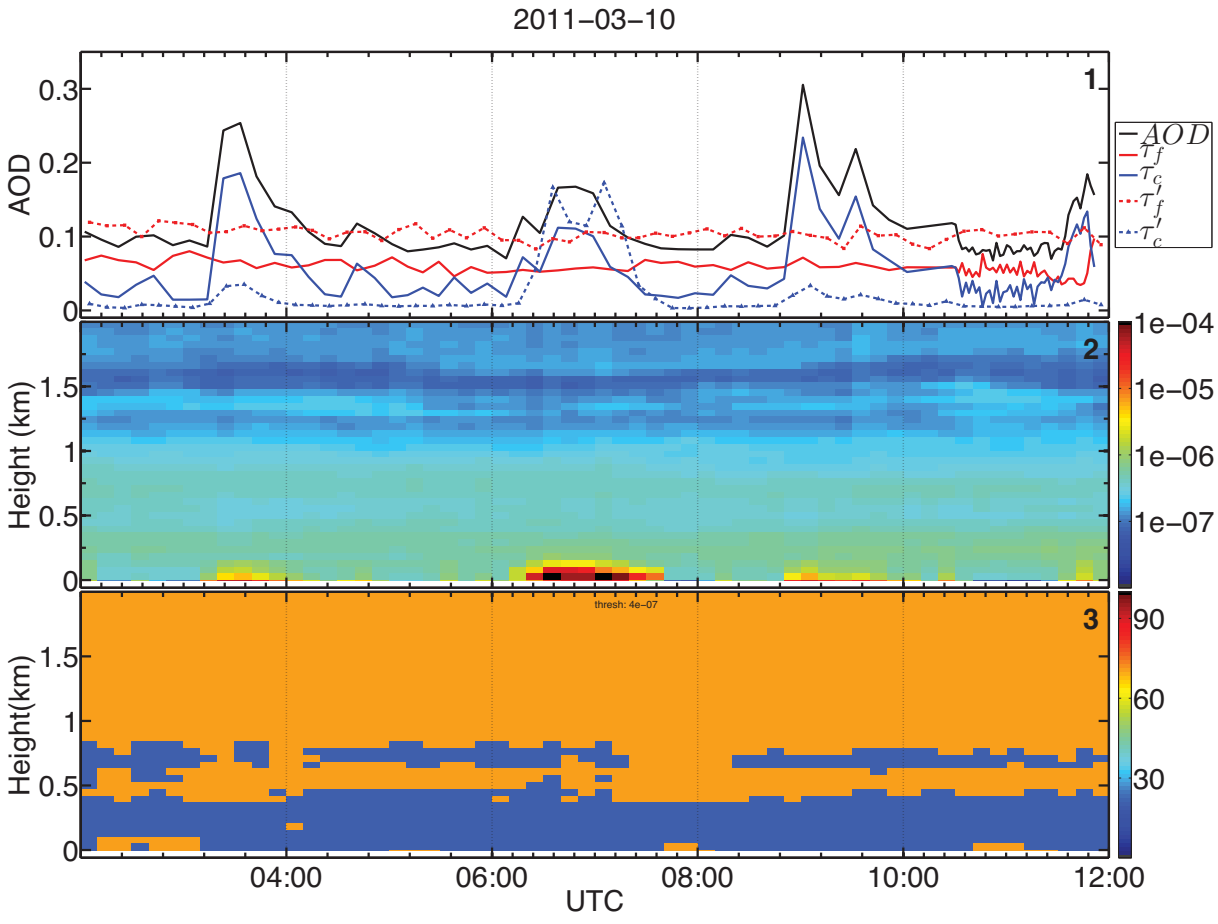

Figure 29: An extract from Figure 26 for Mar 10, 2011. The CRL profiles are shown for the lowest 2km.

The peaks in starphotometry AODs at 3:25, 6:35 and 9:00 are correlated in time with the enhanced lidar signal in the lowest 250m. Furthermore, the SDA indicates that the observed features are coarse-mode dominant. While some weak backscatter layers are present at the higher altitudes (the stratospheric features of pane 2 in Figure 26), τ_c' is dominated by the low-altitude features. For the vertical profile at 7:00, the first 250m contribute more than 80% to the total integrated value. The peaks in τ_c' correspond well in time to those of τ_c. The τ_c' values at 3:25 and 9:00, however, are significantly lower than the corresponding τ_c values. At these low altitudes the laser beam is not entirely within the field of view of the detection optics, so it is likely that the inconsistencies between τ_c' and τ_c are due to the incomplete overlap correction (*Perro*, 2013). In this case, starphotometry measurements are particularly relevant given inherent lidar difficulties at the lowest altitudes.

6.3.4 Thin clouds (EUR: Feb. 21, 2011)

Generally, clouds are relatively opaque and strongly attenuate the inherently weak star radiation. Some types of clouds (such as thin ice clouds, TICs), however, can be optically thin, while extending vertically for several kilometers. An example of such a cloud event observed on Feb. 21, 2011 at Eureka is shown in Figure 30.

The optical depth values of pane 1 show a significant variation between 0.2 and 0.8 during the 11.5-hour measurement period. The SDA applied to the starphotometry dataset shows the dominance of the coarse mode particles which compose the cloud. The assumption that the coarse mode optical depth variation can be ascribed to clouds is supported by the CRL data showing strong backscatter coefficient features in the 3-5 km altitude range. Perhaps more convincingly, the presence of clouds is confirmed by the high depolarization ratio values[1] (up to 40-50%, pane 4) which are spatially correlated with the high backscatter coefficient values of pane 2. Such high depolarization ratio values are typical of ice crystal clouds. The CRL integrated signal associated with cloud features, τ_c', shows good correlation ($R^2 = 0.78$) with the starphotometry coarse mode, τ_c. τ_c' is nevertheless, somewhat smaller than τ_c beyond 05:00. The difference can be due to the prescribed generic lidar ratio of 20sr for the clouds. A slightly higher value of S_a=25sr might be more appropriate as it would bring the τ_c' in better agreement with τ_c (we would also note that the overlap function at the relatively high-altitude positions of

[1]depolarization ratio data for 2011 was generally noisy due to technical difficulties, in this case, however, a strong signal stood out above the noise.

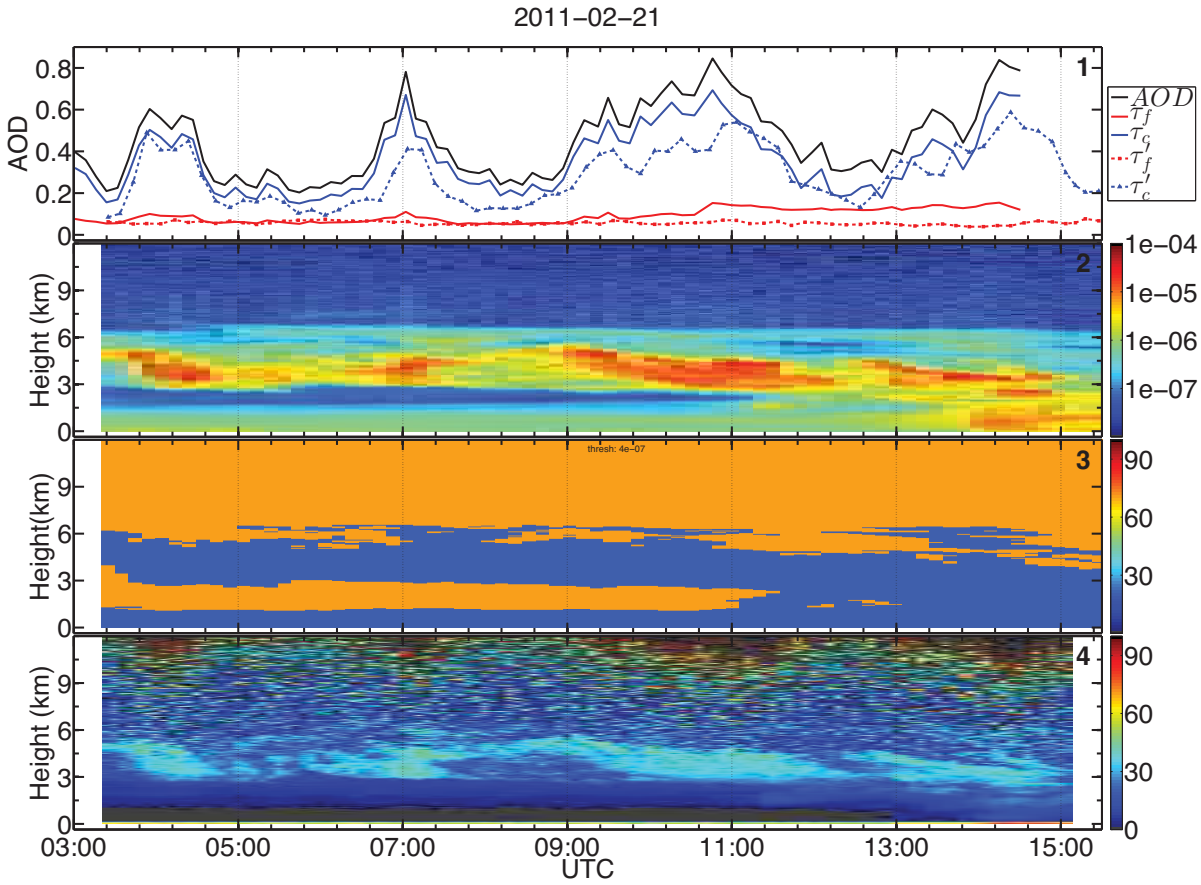

Figure 30: Top 3 panes as in Figure 26. Pane 4 is CRL linear depolarization ratio (%). The data was not overlap corrected in the bottom most 1km. Eureka, Feb. 21, 2011.

the clouds is not an issue). The reader will also note that the fine mode optical depth is relatively stable with realistic values in spite of being dominated by the coarse mode contributions. The τ_f values are around 0.07 until 9:00 and agree closely with those of τ'_f. Beyond 9:00 τ_f rises to the mean value of 0.12, but τ'_f does not undergo a similar change. This discrepancy might be associated with the SDA uncertainties, given the predominantly coarse-mode scene.

6.3.5 Polar Stratospheric Cloud event (NYA: Jan 5-6, 2012)

Background stratospheric optical depth (SOD) values are usually very small (<0.02 : eg. *Sato et al.*, 1993). During the period of Jan 1-7, 2012, however, CALIOP profiles showed enhanced SODs exceeding 0.06 and associated with polar stratospheric clouds (PSC) in

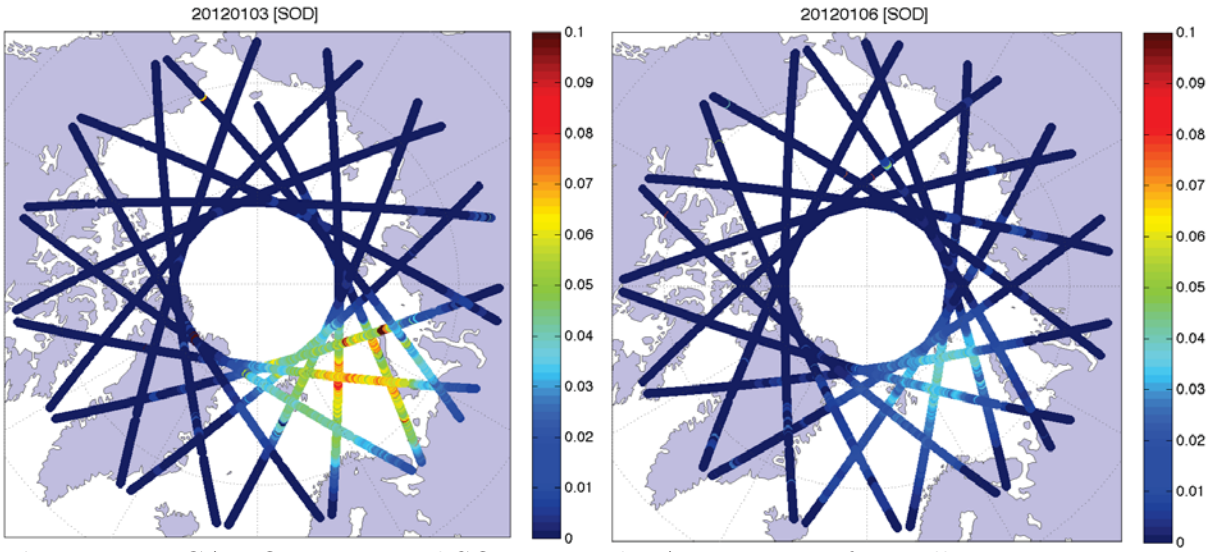

Figure 31: CALIOP estimated SODs over the Arctic region from all overpasses on Jan 3 (left) and 6 (right), 2012. Jan 3 is associated with one of the strongest SOD signals between Jan 1 and 7, 2012.

the European-Russian part of the Arctic (Figure 31).

A particular case of such a large PSC between approximately 15 to 23 km was detected on Jan 5-6, 2012, during an overpass of Ny Ålesund at around 03:53 UTC (Figure 32). The CALIOP depolarization channel indicates that the PSC is a low (if noisy) depolarization feature. Such features have been classified as Type Ib STS (supercooled ternary solution) PSCs consisting of moderate sized liquid spherical particles or a mixture of Type 1b and Type 1a (non-spherical or crystal) particles (*Pitts et al.*, 2011 based on multi-year CALIOP data over the Arctic and Antarctic). Both types of particles grow from initial fine-mode sulfate distributions (see for example, *Toon and Turco*, 1991) but, according to *Strawa*, 2002, bifurcate with increasing extinction coefficient into Type Ia particles with modal radii $\approx$ a few μm or Type Ib particles with modal radii $\approx$ a few tenths of a μm . *Pueschel et al.*, 1992 reported Type I, sub-micron ($r_{eff} \approx 0.5\mu m$) spherical particles computed from particle size distribution measurements acquired aboard an ER-2 aircraft that was flown through a PSC located near Ny Ålesund (effectively Type Ib, STS particles). They pointed out that such particles produced a 10-fold increase in optical depth over ambient sub-micron particles in the Arctic stratosphere (i.e. much more likely to be observed by CALIOP and starphotometry).

The combined starphotometry-KARL data acquired on Jan 5 and 6, indicates that the observed layers are fine-mode dominant ($<1\mu m$) (Figure 33). In fact, the effective

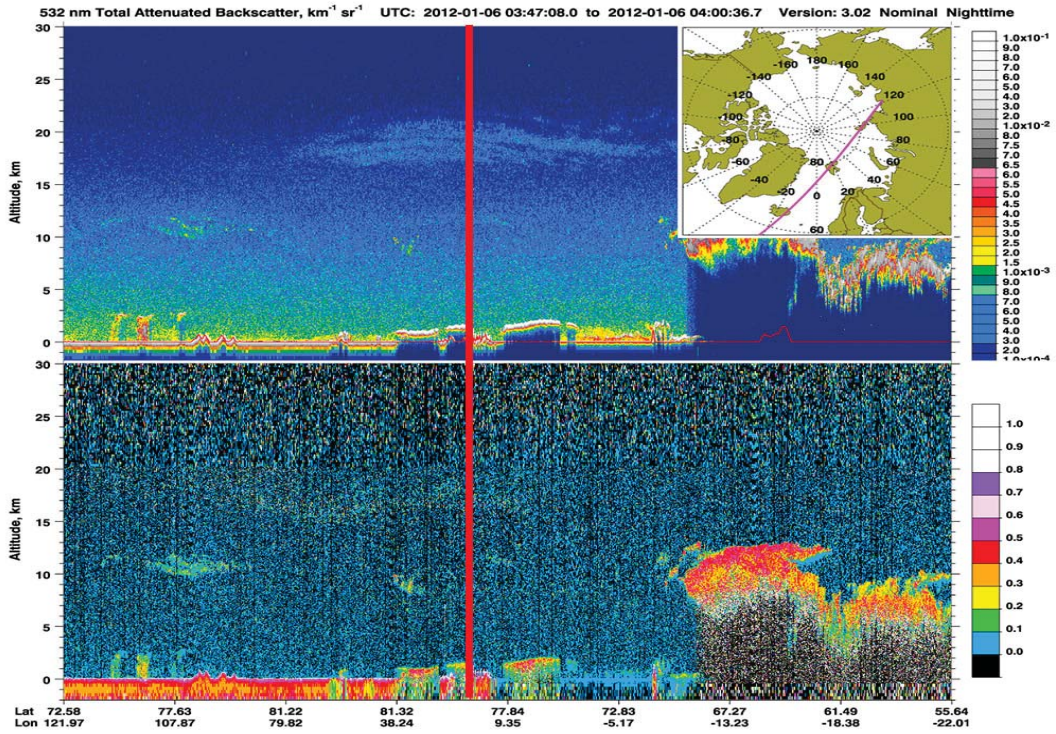

Figure 32: CALIPSO 2D profile acquired on Jan 6, 2012 at approximately 03:53 over Ny Ålesund. Top: attenuated backscatter coefficient at 532nm ($km^{-1}sr^{-1}$). Bottom: depolarization ratio (unitless). The red vertical line approximately indicates the Ny Ålesund location. The purple line on the map indicates the CALIOP orbit.

radius ($r_{eff,f}$) estimated from starphotometry data using SDA/FMC[2] retrieval is between 0.25 and 0.45μm (pane 3) : this means that the observed PSC consists of large fine-mode particles. Stratified lidar optical depth integrations showed that an average PSC optical depth of 0.09 was about 60% of the total optical depth (indicating that the fine mode retrieval of effective radius will be sensitive to the presence of smaller non-Type I fine-mode aerosols). In addition the SDA / FMC retrieval has never been tested, let alone validated, for such large fine mode particles while the small fine mode optical depths characterizing this event increase the retrieval error (as can be inferred from the high frequency variation of the fine mode A.E. and $r_{eff,f}$ between the times of 17:00 and 21:00 UT in pane 4 of Figure 33). Hence, the fine-mode nature of PSCs has to be further investigated using other examples before final conclusions can be drawn. In spite of these shortcomings we feel reasonably certain that the starphotometer measurements have captured a fine mode Type I PSC event : we are not aware that this has ever been

[2]Fine Mode Curvature

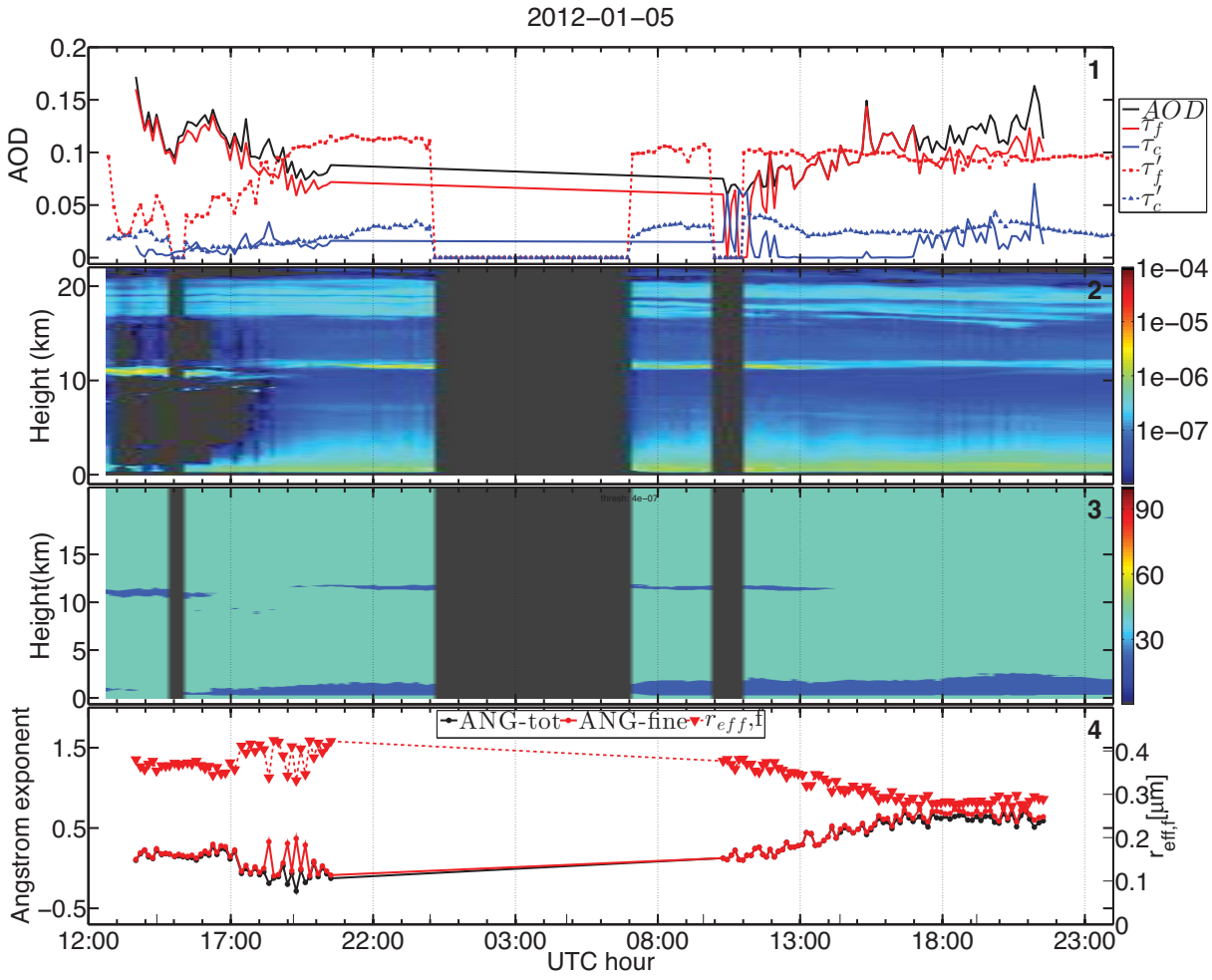

Figure 33: Data for Ny Ålesund, Jan. 5-6, 2012. Pane 1: starphotometry and lidar fine and coarse mode AODs; pane 2: KARL backscatter coefficient ($m^{-1}sr^{-1}$); pane 3: lidar ratio values; pane4: total and fine-mode Angstrom exponents and fine-mode effective radius from SDA/FMC retrievals

reported in the literature.

6.3.6 Polar Stratospheric Cloud event (NYA: Dec 14, 2011)

To reinforce the claim of starphotometry and lidar correlation in the presence of stratospheric features we studied an additional PSC case which occurred on Dec.14, 2011 over Ny Ålesund (Figure 34). Lidar data is missing from 9:24 to 15:33 due to technical problems. One can remark, however, that the few available KARL profiles between 9:10 and

9:24 show PSC features above 18km that are somewhat thinner than the PSC layer observable after 15:33 (pane 2). This corresponds to a slight, but nevertheless appreciable increase in mean τ'_f values from 0.09 to 0.10. Starphotometry high star data seem to confirm this increase with mean τ_f values of 0.08 and 0.10 before and after 15:33, respectively (the RMS difference with τ'_f after 15:33 is 0.02). The low star τ_f values show a more gradual but larger increase from 0.07 at 9:10 to 0.11 at 18:31.

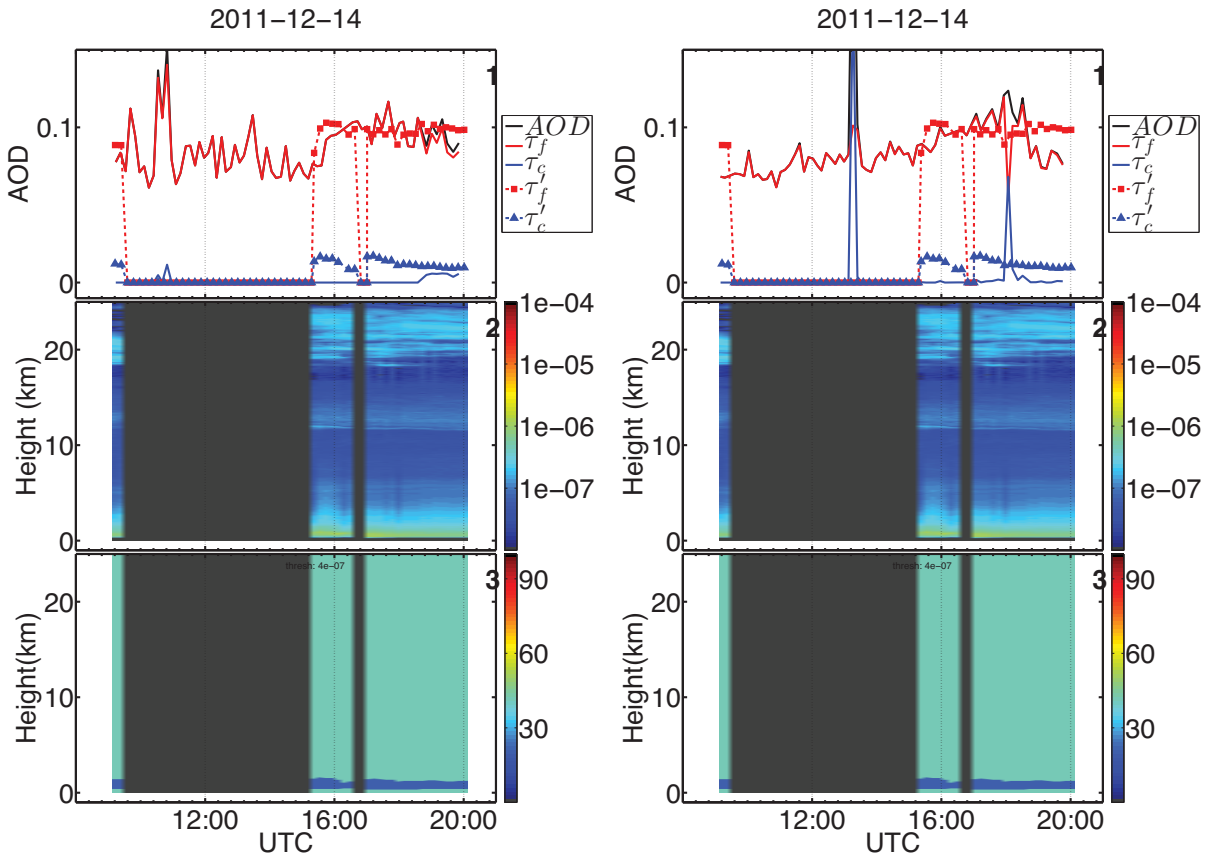

Figure 34: Starphotometry and lidar correlation for a PSC event on Dec.14, 2011 over Ny Ålesund. Panes 1-3 as in Figure 33. Left: high star, right: low star.

6.4 Cloud screening

We examined the performance of temporal cloud screening on several examples. Figure 35 shows the results of filters applied to the AOD time series on the Mar 10, low-altitude crystal event of Figure 29 (filter 1, the optical depth upper limit condition, is ineffective in this case as all AODs are smaller than 0.35).

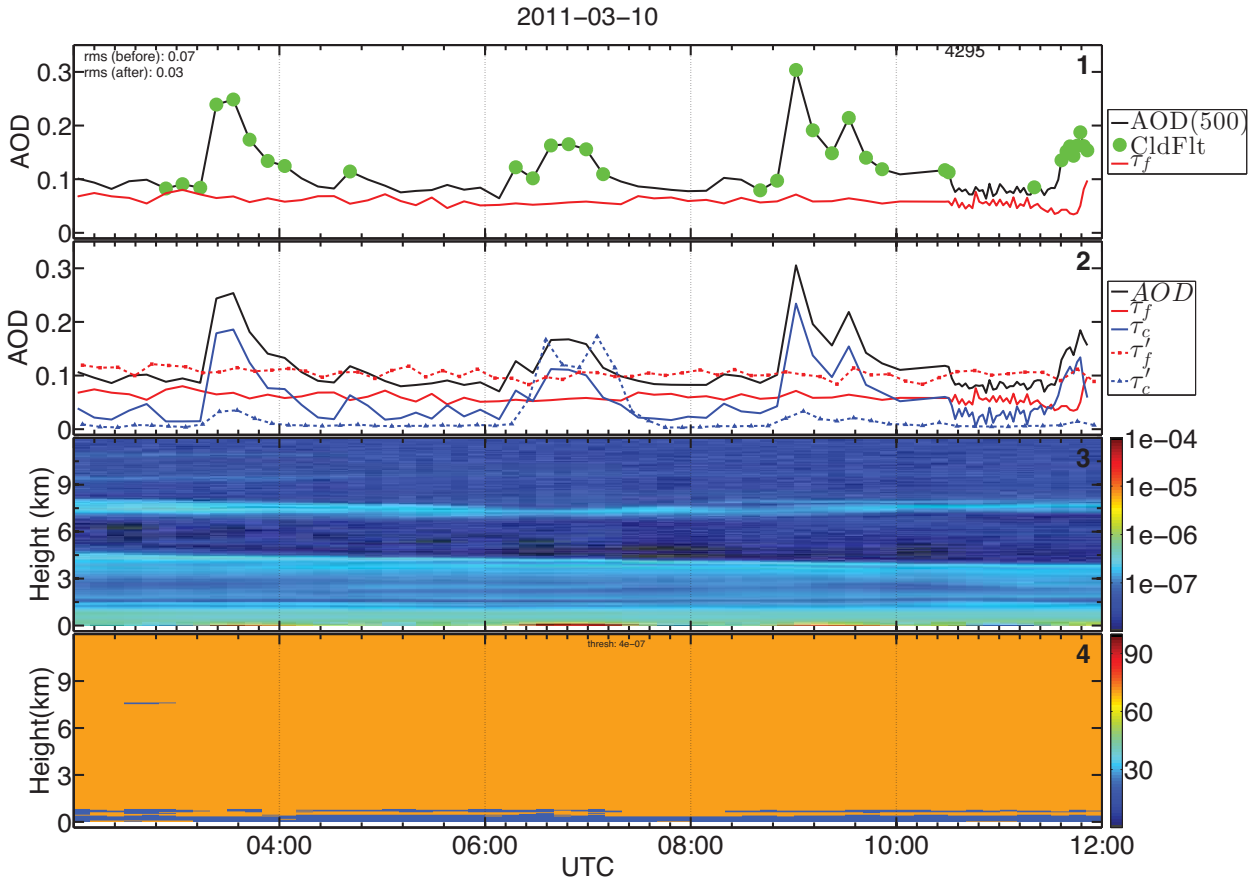

Figure 35: Pane 1: Cloud screened points based on temporal variations; fine mode starphotometry AOD is reproduced for ease of comparison; panes 2-4 as in Figure 26. Mar 10, 2011, Eureka.

As established in section 6.3.3, the AOD peaks centered at 3:25, 6:35 and 09:00 are due to surface layer ice crystals in the lowest 500m. Hence, in this case we talk about a more general coarse mode filtering rather than cloud filtering. Pane 1 shows points that were classified by the cloud filters as contaminated ('CldFlt' series), i.e. points that were associated with abrupt high-frequency temporal variations. For this date, filters performed well in flagging the optical depths associated with the coarse-mode peaks. The remaining points of the black curve (which in principle are associated only with aerosol signal) should be comparable to the fine mode red curve : the δ_f RMS difference between the two improved from 0.07 to 0.03 without and with cloud filtering. Given the limited scarcity of the starphotometry dataset, we leave aside the question of just how much the two should agree to future analyses : one could argue, for example, that

the cloud-screened AODs contain a small OD contribution due to coarse mode aerosols and/or homogeneous clouds or one could equally well question the accuracy of the SDA fine mode retrieval which becomes less accurate for small AODs (*O'Neill et al.*, 2003).

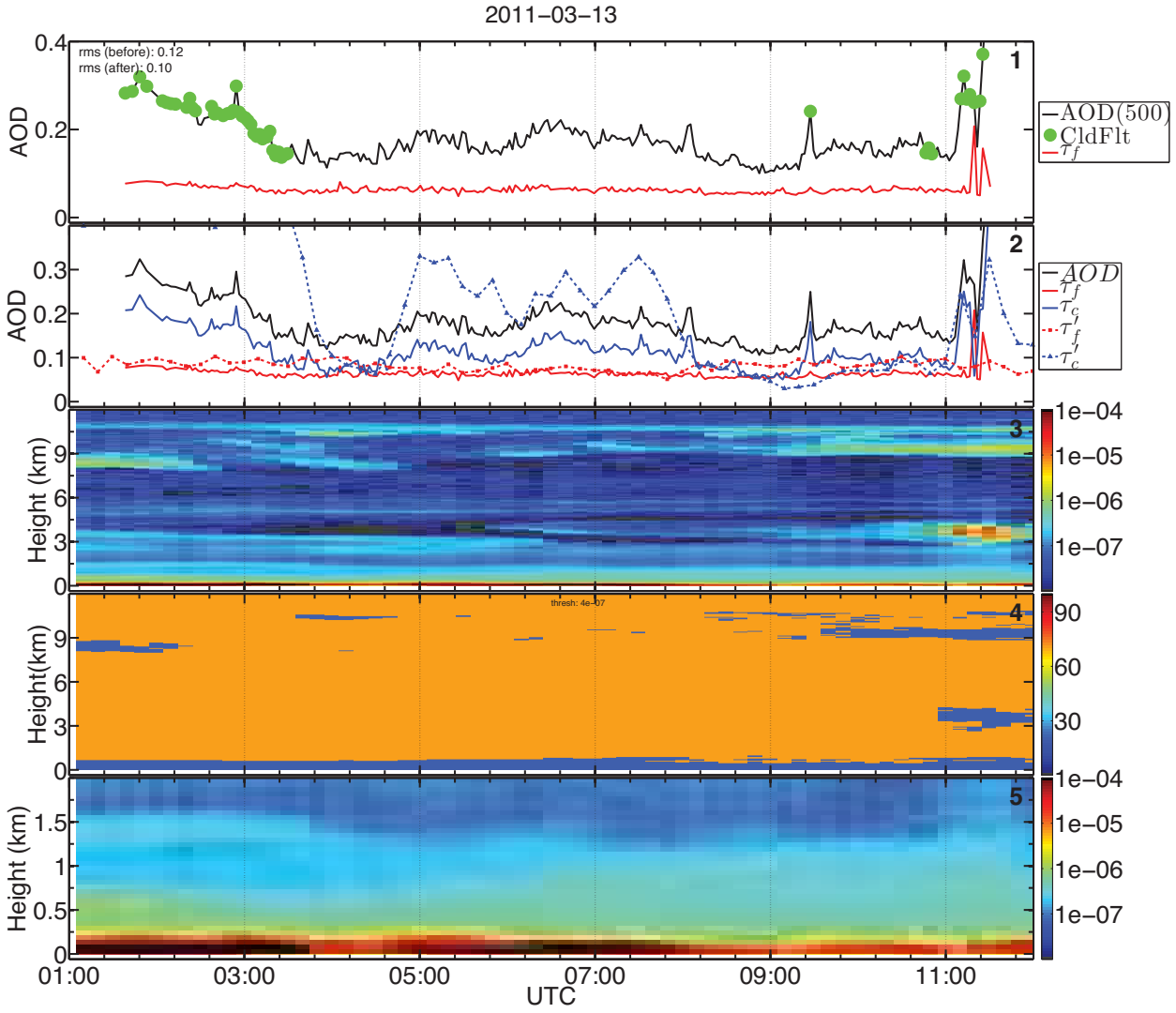

Figure 36: Panes 1-4 as in Figure 35; pane 5 - is an extract from pane 3 for the lowest 2km. Mar 13, 2011 at Eureka.

Figure 36 gives another example of cloud screening for Mar 13, 2011 at Eureka. Lidar profiles show clouds dispersed vertically throughout the atmosphere mostly below 4.5km and above 7.5km. Additional lidar analysis indicates that, in a similar fashion to the Mar. 10, 2011 event, the optical signal is also modulated by the presence of ice crystals patches

in the lowest 500m (pane 5 shows the lowest 2km in lidar profiles). The extinction due to ice crystals is particularly strong before 3:45 and between 4:15 and 8:15 as manifested by the enhanced τ_c' signal (and the SDA derived coarse mode optical depth) during these time frames. Temporal cloud screening, in this case, manages to detect significant coarse mode variations before 3:30 and after 11:00. The procedure, however, fails to screen the low-frequency varying central feature between 4:15 to 8:15. The values of δ_f before and after cloud screening are 0.12 and 0.10 which is only a minor improvement. τ_f agrees well with τ_f' and stays relatively constant at 0.06 throughout the night. On the other hand, the mean AOD between 4:15 and 8:15 would be 0.18 if one chose to believe the poorly cloud-screened total starphotometry signal.

The results from using BSRN data as an additional means to validate cloud screening were mixed. For some opaque clouds the difference in δ_{IR} relative to a clear sky case ($\delta_{IR}(clearsky) - \delta_{IR}(cloud)$) could reach up to 40 W/m^2 and clearly indicated cloud presence. For thinner clouds, however, the δ_{IR} difference values were much smaller. Figure 37 shows the data from Jan 29, 2011 at Ny Ålesund. Two coarse mode peaks centered at 16:00 and 18:00 are evident from the starphotometry data (panes 1 and 2). This is confirmed by the lidar profiles in pane 4, indicating cloud features between 4 and 7km (no KARL profiles were available for this date, so MPL level 0 data was used instead). Level 0 is associated with little or no quality control, but for the purposes of this example it was judged to be sufficient as only cloud presence/absence needed to be established). Temporal cloud screening successfully detects high-frequency cloud features, except for cases of weaker cloud optical depth variation (for example, at the beginning of the cloud events around 14:30 UTC). The associated differences in δ_{IR}, however, are less conclusive. The value of δ_{IR} has decreased by about 7 W/m^2 and 12 W/m^2 for the first (15:00-17:00) and second (17:00-19:00) coarse mode features, respectively, so it is clear that δ_{IR} reacts to clouds. However, a similar decrease of 9 W/m^2 can be observed between 11:00 and 13:00 and should indicate a presence of another cloud in that time interval. The lidar profiles do not, however, show any clouds of comparable backscatter values to those observed after 14:30. These mixed results are representative of other days. The decrease in δ_{IR} can often confirm cloud presence but it is not always corroborated by starphotometry and lidar data. Furthermore, it is hard to define a specific δ_{IR} difference threshold for automatic cloud detection, as different clouds are associated with different decrease in δ_{IR}.

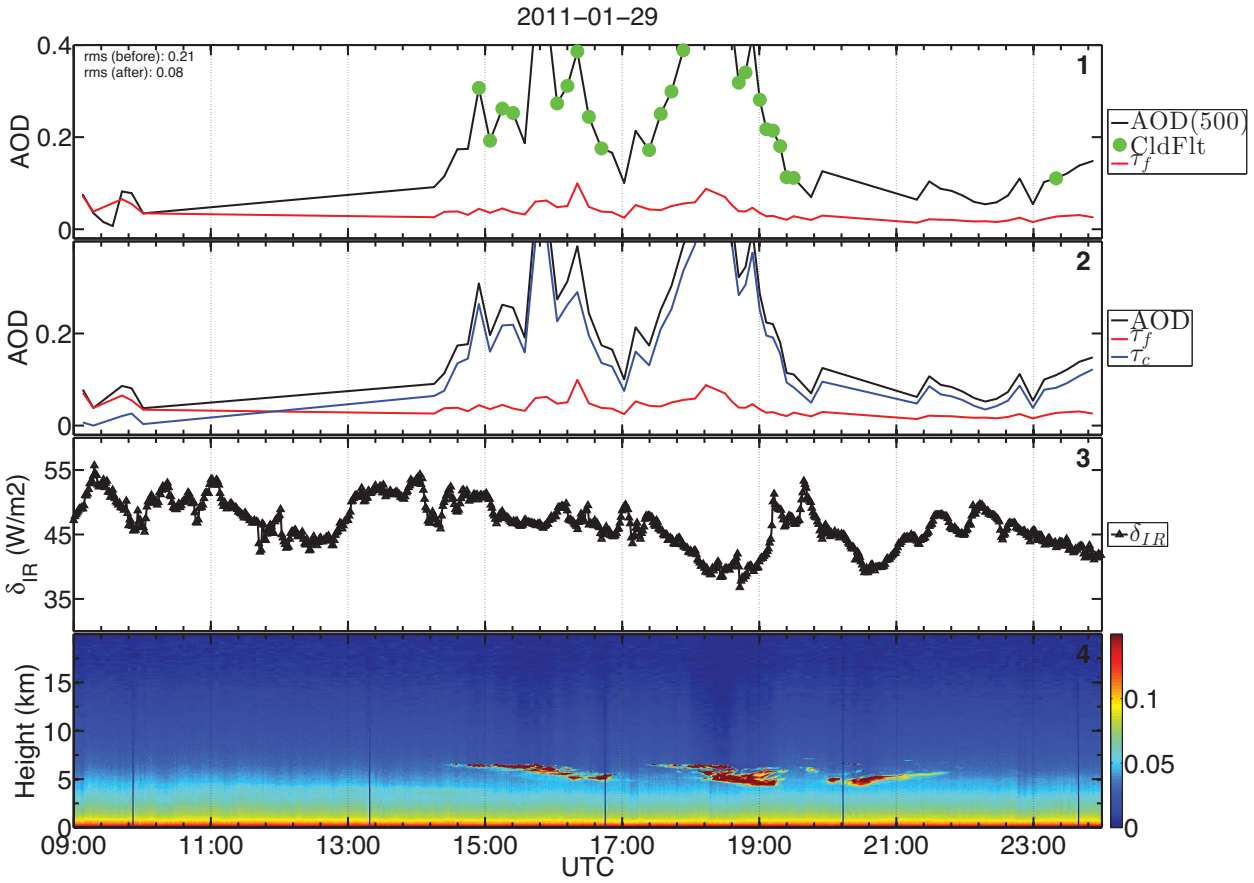

Figure 37: Panes 1 and 2 as in Figure 35; pane 3: difference between upwelling and downwelling IR radiation (δ_{IR}) as measured by Eppley Precision Infrared Radiometer; pane 4: MPL normalized relative backscatter in $counts/(\mu s \mu J)km^2$. Jan 29, 2011 at Ny Ålesund

6.5 Seasonal trends

The size of the datasets obtained were relatively small in terms of undertaking any meaningful climatological analysis. We nevertheless analyzed data on a larger temporal scale with an eye towards possible seasonal trends, similar to those shown in (*Herber et al.*, 2002). Figure 38 to 41 show the composite of all the starphotometry and lidar data acquired during the two seasons at Eureka and Ny Ålesund. For Eureka, few data points were acquired in the fall of 2010 (Oct-Dec), so the data is shown only for the spring period of 2011 (Feb-Mar). In these figures, the top pane shows the daily AOD averages as well as daily averages of the data based on temporal and spectral cloud screening (the

latter refers to the SDA fine-mode AOD). The bottom pane shows the 532 nm, CRL or KARL backscatter coefficient.

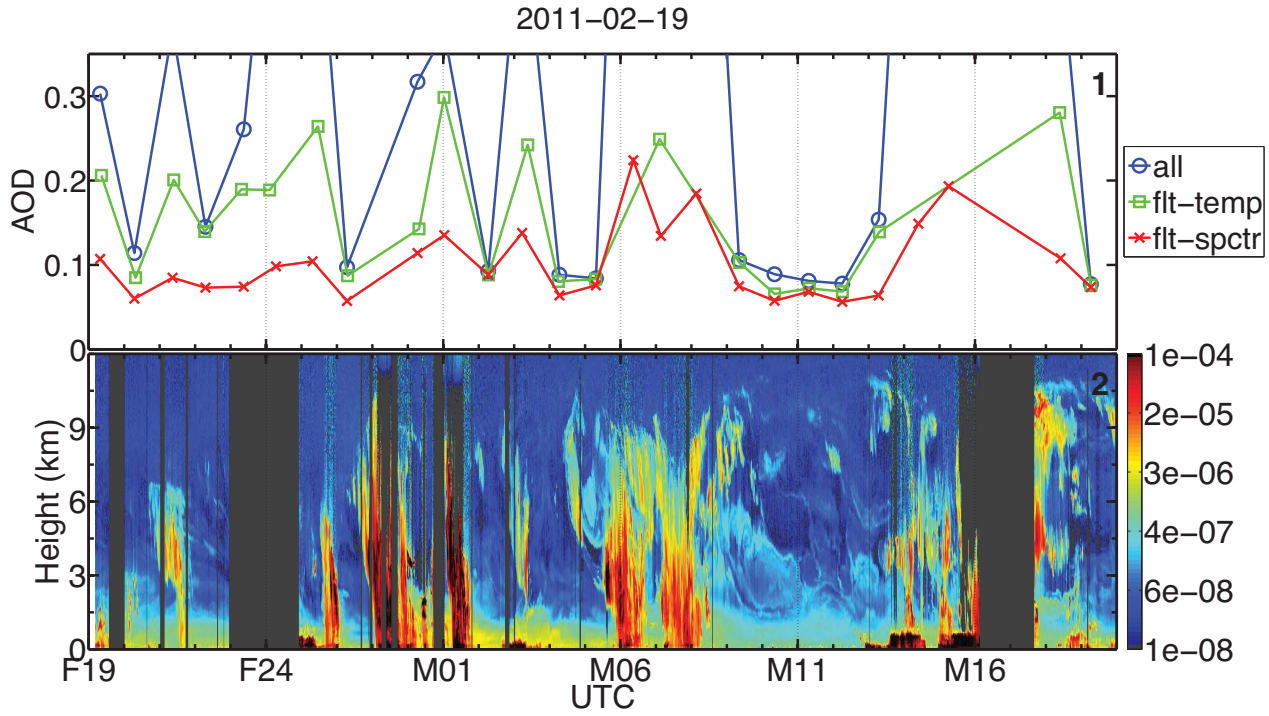

Figure 38: Starphotometry and lidar observations at Eureka for the period February 19, 2011 and March 19, 2011. Top: daily AOD averages at 532nm, Bottom: CRL 532nm backscatter cross-section ($m^{-1}sr^{-1}$).

No distinct seasonal or interannual trends were detected in the data. AOD values at Eureka were generally higher and exhibited larger variations than at Ny Ålesund. The mean fine-mode AODs (followed by the standard deviation in brackets) at Eureka were 0.10 (0.05) and 0.12 (0.06) for Feb 19-Mar 19, 2011 and Feb 25-Mar 30, 2012 respectively. For Ny Ålesund these values were 0.04 (0.02) and 0.10 (0.04) for Nov 10, 2010-Feb 24, 2011 and Nov 10, 2011-Mar 29, 2012. Temporal cloud screening has substantially reduced day-to-day high frequency variations even though there appears to be significant residual effect (a post cloud screening influence of clouds). Furthermore, temporally screened data agreed reasonably well with spectrally screened data at Ny Ålesund. The RMS differences between the two data series were 0.04 and 0.03 for 2010-11 and 2011-12, respectively. For Eureka, these values for the two series of Figures 38 and Figure 39 were higher: 0.09 and 0.11 respectively.

On the whole we could characterize the results as being sensitive to the presence of

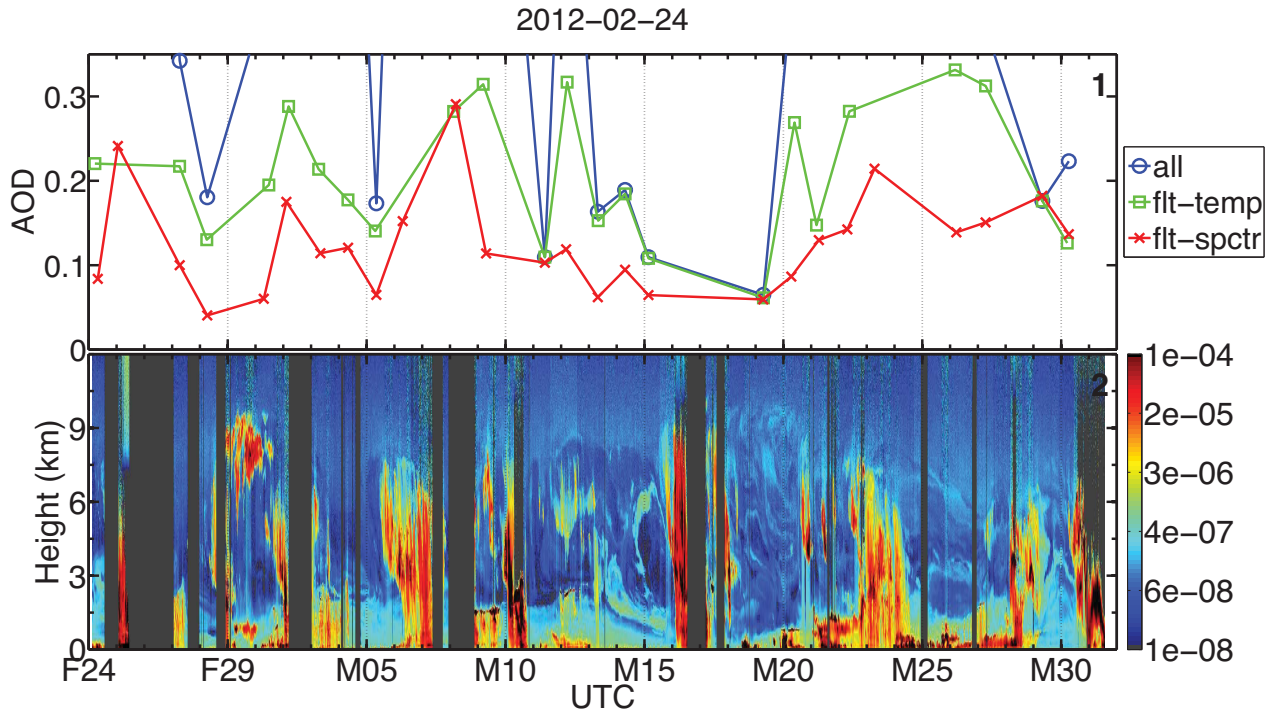

Figure 39: Same as Figure 38, but for February 24, 2011 - March 30, 2012.

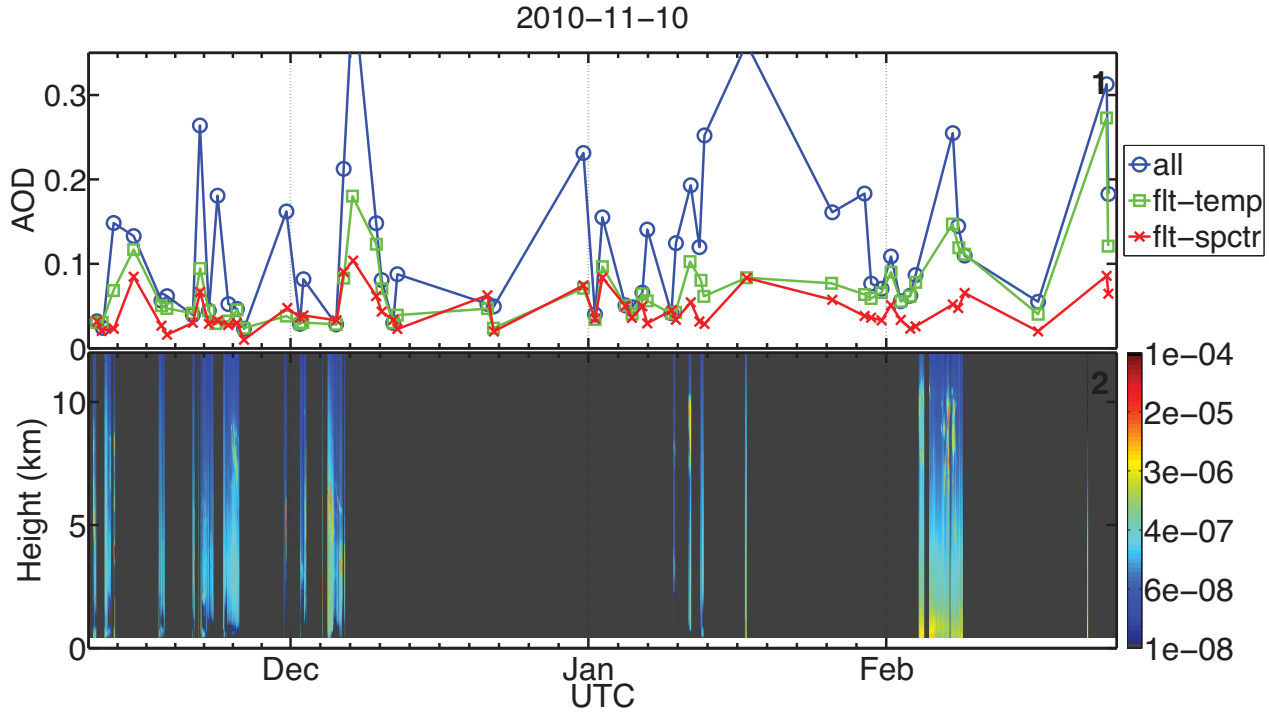

Figure 40: Starphotometry and lidar observations at Ny Ålesund for November 10, 2010- February 24, 2011. The top pane is similar to Figure 38. The bottom pane is KARL aerosol backscatter coefficient at 532nm ($m^{-1}sr^{-1}$).

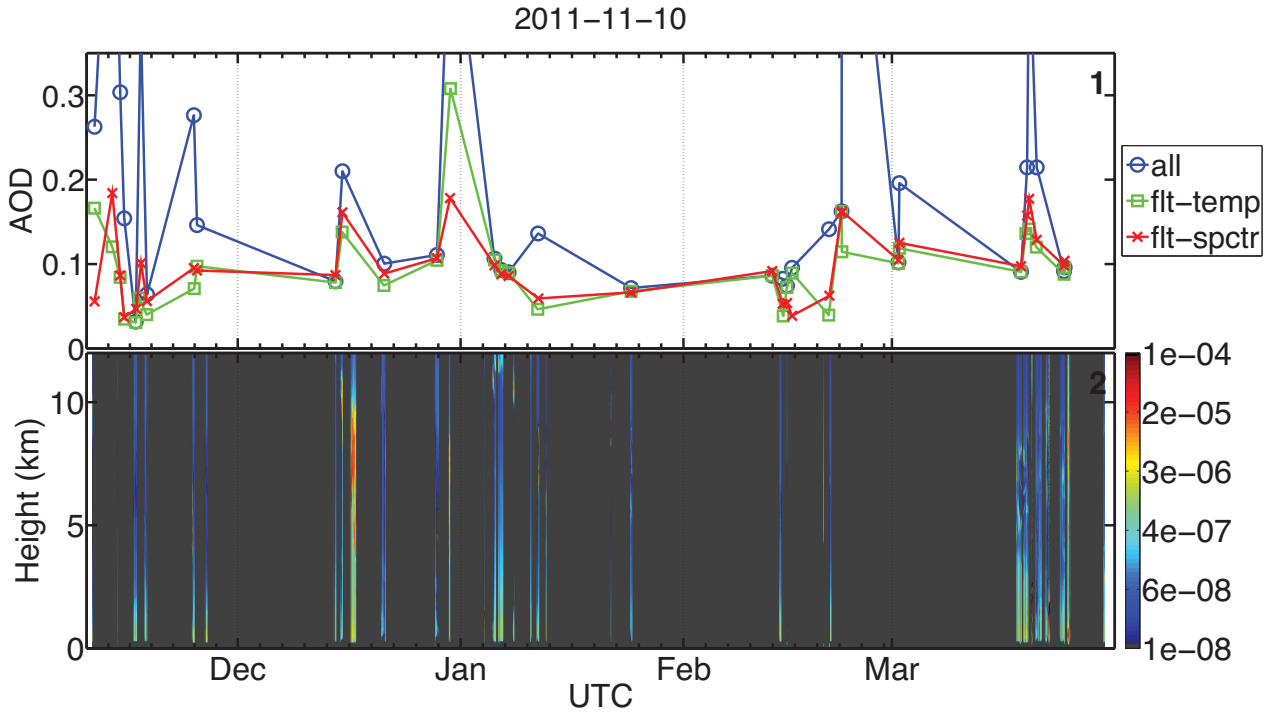

Figure 41: Same as Figure 40, but for November 10, 2011- March 29, 2012

clouds even, apparently, when cloud screening has been applied (the appearance of high frequency variations in the "fit-temp" and "fit-spectr" curves in the presence of strong variations of the backscatter profiles and the "all" category of optical depths would lead one to suspect a residual influence of clouds especially when those clouds are significantly larger in amplitude then the nominally cloud-filtered results). Remembering here that the objective is an AOD seasonal climatology (where a defining sampling frequency of $\approx$ weeks^{-1} would be acceptable) we can well afford to be stricter in our selection criteria in order to achieve an AOD climatology of more significant import. For Figure 38 to 41 we have accordingly defined a "minimal-cloud envelope" (CldEnv time series) which consists only of points where the time series "all", "flt-temp" and "flt-spctr" agree to better than 0.04 (see Appendix A) . As shown in Table 4, the average τ_f values agree to within 0.01 (with the exception of 0.02 for Eureka, 2010-11) with the minimal-cloud envelope. However the "CldEnv" values also exhibit less spread as indicated by smaller standard deviation values (a change which is again most significant for the 2010-11 Eureka values of τ_f). This lends a degree of greater confidence to these refiltered daily averages.

Seasonal AOD dynamics, represented by Eureka and Ny Ålesund minimal-cloud envelopes, are shown in Figure 42. Also shown, are vertically integrated CALIOP seasonal

Table 4: Seasonal averages and standard deviations (σ) of fine-mode AOD and minimal-cloud envelope

	τ_f		CldEnv	
	Mean	σ	Mean	σ
Eureka 2010-11	0.10	0.05	0.08	0.01
Eureka 2011-12	0.12	0.06	0.12	0.06
Ny Ålesund 2010-11	0.04	0.02	0.04	0.01
Ny Ålesund 2011-12	0.10	0.04	0.09	0.03

extinction values for the European (ERP) and North American (NAM) sectors based on Figure 9 of *Di Pierro et al.*, 2013 (the extinction values were converted to km^{-1}, multiplied by the appropriate altitude interval and summed up).

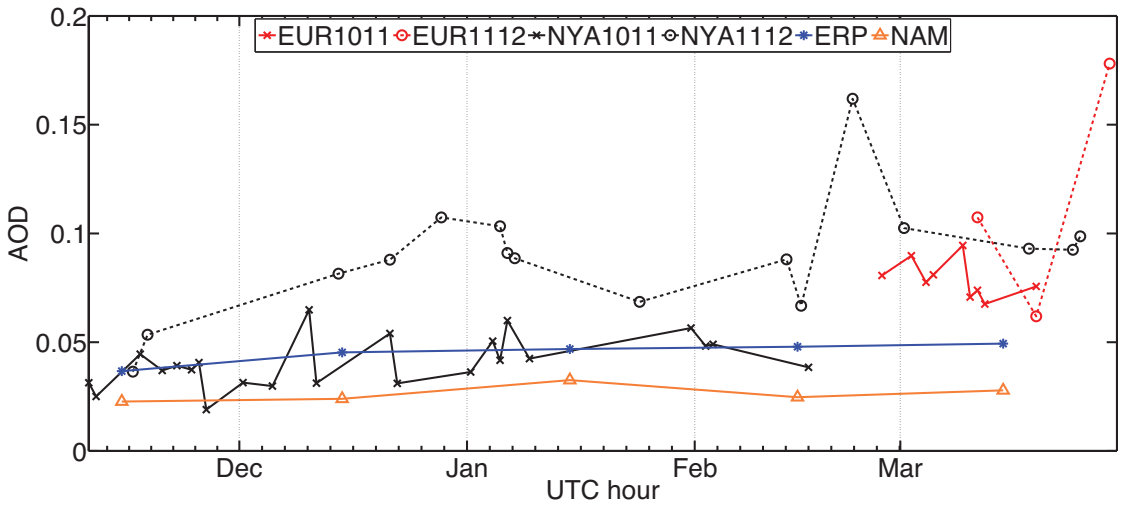

Figure 42: Eureka and Ny Ålesund minimal-cloud envelopes for 2010-11 and 2011-12. Also shown are mean CALIOP AODs for 2006-2012 (ERP - Europe, NAM - North America) based on Figure 9 of *Di Pierro et al.*, 2013

In general, starphotometry AODs were higher than those estimated using CALIOP extinction profiles with a notable exception of NYA 2011-12 associated with the best agreement of the two datasets. While significantly underestimated CALIOP values are possible given problems associated with lower limit detectability threshold of CALIOP (see section 5.5), there are other factors in play. The higher starphotometer τ_f values for Ny Alesund (NYA1112) during December and January are quite possibly related to the PSC activity seen in Figure 24 (and commented on in the text associated with Figure 32) since the CALIOP AOD integrations stop at 8 km altitude. However Figure 24 does

not explain the large τ_f peak observed in the latter stages of February.

Similarly to Figure 42, Figure 47 of Appendix B gives comparisons with CALIOP seasonal extinction values for 2010-11 and 2011-12. The average Nov.-Mar. AODs for these seasons were 0.04 and 0.03 respectively. As in the case of Figure 42, starphotometry AODs were generally higher than CALIOP values. Also, contrary to the CALIOP inter-annual dynamics, ground-based AODs were higher during the Polar Winter of 2011-12.

Chapter 7

Summary, conclusions and future work

Optical measurements, and specifically AOD measurements, during the Polar Winter are extremely scarce and present a substantial contribution to climatological studies, instrumental intercomparisons, satellite validation (such as CALIOP) and model tie-down points. This work is based on starphotometry and lidar data synchronously obtained at the Eureka and Ny Ålesund High Arctic stations during the Polar Winters of 2010-11 and 2011-12. The very process of obtaining starphotometry AOD measurements is quite problematic in the Arctic due to high precision requirements in some of the harshest and logistically challenging conditions on the planet. We acquired a total of more than 300 and 500h of AOD data using SPSTAR starphotometers during 2010-11 at Eureka and Ny Ålesund respectively. These numbers were about 200 and 230h during 2011-12. AOD measurements were accompanied whenever possible by simultaneously acquired vertical aerosol and thin cloud profiles from the CRL and KARL Raman lidars.

Starphotometry is a relatively new technology that is subject to weak-signal problems exacerbated in the extreme Arctic conditions. The accuracy of the derived AODs ultimately depends on the choice of calibration values and other instrumental and environmental factors such as optics degradation or background field characterization. In particular, it was shown that ice crystal deposition on the collecting telescope could result in significant and false increase in OSM AOD (*Ivanescu*, 2013). TSM AODs obtained using a differential technique are affected to a lesser extent (idem). Given the slowly changing air masses for most measurement stars, Langley calibration is problematic in the Arctic. The SPSTAR was calibrated using differential two-star measurements. Only points satisfying AOD range and measurement uncertainty criteria were considered for calibration. The quality of the calibration values (C) was confirmed by studying their

evolution throughout the entire measurement period. The AOD errors due to the spread in the potential calibration values were estimated to be 0.025. The total error in AOD, $\delta(\tau_{aer})$, was estimated to be $\delta(\tau_{aer}) \lesssim 0.03$ (for air mass of 1).

Short-time scale ($\approx$ minutes) process-level analysis of aerosol and cloud events simultaneously captured in photometric and lidar data is essential to ensure that extracted extensive (bulk) and intensive (per particle) optical and microphysical indicators are coherent and physically consistent. At the same time, this type of analysis is rarely addressed in the literature and we have found no measurement series that deal with process-level analysis of Polar Winter datasets. Using the starphotometry-lidar synergy we have detected and characterized several distinct events throughout the measurement periods. In particular, we provided case studies of : aerosols (Eureka: Mar 9-12, 2011, Mar 13-15, 2012), ice crystals (Eureka: Mar 10, 2011), thin clouds (Eureka: Feb 21, 2011), and fine-mode polar stratospheric clouds (Ny Ålesund: Jan 5-6, 2012). For this analysis, we employed prescribed values of extinction to backscatter lidar ratio values and applied these values to a simple threshold based classification of the lidar backscatter images. In general, there was good agreement in terms of the physical coherence between fine and coarse mode starphotometry ODs (τ_f and τ_c) and corresponding lidar optical depths (LODs) of aerosol and cloud layers (τ'_f and τ'_c). Nevertheless, several inconsistencies were also found between the instruments. For the aerosol event of Mar 13-15, 2012, we argued that the source of unconfirmed starphotometry AOD increase could be due to the ice crystals deposition on the telescope. Another intriguing example of an inconsistency was the relatively weak coarse mode LODs associated with ice crystals of Mar 10, 2011 compared with the value of τ_c from the starphotometer. This discrepancy was explained by an incomplete lidar overlap correction.

Studying seasonal aerosol trends necessitates cloud-screening procedures. We have developed several tests that help detect cloud-contaminated AODs based on high-frequency AOD variations. In addition, we used fine-mode AOD as a means of performing de facto spectral cloud screening. In general, a combination of temporal filters performs well for most cloud features with optical depths that have been removed by the cloud screening being in good agreement with peaks in both τ_c and τ'_c. Temporal cloud screening, nevertheless, predictably fails for low-frequency variations associated with ice crystals or homogeneous clouds. In this case, spectral cloud screening has a distinct advantage of not being dependent on temporal variations.

The results from using BSRN radiation data as an additional means to validate cloud

screening were mixed. The difference between the upwelling and downwelling IR radiation (δ_{IR}) was effective to a degree in indicating cloud presence (in the case of opaque clouds). In the case of several thin clouds, however, variations in δ_{IR} were insufficient or did not correlate with either starphotometry or lidar data. We are progressively increasing our database and testing the sensitivity of the SDA and temporal cloud screening to algorithmic parameterizations. Ultimately we hope to arrive at a robust method for the temporal / spectral cloud-screening of starphotometer (and sunphotometer) data.

Despite the scarcity of the datasets, we analyzed daily averaged starphotometry data with an eye towards possible trends. We found that even after the application of cloud screening, the resulting fine mode optical depths could still exhibit an apparent influence of clouds. A more restrictive, second-pass, clear sky criterion ("minimal cloud envelope") produced mean 2010-11 AOD seasonal values of 0.08 and 0.04 for Eureka and Ny Ålesund respectively. In 2011-12 the values were 0.12 and 0.09. These values were generally higher than AODs calculated from the CALIOP six-year aerosol extinction climatology (Nov.-Mar. average values of ≈ 0.03 and 0.05 for North American and European sectors respectively). The apparent inter-annual increase in starphotometry AODs is in dissonance with integrated CALIOP profiles, which give mean Nov.-Mar. AODs of 0.04 and 0.03 for 2010-2011 and 2011-2012 respectively. The CALIOP AODs of the *Di Pierro et al.*, 2013 climatology were, however, calculated for 0-8km altitude range and are thus somewhat underestimated. Furthermore, in reviewing individual CALIOP profiles, we noticed that some large backscatter contributions (especially in the lowest 2km) could be eliminated or retained depending on the threshold employed. This sensitivity problem requires more analysis.

We conclude by saying that the synergism employed in the present work enabled the assemblage of evidence for events whose process-level understanding will inevitably generate greater confidence in starphotometer retrievals as well as starphotometer/ lidar comparisons and will lead to the improvement of critical statistics such as multi-year climatologies. Such an assemblage is non trivial in a low AOD (low signal to noise) environment such as the Arctic.

7.1 Future work

Given the scarcity of the available data, the single most relevant recommendation of this work pertains to the increase of both starphotometry and lidar measurements through-

out the winter period. Ideally, one should strive to obtain uninterrupted night-time measurements from November to April which would inevitably supply more events for process-level analysis, yield better climatological and statistical trends and result in a significantly larger dataset for model and satellite validation. A feasible solution to this challenging task of data acquisition is the remote operation of the instruments from mid-latitudes. Some significant strides in this direction have already been made for Eureka (eg. *Nott et al.*, 2012 with the CRL and recent work by our group using web cameras and remote control capabilities offered by the latest generation of the SPSTAR, the new alta-azimuth mount and a much improved dome).

As the aerosol measurement database grows with time, it will become feasible and increasingly important within the context of Arctic climate change, to compare the data with models. Polar Winter model runs focused specifically on aerosol properties and transport in the Arctic are only beginning to be validated. Within the context of this work, it was planned to use GEM-AQ (Global Environmental Multiscale model with Air Quality processes, *Kaminski et al.*, 2008; *Gong et al.*, 2012) in an effort to reproduce aerosol events detected with starphotometry and lidars. One distinct advantage of GEM-AQ is that it explicitly incorporates the Canadian Aerosol Module (CAM, *Gong*, 2003) including 5 size-resolved aerosol types that undergo processes such as coagulation, nucleation and dry and wet scavenging. Due to logistical difficulties, GEM-AQ runs were not possible for this work, but remain an important exercise for all future work.

Appendix A

Minimal-cloud envelope

Figures 43-46 show a "minimal-cloud envelope" (CldEnv, red dotted line) which consists only of days (marked with black vertical lines) where the time series "all", "flt-temp" and "flt-spctr" agree to better than 0.04. The average value of the CldEnv is shown at the left top corner of pane 1.

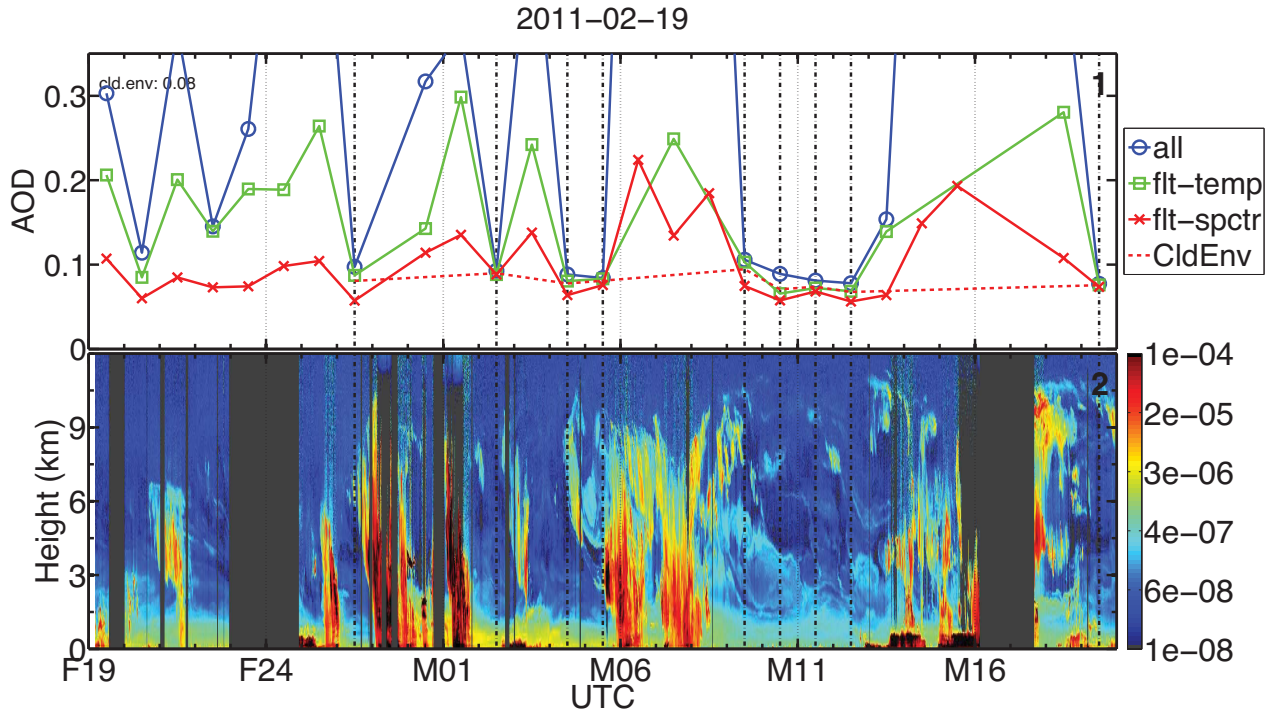

Figure 43: Same as Figure 38, but with a minimal-cloud envelope time series.

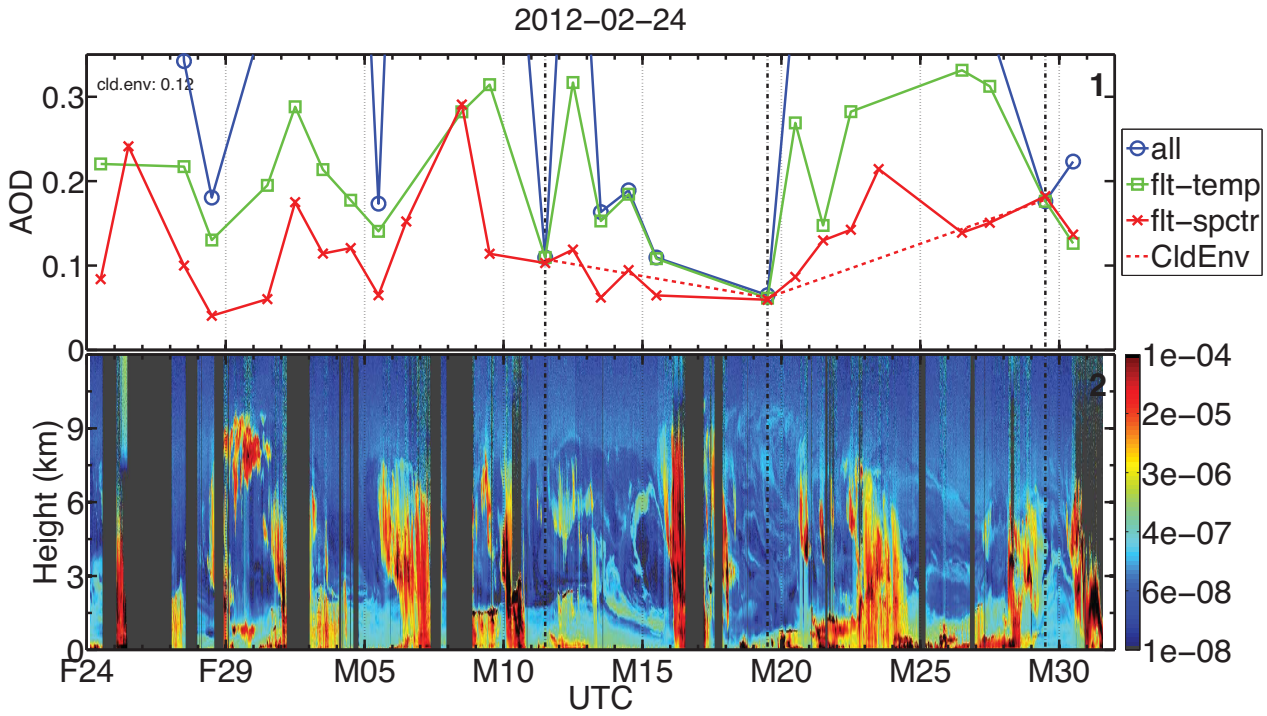

Figure 44: Same as Figure 39, but with a minimal-cloud envelope time series.

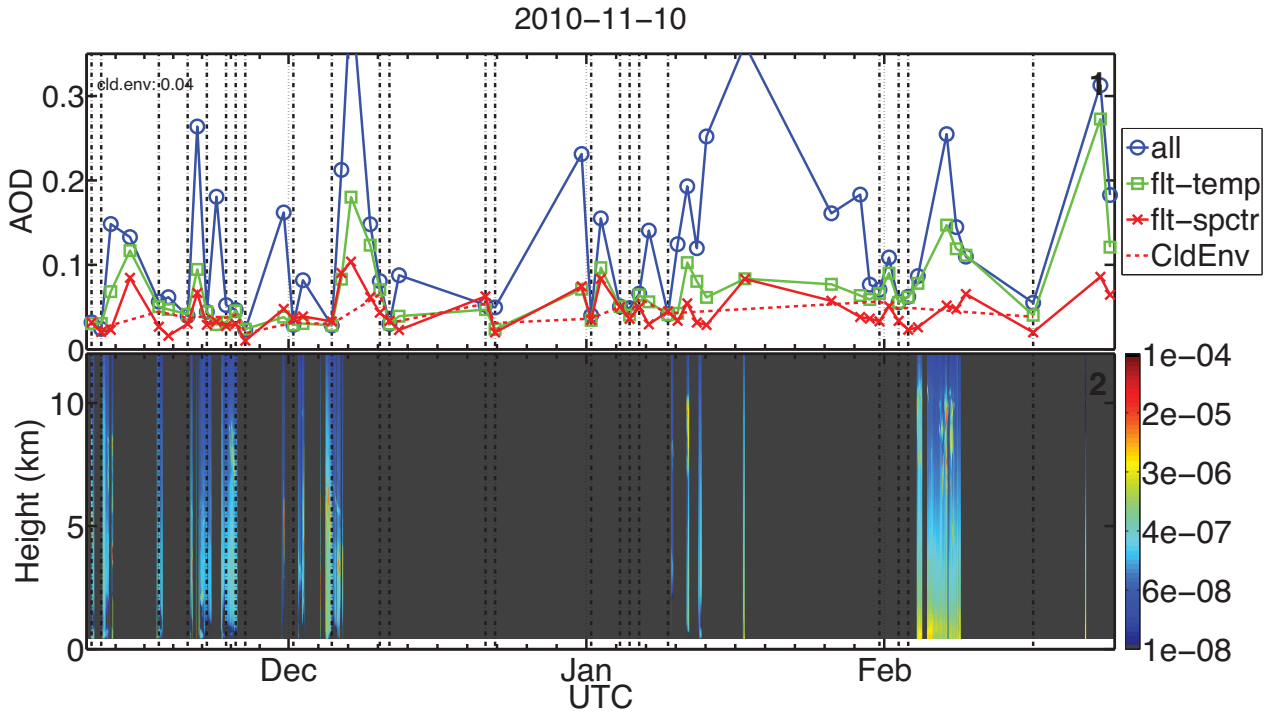

Figure 45: Same as Figure 40, but with a minimal-cloud envelope time series.

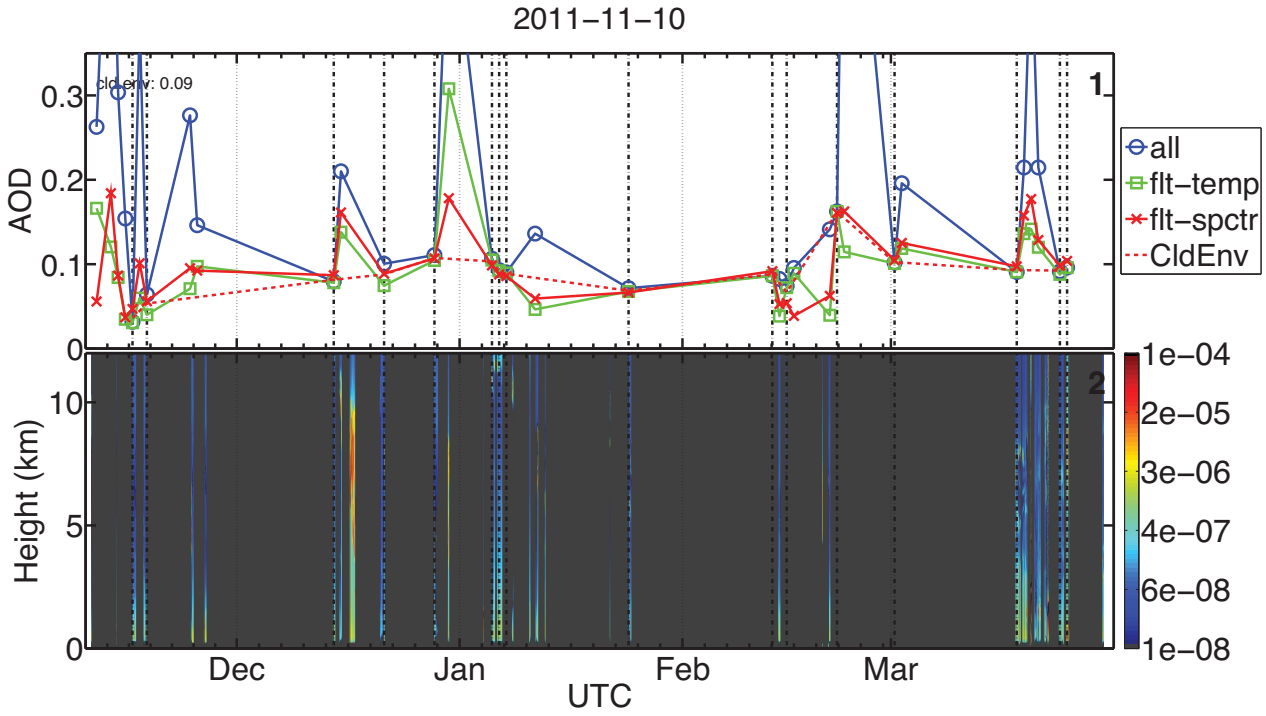

Figure 46: Same as Figure 41, but with a minimal-cloud envelope time series.

Appendix B

Comparisons with CALIOP seasonal AODs

Figure 47 shows integrated CALIOP seasonal extinction values for 2010-11 and 2011-12 based on Figure 13 of *Di Pierro et al.*, 2013 (the extinction values were converted to km^{-1}, multiplied by the appropriate altitude interval and summed up).

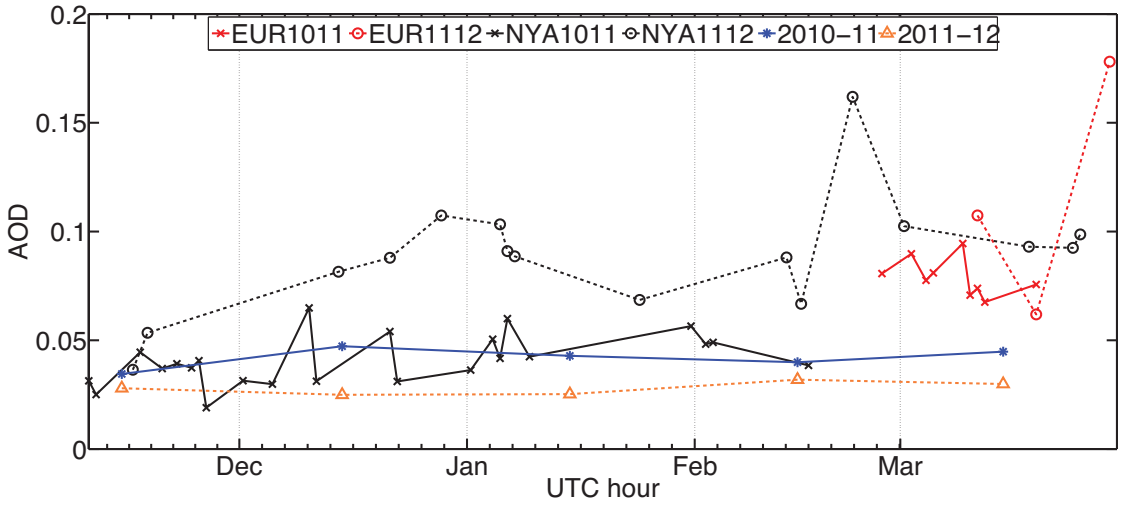

Figure 47: . Eureka and Ny Ålesund minimal-cloud envelopes for 2010-11 and 2011-12. Also shown are mean CALIOP AODs for 2010-2011 and 2011-12 based on Figure 13 of *Di Pierro et al.*, 2013

Bibliography

Alados-Arboledas, L., D. Müller, J. L. Guerrero-Rascado, F. Navas-Guzmán, D. Pérez-Ramírez, and F. J. Olmo (2011), Optical and microphysical properties of fresh biomass burning aerosol retrieved by Raman lidar, and star-and sun-photometry, *Geophysical Research Letters*, *38*(1), n/a–n/a, doi:10.1029/2010GL045999. 22, 50

AMAP (2011), *The Impact of Black Carbon on Arctic Climate. By: Quinn, P.K. Stohl, A. Arneth, A. Berntsen, T. Burkhart, J. F. Christensen, J. Flanner, M. Kupiainen, K. Lihavainen, H. Shepherd, M. Shevchenko, V. Skov, H. Vestreng, V.*, 72 pp., Arctic Monitoring and Assessment Programme (AMAP), Oslo. 16, 36

Angstrom, A. (1964), The parameters of atmospheric turbidity, *Tellus*, *XVI*, 64–75. 33

Ansmann, A., U. Wandinger, M. Riebesell, C. Weitkamp, and W. Michaelis (1992), Independent measurement of extinction and backscatter profiles in cirrus clouds by using a combined Raman elastic-backscatter lidar., *Applied optics*, *31*(33), 7113, doi:10.1364/AO.31.007113. 19, 71

ASDC (2013), CALIPSO Quality Statements: Lidar Level 2 Cloud and Aerosol Profile Products Version Releases: 3.01, 3.02, distributed by Atmospheric Science Data Center, *Tech. rep.* 71, 73

Baibakov, K. (2009), Characterization of night-time aerosols using starphotometry, M.Sc. thesis, University of Sherbrooke. 24, 30, 39, 61

Balis, D. (2003), Raman lidar and sunphotometric measurements of aerosol optical properties over Thessaloniki, Greece during a biomass burning episode, *Atmospheric Environment*, *37*(32), 4529–4538, doi:10.1016/S1352-2310(03)00581-8. 50

Barreto, A., E. Cuevas, B. Damiri, C. Guirado, T. Berkoff, A. J. Berjón, Y. Hernández, F. Almansa, and M. Gil (2012), A new method for nocturnal aerosol measurements

with a lunar photometer prototype, *Atmospheric Measurement Techniques Discussions*, *5*(4), 5527–5569, doi:10.5194/amtd-5-5527-2012. 18

Berkoff, T. A., M. Sorokin, T. Stone, T. F. Eck, R. Hoff, E. Welton, and B. Holben (2011), Nocturnal Aerosol Optical Depth Measurements with a Small-Aperture Automated Photometer Using the Moon as a Light Source, *Journal of Atmospheric and Oceanic Technology*, *28*(10), 1297–1306, doi:10.1175/JTECH-D-10-05036.1. 18

Blanchet, J.-P., and E. Girard (1994), Arctic 'greenhouse effect', *Nature*, *371*(6496), 383–383, doi:10.1038/371383a0. 47, 53

Bodhaine, B. A., and E. G. Dutton (1993), A long-term decrease in Arctic haze at Barrow, Alaska, *Geophysical Research Letters*, *20*(10), 947–950, doi:10.1029/93GL01146. 49

Bodhaine, B. A., N. B. Wood, E. G. Dutton, and J. R. Slusser (1999), On Rayleigh Optical Depth Calculations, *Journal of Atmospheric and Oceanic Technology*, *16*(11), 1854–1861. 43

Bourdages, L., T. J. Duck, G. Lesins, J. R. Drummond, and E. W. Eloranta (2009), Physical properties of High Arctic tropospheric particles during winter, *Atmos. Chem. Phys.*, *9*(18), 6881–6897, doi:10.5194/acp-9-6881-2009. 54

Bourgeois, Q., and I. Bey (2011), Pollution transport efficiency toward the Arctic: Sensitivity to aerosol scavenging and source regions, *Journal of Geophysical Research*, *116*(D8), D08,213, doi:10.1029/2010JD015096. 48

Bradley, R. S., F. T. Keimig, and H. F. Diaz (1992), Climatology of surface-based inversions in the North American Arctic, *Journal of Geophysical Research: Atmospheres*, *97*(D14), 15,699–15,712, doi:10.1029/92JD01451. 47

Campbell, J. R., D. L. Hlavka, E. J. Welton, C. J. Flynn, D. D. Turner, J. D. Spinhirne, V. S. Scott, and I. H. Hwang (2002), Full-Time, Eye-Safe Cloud and Aerosol Lidar Observation at Atmospheric Radiation Measurement Program Sites: Instruments and Data Processing, *Journal of Atmospheric and Oceanic Technology*, *19*(4), 431–442, doi:10.1175/1520-0426(2002)019<0431:FTESCA>2.0.CO;2. 43

Campbell, J. R., J. L. Tackett, J. S. Reid, J. Zhang, C. a. Curtis, E. J. Hyer, W. R. Sessions, D. L. Westphal, J. M. Prospero, E. J. Welton, a. H. Omar, M. a. Vaughan,

and D. M. Winker (2012), Evaluating nighttime CALIOP 0.532 μm aerosol optical depth and extinction coefficient retrievals, *Atmospheric Measurement Techniques*, *5*(9), 2143–2160, doi:10.5194/amt-5-2143-2012. 73

Carswell, A. I. (1983), Lidar measurements of the atmopshere, *Can. J. Phys.*, *61(2)*, 378–395. 41, 42

Cattrall, C., J. Reagan, K. Thome, and O. Dubovik (2005), Variability of aerosol and spectral lidar and backscatter and extinction ratios of key aerosol types derived from selected Aerosol Robotic Network locations, *J.Geophys.Res.*, *110*. 43

Cordoba-Jabonero, C., M. Gil, M. Yela, M. Maturilli, and R. Neuber (2009), Polar Stratospheric Cloud Observations in the 2006/07 Arctic Winter by Using an Improved Micropulse Lidar, *Journal of Atmospheric and Oceanic Technology*, *26*(10), 2136–2148, doi:10.1175/2009JTECHA1250.1. 55

Curry, J. A., F. G. Meyer, L. F. Radke, C. A. Brock, and E. E. Ebert (1990), Occurrence and characteristics of lower tropospheric ice crystals in the arctic, *International Journal of Climatology*, *10*(7), 749–764, doi:10.1002/joc.3370100708. 20, 47

Curry, J. A., J. L. Schramm, and E. E. Ebert (1995), Sea Ice-Albedo Climate Feedback Mechanism, *Journal of Climate*, *8*(2), 240–247, doi:10.1175/1520-0442(1995)008<0240:SIACFM>2.0.CO;2. 53

Daou, D. (2014), Charactérisation des aérosols par inversion des données combinées des photomètres et lidars au sol, Ph.D. thesis (in revision). 45

Di Pierro, M., L. Jaeglé, E. W. Eloranta, and S. Sharma (2013), Spatial and seasonal distribution of Arctic aerosols observed by the CALIOP satellite instrument (2006–2012), *Atmospheric Chemistry and Physics*, *13*(14), 7075–7095, doi:10.5194/acp-13-7075-2013. 73, 75, 76, 77, 79, 100, 104, 109

Dolgii, S. I., V. D. Burlakov, A. P. Makeev, A. V. Nevzorov, K. A. Shmirko, A. N. Pavlov, S. Y. Stolyarchuk, O. A. Bukin, A. P. Chaykovskii, F. P. Osipenko, and D. A. Trifonov (2012), Aerosol disturbances of the stratosphere after eruption of Grimsvötn volcano (Iceland, May 21, 2011) according to observations at lidar network stations of CIS countries CIS-LiNet in Minsk, Tomsk, and Vladivostok, in *Eighteenth International Symposium on Atmospheric and Ocean Optics: Atmospheric Physics*, edited by O. A.

Romanovskii, pp. 86,960I–86,960I–4, International Society for Optics and Photonics, doi:10.1117/12.2008709. 80

Doyle, J. G., G. Lesins, C. P. Thackray, C. Perro, G. J. Nott, T. J. Duck, R. Damoah, and J. R. Drummond (2011), Water vapor intrusions into the High Arctic during winter, *Geophysical Research Letters*, *38*(12), L12,806, doi:10.1029/2011GL047493. 53

Duarte, C. M., T. M. Lenton, P. Wadhams, and P. Wassmann (2012), Abrupt climate change in the Arctic, *Nature Climate Change*, *2*(2), 60–62, doi:10.1038/nclimate1386. 15, 16

Duck, T. (2013), Personal communication. 84

Durand, G., L. Cadelis, V. Minier, C. Veyssière, C. Walter, A. Pierre, A. Agabi, E. Fossat, and F. Jeanneaux (2007), GIVRE: A Protection Against Frost Deposit on Polar Instruments, *EAS Publications Series*, *25*, 77–80. 66

Dusek, U., G. P. Frank, L. Hildebrandt, J. Curtius, J. Schneider, S. Walter, D. Chand, F. Drewnick, S. Hings, D. Jung, S. Borrmann, and M. O. Andreae (2006), Size matters more than chemistry for cloud-nucleating ability of aerosol particles., *Science (New York, N.Y.)*, *312*(5778), 1375–8, doi:10.1126/science.1125261. 17, 37

Eck, T. F., B. N. Holben, J. S. Reid, O. Dubovik, A. Smirnov, N. T. O'Neill, I. Slutsker, and S. Kinne (1999), Wavelength dependence of the optical depth of biomass burning, urban, and desert dust aerosols, *J. Geophys. Res.*, *104*. 33

Engvall, A.-C., J. Ström, P. Tunved, R. Krejci, H. Schlager, and A. Minikin (2009), The radiative effect of an aged, internally mixed Arctic aerosol originating from lower-latitude biomass burning, *Tellus B*, *61*(4), 677–684, doi:10.1111/j.1600-0889.2009.00431.x. 20

Fairall, C. W., P. O. G. Persson, E. F. Bradley, R. E. Payne, and S. P. Anderson (1998), A New Look at Calibration and Use of Eppley Precision Infrared Radiometers. Part I: Theory and Application, *Journal of Atmospheric and Oceanic Technology*, *15*(6), 1229–1242, doi:10.1175/1520-0426(1998)015<1229:ANLACA>2.0.CO;2. 64

Forster, P., V. Ramaswamy, P. Artaxo, T. Berntsen, R. Betts, D. Fahey, J. Haywood, J. Lean, D. Lowe, G. Myhre, J. Nganga, R. Prinn, G. Raga, M. Schulz, and R. V.

Dorland (2007), 2. Changes in Atmospheric Constituents and in Radiative Forcing, in *Climate Change 2007: The Physical Science Basis. Contribution of Working Group I to the Fourth Assessment Report of the Intergovernmental Panel on Climate Change*, edited by S. Solomon, D. Qin, M. Manning, Z. Chen, M. Marquis, K. B. Averyt, M. Tignor, and H. L. Miller, Cambridge University Press, United Kingdom and New York, NY, USA. 16, 17, 35, 36

Frohlich, C., and G. E. Shaw (1980), New determination of Rayleigh scattering in the terrestrial atmosphere, *Applied Optics*, *19*(11), 1773–1775. 28, 66

Girard, E., J.-P. Blanchet, and Y. Dubois (2005), Effects of arctic sulphuric acid aerosols on wintertime low-level atmospheric ice crystals, humidity and temperature at Alert, Nunavut, *Atmospheric Research*, *73*(1–2), 131–148, doi:10.1016/j.atmosres.2004.08.002. 53

Gong, S. L. (2003), Canadian Aerosol Module: A size-segregated simulation of atmospheric aerosol processes for climate and air quality models 1. Module development, *Journal of Geophysical Research*, *108*(D1), 4007, doi:10.1029/2001JD002002. 105

Gong, S. L., D. Lavoué, T. L. Zhao, P. Huang, and J. W. Kaminski (2012), GEM-AQ/EC, an on-line global multi-scale chemical weather modelling system: model development and evaluation of global aerosol climatology, *Atmospheric Chemistry and Physics*, *12*(17), 8237–8256, doi:10.5194/acp-12-8237-2012. 105

Gröschke, A. (2009), Unpublished manuscript, Personal Communication. 25, 58, 59, 61, 65, 66

Halthore, R. N., T. F. Eck, B. N. Holben, and B. L. Markham (1997), Sun photometric measurements of atmospheric water vapor column abundance in the 940-nm band, *J. Geophys. Res.*, *102*. 31

Hansen, J., and L. Travis (1974), Light scattering in planetary atmospheres, *Space Science Reviews*, *16*, 527–610, doi:10.1007/BF00168069. 36, 44

Herber, A. (2012), Personal communication. 64

Herber, A., L. W. Thomason, H. Gernandt, U. Leiterer, D. Nagel, K.-H. Schulz, J. Kaptur, T. Albrecht, and J. Notholt (2002), Continuous day and night aerosol optical

depth observations in the Arctic between 1991 and 1999, *J.Geophys.Res.*, *107*. 18, 20, 25, 38, 49, 54, 55, 59, 63, 96

Hinds, W. C. (1999), *Aerosol technology: properties, behaviour, and measurements of airborne particles*, 2nd ed., John Wiley and Sons. 16

Hinkey, E. D. (1976), *Laser monitoring of the atmosphere*, 380 pp., Springer-Verlag, Berlin-New York. 41

Hoffman, A. (2010), Comparative Aerosol Studies based on Multi-wavelength Raman LIDAR at Ny-Ålesund, Spitsbergen, Ph.D. thesis, University of Potsdam, Germany. 70

Hoffmann, A., C. Ritter, M. Stock, M. Maturilli, S. Eckhardt, A. Herber, and R. Neuber (2010), Lidar measurements of the Kasatochi aerosol plume in August and September 2008 in Ny-Ålesund, Spitsbergen, *Journal of Geophysical Research*, *115*(September 2008), D00L12, doi:10.1029/2009JD013039. 20, 51, 55

Huntington, H., G. Weller, E. Bush, T. Callaghan, V. Kattsov, and M. Nuttall (2005), 1. An Introduction to the Arctic Climate Impact Assessment, in *Arctic Climate Impact Assessment*, Cambridge University Press, Cambridge, United Kingdom and New York, NY, USA. 16

Inoue, J., J. Liu, J. O. Pinto, and Curry (2006), Intercomparison of Arctic Regional Climate Models : Modeling Clouds and Radiation for SHEBA in May 1998, *J.Climate*, *19*, 4167–4179. 15

Intrieri, J. M., and M. D. Shupe (2004), Characteristics and Radiative Effects of Diamond Dust over the Western Arctic Ocean Region, *Journal of Climate*, *17*(15), 2953–2960, doi:10.1175/1520-0442(2004)017<2953:CAREOD>2.0.CO;2. 20, 47

Ishii, S., T. Shibata, T. Nagai, K. Mizutani, T. Itabe, M. Hirota, T. Fujimoto, and O. Uchino (1999), Arctic haze and clouds observed by lidar during four winter seasons of 1993–1997, at Eureka, Canada, *Atmospheric Environment*, *33*(16), 2459–2470, doi: 10.1016/S1352-2310(98)00397-5. 54

Istomina, L. G., W. von Hoyningen-Huene, A. A. Kokhanovsky, E. Schultz, and J. P. Burrows (2011), Remote sensing of aerosols over snow using infrared AATSR

observations, *Atmospheric Measurement Techniques Discussions*, *4*(1), 33–71, doi: 10.5194/amtd-4-33-2011. 48

Ivanescu, L. (2013), Personal communication. 102

Junge, C. (1955), THE SIZE DISTRIBUTION AND AGING OF NATURAL AEROSOLS AS DETERMINED FROM ELECTRICAL AND OPTICAL DATA ON THE ATMOSPHERE, *Journal of Meteorology*, *12*(1), 13–25, doi:10.1175/1520-0469(1955)012<0013:TSDAAO>2.0.CO;2. 37

Kaminski, J. W., L. Neary, J. Struzewska, J. C. McConnell, A. Lupu, J. Jarosz, K. Toyota, S. L. Gong, J. Côté, X. Liu, K. Chance, and A. Richter (2008), GEM-AQ, an on-line global multiscale chemical weather modelling system: model description and evaluation of gas phase chemistry processes, *Atmospheric Chemistry and Physics*, *8*(12), 3255–3281, doi:10.5194/acp-8-3255-2008. 105

Kattsov, V., and E. Källén (2005), 4. Future Climate Change: Modeling and Scenarios for the Arctic, in *Arctic Climate Impact Assessment*, Cambridge University Press, Cambridge, United Kingdom and New York, NY, USA. 15

Kaufman, Y. J., D. Tanré, and O. Boucher (2002), A satellite view of aerosols in the climate system., *Nature*, *419*(6903), 215–23, doi:10.1038/nature01091. 18

Kerzenmacher, T. E. (2005), Measurements of O_3, NO_2 and Temperature during the 2004 Canadian Arctic ACE Validation Campaign, *Geophysical Research Letters*, *32*(16), L16S07, doi:10.1029/2005GL023032. 65

Koch, D., and J. Hansen (2005), Distant origins of Arctic black carbon: A Goddard Institute for Space Studies ModelE experiment, *Journal of Geophysical Research*, *110*(D4), D04,204, doi:10.1029/2004JD005296. 48

Kokhanovsky, A., and G. de Leeuw (Eds.) (2005), *Satellite Aerosol Remote Sensing Over Land*, 388 pp., Springer+Praxis, Chichester, UK. 18

Leiterer, U., A. Naebert, T. Naebert, and G.Alekseeva (1995), A New Star Photometer Developed for Spectral Aerosol Optical Thickness Measurements in Lindenberg, *Contrib. Atmos. Physics*, *68*, 133–141. 18, 38

Lesins, G., L. Bourdages, T. J. Duck, J. R. Drummond, E. W. Eloranta, and V. P. Walden (2009), Large surface radiative forcing from topographic blowing snow residuals measured in the High Arctic at Eureka, *Atmospheric Chemistry and Physics*, *9*(6), 1847–1862, doi:10.5194/acp-9-1847-2009. 47

Lesins, G., T. J. Duck, and J. R. Drummond (2010), Climate trends at Eureka in the Canadian high arctic, *Atmosphere-Ocean*, *48*(2), 59–80, doi:10.3137/AO1103.2010. 52, 53

Liu, Z., M. Vaughan, D. Winker, C. Kittaka, B. Getzewich, R. Kuehn, A. Omar, K. Powell, C. Trepte, and C. Hostetler (2009), The CALIPSO Lidar Cloud and Aerosol Discrimination: Version 2 Algorithm and Initial Assessment of Performance, *Journal of Atmospheric and Oceanic Technology*, *26*(7), 1198–1213, doi:10.1175/2009JTECHA1229.1. 18, 73

Manney, G. L., M. L. Santee, M. Rex, N. J. Livesey, M. C. Pitts, P. Veefkind, E. R. Nash, I. Wohltmann, R. Lehmann, L. Froidevaux, L. R. Poole, M. R. Schoeberl, D. P. Haffner, J. Davies, V. Dorokhov, H. Gernandt, B. Johnson, R. Kivi, E. Kyrö, N. Larsen, P. F. Levelt, A. Makshtas, C. T. McElroy, H. Nakajima, M. C. Parrondo, D. W. Tarasick, P. von der Gathen, K. A. Walker, and N. S. Zinoviev (2011), Unprecedented Arctic ozone loss in 2011, *Nature*, *478*(7370), 469–475, doi:10.1038/nature10556. 15, 46

Maturilli, M., R. Neuber, P. Massoli, F. Cairo, A. Adriani, M. L. Moriconi, and G. Di Donfrancesco (2005), Differences in Arctic and Antarctic PSC occurrence as observed by lidar in Ny-Ålesund (79N, 12E) and McMurdo (78S, 167E), *Atmospheric Chemistry and Physics*, *5*(8), 2081–2090, doi:10.5194/acp-5-2081-2005. 55

Measures, R. M. (1984), *Laser remote sensing: fundamentals and applications*, 510 pp., Wiley, New York. 41

Melo, S. M., E. Farahani, K. Strong, M. Bassford, K. Preston, and C. McLinden (2004), NO2 vertical profiles retrieved from ground-based measurements during spring 1999 in the Canadian Arctic, *Advances in Space Research*, *34*(4), 786–792, doi:10.1016/j.asr.2003.08.065. 31

Menut, L., C. Flamant, J. Pelon, and P. H. Flamant (1999), Urban Boundary-Layer Height Determination from Lidar Measurements Over the Paris Area, *Applied Optics*, *38*(6), 945, doi:10.1364/AO.38.000945. 19

Mishchenko, M. I., and K. Sassen (1998), Depolarization of lidar returns by small ice crystals: An application to contrails, *Geophysical Research Letters*, *25*(3), 309–312, doi:10.1029/97GL03764. 22

Mohanakumar, K. (2008), *Stratosphere Troposphere Interactions: An Introduction*, 416 pp., Springer Science + Business Media B. V. 46

Moritz, R. E., C. M. Bitz, and E. J. Steig (2002), Dynamics of Recent Climate Change in the Arctic, *Science*, *297*(5586), 1497–1502, doi:10.1126/science.1076522. 15

Müller, D. (2003), Saharan dust over a central European EARLINET-AERONET site: Combined observations with Raman lidar and Sun photometer, *Journal of Geophysical Research*, *108*(D12), 4345, doi:10.1029/2002JD002918. 50

Müller, D., I. Mattis, A. Ansmann, B. Wehner, D. Althausen, U. Wandinger, and O. Dubovik (2004), Closure study on optical and microphysical properties of a mixed urban and Arctic haze air mass observed with Raman lidar and Sun photometer, *Journal of Geophysical Research: Atmospheres*, *109*(D13), doi:10.1029/2003JD004200. 51, 55

Musat, I. C. (2004), Short-term variability of atmospheric extinction during the night, under clear-sky conditions, investigated by broadband stellar photometry., Ph.D. thesis, University of Maryland, College Park. 18

Nott, G. J., T. J. Duck, J. G. Doyle, M. E. W. Coffin, C. Perro, C. P. Thackray, J. R. Drummond, P. F. Fogal, E. McCullough, and R. J. Sica (2012), A Remotely Operated Lidar for Aerosol, Temperature, and Water Vapor Profiling in the High Arctic, *Journal of Atmospheric and Oceanic Technology*, *29*(2), 221–234, doi:10.1175/JTECH-D-11-00046.1. 70, 105

O'Neill, N. T. (1999), On NO_2 optical depths in the visible, *Internal AERONET memo*, GSFC/NASA. 31, 65

O'Neill, N. T. (2013), Personal communication. 66, 72

O'Neill, N. T., O. Dubovik, and T. F. Eck (2001a), Modified Ångström Exponent for the Characterization of Submicrometer Aerosols, *Appl. Opt.*, *40*(15), 2368–2375. 33, 34

O'Neill, N. T., T. F. Eck, B. N. Holben, A. Smirnov, O. Dubovik, and A. Royer (2001b), Bimodal size distribution influences on the variation of Angstrom derivatives in spectral and optical depth space, *J. Geophys. Res.*, *106*. 34, 37

O'Neill, N. T., T. F. Eck, A. Smirnov, B. N. Holben, and S. Thulasiraman (2003), Spectral discrimination of coarse and fine mode optical depth, *J. Geophys. Res.*, *108*. 21, 34, 63, 94

O'Neill, N. T., K. B. Strawbridge, S. Thulasiraman, J. Zhang, A. Royer, and J. Freemantle (2004), Optical coherency of sunphotometry, sky radiometry and lidar measurements during the early phase of Pacific 2001, *Atmospheric Environment*, *38*(34), 5887–5894, doi:DOI:10.1016/j.atmosenv.2003.12.049. 50

O'Neill, N. T., O. Pancrati, K. Baibakov, E. Eloranta, R. L. Batchelor, J. Freemantle, L. J. B. McArthur, K. Strong, and R. Lindenmaier (2008), Occurrence of weak, sub-micron, tropospheric aerosol events at high Arctic latitudes, *Geophysical Research Letters*, *35*(14), L14,814, doi:10.1029/2008GL033733. 20, 21, 22, 50, 54, 73, 83

O'Neill, N. T., C. Perro, A. Saha, G. Lesins, T. J. Duck, E. W. Eloranta, G. J. Nott, A. Hoffman, M. L. Karumudi, C. Ritter, A. Bourassa, I. Abboud, S. a. Carn, and V. Savastiouk (2012), Properties of Sarychev sulphate aerosols over the Arctic, *Journal of Geophysical Research*, *117*(D4), D04,203, doi:10.1029/2011JD016838. 21, 51, 55, 80

Pahlow, M., D. Müller, M. Tesche, H. Eichler, G. Feingold, W. L. Eberhard, and Y.-F. Cheng (2006), Retrieval of aerosol properties from combined multiwavelength lidar and sunphotometer measurements, *Applied Optics*, *45*(28), 7429–7442, doi:10.1364/AO.45.007429. 51

Papayannis, A., H. Q. Zhang, V. Amiridis, H. B. Ju, G. Chourdakis, G. Georgoussis, C. Pérez, H. B. Chen, P. Goloub, R. E. Mamouri, S. Kazadzis, D. Paronis, G. Tsaknakis, and J. M. Baldasano (2007), Extraordinary dust event over Beijing, China, during April 2006: Lidar, Sun photometric, satellite observations and model validation, *Geophysical Research Letters*, *34*(7), L07,806, doi:10.1029/2006GL029125. 50

Pérez-Ramírez, D. (2012), Personal communication. 62

Pérez-Ramírez, D., J. Aceituno, B. Ruiz, F. J. Olmo, and L. Alados-Arboledas (2008a), Development and calibration of a star photometer to measure the aerosol optical depth:

Smoke observations at a high mountain site, *Atmospheric Environment*, *42*(11), 2733–2738, doi:DOI:10.1016/j.atmosenv.2007.06.009. 18, 65

Pérez-Ramírez, D., B. Ruiz, J. Aceituno, F. J. Olmo, and L. Alados-Arboledas (2008b), Application of Sun/star photometry to derive the aerosol optical depth, *International Journal of Remote Sensing*, *29*(17), 5113. 58, 60, 65

Pérez-Ramírez, D., H. Lyamani, F. Olmo, and L. Alados-Arboledas (2011), Improvements in star photometry for aerosol characterizations, *Journal of Aerosol Science*, *42*(10), 737–745, doi:10.1016/j.jaerosci.2011.06.010. 58

Pérez-Ramírez, D., F. Navas-Guzmán, H. Lyamani, J. Fernández-Gálvez, F. J. Olmo, and L. Alados-Arboledas (2012a), Retrievals of precipitable water vapor using star photometry: Assessment with Raman lidar and link to sun photometry, *Journal of Geophysical Research*, *117*(D5), D05,202, doi:10.1029/2011JD016450. 31

Pérez-Ramírez, D., H. Lyamani, F. J. Olmo, D. N. Whiteman, F. Navas-Guzmán, and L. Alados-Arboledas (2012b), Cloud screening and quality control algorithm for star photometer data: assessment with lidar measurements and with all-sky images, *Atmospheric Measurement Techniques*, *5*(7), 1585–1599, doi:10.5194/amt-5-1585-2012. 62, 63

Perro, C. (2010), Cloud and aerosol properties measured with a lidar in the high Arctic at Eureka, M.Sc. thesis, Dalhousie University. 45

Perro, C. (2013), Personal communication. 72, 87

Pitts, M. C., L. R. Poole, A. Dörnbrack, and L. W. Thomason (2011), The 2009–2010 Arctic polar stratospheric cloud season: a CALIPSO perspective, *Atmospheric Chemistry and Physics*, *11*(5), 2161–2177, doi:10.5194/acp-11-2161-2011. 89

Pueschel, R., and S. Kinne (1995), Physical and radiative properties of Arctic atmospheric aerosols, *Science of The Total Environment*, *160-161*(null), 811–824, doi:10.1016/0048-9697(95)04414-V. 17

Pueschel, R. F., G. V. Ferry, K. G. Snetsinger, J. Goodman, J. E. Dye, D. Baumgardner, and B. W. Gandrud (1992), A case of Type I polar stratospheric cloud formation by heterogeneous nucleation, *Journal of Geophysical Research*, *97*(D8), 8105, doi:10.1029/91JD02352. 89

Quinn, P., B. Andrews, E. Dutton, G. Shaw, and T. Ruoho-Airola (2006), 4. Arctic Haze, in *AMAP Assessment 2006: Acidifying Pollutants, Arctic Haze, and Acidification in the Arctic*, Arctic Monitoring and Assessment Programme (AMAP), Oslo, Norway. 46

Quinn, P. K., G. Shaw, E. Andrews, E. G. Dutton, T. Ruoho-Airola, and S. L. Gong (2007), Arctic haze: current trends and knowledge gaps, *Tellus B*, *59*(1), doi:10.3402/tellusb.v59i1.16972. 20, 25, 48, 49

Rees, W. G. (2001), *Physical Principles of Remote Sensing*, 343 pp., Cambridge University Press, New York, NY. 26

Saha, a., N. T. O'Neill, E. Eloranta, R. S. Stone, T. F. Eck, S. Zidane, D. Daou, a. Lupu, G. Lesins, M. Shiobara, and L. J. B. McArthur (2010), Pan-Arctic sunphotometry during the ARCTAS-A campaign of April 2008, *Geophysical Research Letters*, *37*(5), n/a–n/a, doi:10.1029/2009GL041375. 20, 50, 54

Sassen, K. (2005), 2. Polarization in Lidar, in *Lidar - Range-Resolved Optical Remote Sensing of the Atmosphere*, edited by C. Weitkamp, Springer Science + Business Media Inc., New York. 44

Sato, M., J. E. Hansen, M. P. McCormick, and J. B. Pollack (1993), Stratospheric aerosol optical depths, 1850–1990, *Journal of Geophysical Research*, *98*(D12), 22,987, doi:10.1029/93JD02553. 88

Schulz, K. (2008), Personal communication, Personal Communication. 30

Schulz, K.-H. (2007), Measuring System Starphotometer, Instruction manual. 29, 38, 57

Schuster, G. L., O. Dubovik, and B. N. Holben (2006), Angstrom exponent and bimodal aerosol size distributions, *J. Geophys. Res.*, *111*. 33

Seinfeld, J. H., and S. N. Pandis (2006), *Atmospheric Chemistry and Physics. From Air Pollution to Climate Change*, 2 ed., 1232 pp., John Wiley & Sons, Hoboken, NJ. 28, 36, 37

Shaw, G. E. (1983), Sun Photometry, *Bulletin of the American Meteorological Society*, *64*(1), 4–10. 18

Shaw, G. E. (1995), The Arctic Haze Phenomenon, *Bulletin of the American Meteorological Society*, *76*(12), 2403–2413, doi:10.1175/1520-0477(1995)076<2403:TAHP>2.0.CO;2. 48

Shaw, G. E., J. A. Reagan, and B. M. Herman (1973), Investigations of Atmospheric Extinction Using Direct Solar Radiation Measurements Made with a Multiple Wavelength Radiometer, *Journal of Applied Meteorology*, *12*(2), 374–380. 28, 58

Shindell, D., and G. Faluvegi (2009), Climate response to regional radiative forcing during the twentieth century, *Nature Geoscience*, *2*(4), 294–300, doi:10.1038/ngeo473. 16, 17

Shiobara, M., and S. Asano (1994), Estimation of Cirrus Optical Thickness from Sun Photometer Measurements, *Journal of Applied Meteorology*, *33*(6), 672–681, doi:10.1175/1520-0450(1994)033<0672:EOCOTF>2.0.CO;2. 66

Smirnov, A., B.N.Holben, T.F.Eck, O.Dubovik, and I.Slutsker (2000), Cloud screening and quality control algorithms for the AERONET database, *Rem.Sens.Env.*, *73*, 337–349. 62, 63

Steinbring, E., W. Ward, and J. R. Drummond (2012), Astronomical Sky Quality Near Eureka, in the Canadian High Arctic, *Publications of the Astronomical Society of the Pacific 124*, (no. 912 (February 2012)), 185–194. 52, 53

Stock, M., C. Ritter, A. Herber, W. von Hoyningen-Huene, K. Baibakov, J. Gräser, T. Orgis, R. Treffeisen, N. Zinoviev, A. Makshtas, and K. Dethloff (2012), Springtime Arctic aerosol: Smoke versus haze, a case study for March 2008, *Atmospheric Environment*, *52*(0), 48–55, doi:10.1016/j.atmosenv.2011.06.051. 20, 48, 51, 55

Stohl, A. (2006), Characteristics of atmospheric transport into the Arctic troposphere, *Journal of Geophysical Research*, *111*(D11), D11,306, doi:10.1029/2005JD006888. 48, 55

Stohl, A., T. Berg, J. F. Burkhart, A. M. Fjaeraa, C. Forster, A. Herber, O. Hov, C. Lunder, W. W. McMillan, S. Oltmans, M. Shiobara, D. Simpson, S. Solberg, K. Stebel, J. Ström, K. Tø rseth, R. Treffeisen, K. Virkkunen, and K. E. Yttri (2007), Arctic smoke - record high air pollution levels in the European Arctic due to agricultural fires in Eastern Europe in spring 2006, *Atmospheric Chemistry and Physics*, *7*(2), 511–534, doi:10.5194/acp-7-511-2007. 49, 55

Stone, R. S., G. P. Anderson, E. P. Shettle, E. Andrews, K. Loukachine, E. G. Dutton, C. Schaaf, and M. O. Roman (2008), Radiative impact of boreal smoke in the Arctic: Observed and modeled, *Journal of Geophysical Research*, *113*(D14), D14S16, doi:10.1029/2007JD009657. 20

Strawa, A. W. (2002), Discriminating Types Ia and Ib polar stratospheric clouds in POAM satellite data, *Journal of Geophysical Research*, *107*(D20), 8291, doi:10.1029/2001JD000458. 89

Stroeve, J. C., M. C. Serreze, M. M. Holland, J. E. Kay, J. Malanik, and A. P. Barrett (2011), The Arctic's rapidly shrinking sea ice cover: a research synthesis, *Climatic Change*, *110*(3-4), 1005–1027, doi:10.1007/s10584-011-0101-1. 15

Thomason, L. W., B. M. Herman, and J. A. Reagan (1983), The Effect of Atmospheric Attenuators with Structured Vertical Distributions on Air Mass Determinations and Langley Plot Analyses, *Journal of the Atmospheric Sciences*, *40*(7), 1851–1854. 28

Tomasi, C., V. Vitale, A. Lupi, C. Di Carmine, M. Campanelli, A. Herber, R. Treffeisen, R. S. Stone, E. Andrews, S. Sharma, V. Radionov, W. von Hoyningen-Huene, K. Stebel, G. H. Hansen, C. L. Myhre, C. Wehrli, V. Aaltonen, H. Lihavainen, A. Virkkula, R. Hillamo, J. Ström, C. Toledano, V. E. Cachorro, P. Ortiz, A. M. de Frutos, S. Blindheim, M. Frioud, M. Gausa, T. Zielinski, T. Petelski, and T. Yamanouchi (2007), Aerosols in polar regions: A historical overview based on optical depth and in situ observations, *Journal of Geophysical Research*, *112*(D16), D16,205, doi:10.1029/2007JD008432. 49, 63

Toon, O. B., and R. P. Turco (1991), Polar stratospheric clouds and ozone depletion, *Scientific American*, *264*, 68–74. 89

Wallace, J., and P. Hobbs (2006), *Atmospheric science: an introductory survey*, 483 pp., Academic Press. 27, 35, 45

Wandinger, U. (2005), 9. Raman Lidar, in *Lidar - Range-Resolved Optical Remote Sensing of the Atmosphere*, edited by C. Weitkamp, p. 456, Springer Science + Business Media Inc., New York. 19, 71

Wang, X., and J. R. Key (2003), Recent trends in Arctic surface, cloud, and radiation

properties from space., *Science (New York, N.Y.)*, *299*(5613), 1725–8, doi:10.1126/science.1078065. 15

Weitkamp, C. (Ed.) (2005), *LIDAR: range-resolved optical remote sensing of the atmosphere.*, 455 pp., Springer Science+Business Media Inc, New York. 18, 41, 42, 71

Winker, D. M., J. R. Pelon, and M. P. McCormick (2003), gg, in *Third International Asia-Pacific Environmental Remote Sensing Remote Sensing of the Atmosphere, Ocean, Environment, and Space*, edited by U. N. Singh, T. Itabe, and Z. Liu, pp. 1–11, International Society for Optics and Photonics, doi:10.1117/12.466539. 19

You, Y., G. W. Kattawar, P. Yang, Y. X. Hu, and B. A. Baum (2006), Sensitivity of depolarized lidar signals to cloud and aerosol particle properties, *Journal of Quantitative Spectroscopy and Radiative Transfer*, *100*(1-3), 470–482, doi:10.1016/j.jqsrt.2005.11.058. 22

Young, C. L., I. N. Sokolik, and J. Dufek (2012), Regional radiative impact of volcanic aerosol from the 2009 eruption of Mt. Redoubt, *Atmospheric Chemistry and Physics*, *12*(8), 3699–3715, doi:10.5194/acp-12-3699-2012. 20

Universität Bremen

Die zur Veröffentlichung erstellte Version meiner Dissertation enthält die folgenden Überarbeitungen bzw. Kürzungen, deren Umfang auf den angegebenen Seiten eindeutig gekennzeichnet sind. Die folgenden Überarbeitungen/Kürzungen sind erfolgt:

Seite	erfolgte Überarbeitung/Kürzung
1)	frontpage - change in title
2)	pp.72,82,84-86,88,91,92 - figures improved
3)	p.105 - some text added
4)	p.110 - some references have been added

Kandidatin/Kandidat: Konstantin Baibakov

Sherbrooke, March 31, 2014

Ort/Datum **Unterschrift**

Vorsitzende/Vorsitzender der Prüfungskommission: Prof. O. Schrems

Ich bin mit den gemachten Überarbeitungen/Kürzungen in der für die Veröffentlichung erstellten Version dieser Dissertation einverstanden.

Bremen, March 31, 2014

Ort/Datum **Unterschrift**